THE ROLE OF QUANTUM DOTS IN THE FUNCTIONAL LAYERS OF THIN FILM POLYMER SOLAR CELLS

Author: Abiodun Kazeem Ogundele

Supervisor: Professor Genene Tessema Mola

A thesis submitted for the award of
Doctor of Philosophy in Physics (Material Sciences)

School of Chemistry and Physics
University of KwaZulu-Natal, Pietermaritzburg Campus
South Africa

November 2024

DECLARATION 1: PLAGIARISM

I, **Abiodun Kazeem Ogundele**, declare that;

1. The reported investigations in this thesis, except where otherwise indicated, are the outcomes of my original research.

2. This project has not been presented for any degree or examination at any other institution.

3. This project does not contain other persons' data, pictures, graphs or other information unless specifically acknowledged as being sourced from other persons.

4. This project does not contain other persons' writing unless specifically acknowledged as being sourced from other researchers. Where other written sources have been quoted, then:

   (a) Their words have been re-written, but the general information attributed to them has been referenced.

   (b) Where their exact words have been used, then their writing has been placed in italics and inside quotation marks and referenced.

5. This project does not contain text, graphics or tables copied and pasted from the Internet, unless specifically acknowledged, and the source is detailed in the thesis and the references sections.

Signature:..... Date: 12 March 2025

DECLARATION 2: PUBLICATIONS

I, Abiodun Kazeem Ogundele declare that the following research papers as indicated below formed the integral parts of my thesis.

1. **Ogundele, A. K.**, & Mola, G. T. (2022). Ternary atoms alloy quantum dot assisted hole transport in thin film polymer solar cells. Journal of Physics and Chemistry of Solids, 171, 110999. My role includes the conceptualisation and design of experiments, fabrication of solar cell devices, data collection and analysis, and drafting of manuscripts. The drafted manuscript was then sent to my supervisor for editing before submitting to the journal for consideration. The reviewers' comments were later addressed with the guidance of my supervisor.

2. **Ogundele, A. K.**, & Mola, G. T. (2023). Semiconductor quantum dots as a mechanism to enhance charge transfer processes in polymer solar cells. Chemosphere, 345, 140453. My role in this manuscript included the conception of the experimental design, fabrication of devices, data curation and analysis, and drafting the manuscript. My supervisor was consulted intermittently during these processes and edited the manuscript before it was submitted to the journal for consideration. The reviewers' comments were later addressed, leading to the final acceptance and subsequent publication by the journal.

3. **Ogundele, A. K.**, & Mola, G. T. (2024). Enhanced Collection of Photocurrents Using Core-Shell Quantum Dots Decorated Polymer Composite Films. Energy & Fuels. My contributions to the published manuscript include the conceptualisation, design, and fabrication of devices, as well as the collection and analysis of data, and drafting the manuscript. The draft was subsequently forwarded to my supervisor **for editing** before its eventual submission to the journal for publication. The reviewers' comments were addressed prior to final acceptance and publication.

Signature:.... [redacted] ..... Date: 12 March 2025 .....

The following publications and article are not listed in my thesis.

1. Ashagre, S., **Ogundele, A. K**., Ike, J. N., Gebremichael, B., Bekele, M., Sharma, G. D., & Mola, G. T. (2023). Synergistic contribution of potassium sulfide doped with silver nanoparticles on the performance of thin film organic solar cells. Journal of Physics and Chemistry of Solids, 177, 111290. My role in this manuscript included experimental preparations, device fabrication, and drafting the manuscript. The other authors contributed their sections before the supervisor made final edits and submitted the manuscript to the journal for consideration. The reviewers' comments were addressed collaboratively by all the authors.

2. Ahmed, A. Y., **Ogundele A.K**.,Mohammed S.G. Hamed, M.S., Newayemedhin Tegegne, Amit Kumar, Gaurav Sharma & Mola, G. T. (2025). Application of cobalt-sulphide to suppress charge recombination in polymer solar cell. Materials Science in Semiconductor Processing. My role in this manuscript includes experimental preparations, collaborating on device fabrication, drafting part of the manuscript, and responding to reviewers' comments for specific sections.

3. **Ogundele, A. K.**, & Mola, G. T. Semiconductor quantum dots as a mechanism to harvest solar energy in thin film solar cell technologies. A Review. I wrote the manuscript and sent it to my supervisor for editing in preparation for submission to a journal for consideration.

DEDICATION

To the loving memory of my father, Mr. Ganiyu Akinloye Akanbi Ogundele, whose quiet moral guidance, hard work, and compassion inspire me daily. Though he is not here to share this moment, I feel his presence in everything I do. Dad, this achievement is for you. Thank you for instilling in us essential core moral values.

To my mother, Mrs. Taibat Kosemani Ogundele, and my loving siblings, Folashade, Atinuke, and Temitope Ogundele, for their unwavering love and support.

To my own "World", led by my ever-supportive, pious, dependable, and loving wife, Omokehinde Halimah Abake, and my children, Fadilah Olatide Atoke, Suad Foyinsola Abeke and Abdullah Akinwumi Akinloye Akanbi Ogundele, for maintaining high moral standards and their incredible attitudes even in my absence.

ACKNOWLEDGEMENTS

In the name of Allah, the Most Gracious, the Most Merciful. My heart overflows with gratitude to Allah, the eternal guide who illuminates the path of truth and bestows upon us boundless blessings. With every fibre of my being, I say "Alhamdulillah" for His grace that has carried me through this journey.

I am profoundly thankful to my supervisor, **Professor Genene Tessema Mola**, whose belief in me set the course for this incredible sojourn to South Africa. His unmatched professionalism, moral integrity, and generous support both financial and personal fueled the momentum of this work. The wisdom and mentorship he imparted will remain etched in my mind as a source of strength and inspiration. Words alone cannot express my deep appreciation for your role in shaping the success of this thesis.

To the University of KwaZulu-Natal, I express my sincere gratitude for granting me three years of fee remission. Your support, along with that of the National Research Foundation (NRF), and my supervisor's backing, has been instrumental in making this endeavour possible. The Southwestern University, Nigeria is also acknowledged.

With the deepest reverence, I honour the memory of my late father. His sacrifices, immeasurable and enduring, paved the way for my siblings and me to thrive in this world. No words can fully capture the magnitude of what you gave; there will never be another like you. May your soul continue to rest in eternal peace, amin. My mother, a wellspring of love and strength, your unwavering faith and priceless contributions continue to guide me. To my beloved sisters, Folashade and Atinuke, and steadfast brother Temitope, thank you for standing by me with your unshakeable support. I am grateful to all my family members, especially the descendants of G.A. Ogundele, whose collective moral and spiritual support sustained me through every challenge. My boundless gratitude extends to Alhaji N.A. Lasisi, whose presence has been a pillar in my life. Your unflinching support has illuminated challenging moments and propelled me forward. I pray Allah's unlimited Albarka continues to bless all that springs from you. The moral support of my in-laws, Alhaji Wahab and Alhaja Faosat Lawal is respectively acknowledged.

To Dr. S.O. Oseni, whose guidance was a beacon of light in my early days in the program and well beyond, I remain forever thankful. My special thanks to Dr. N. B. Dlamini for

his ever selfless nature and willingness to help whenever called upon. The camaraderie and collaboration I experienced with the Material Science Lab group past and present members, Dr. M. A. Adedeji, Abdallah AYA Ahmed, and many others, will forever hold a special place in my heart. Our shared efforts, discussions, and mutual support have forged bonds that transcend the walls of academia. Special thanks also go to the academic, technical, and support staff of the School of Physics. My thanks go to the procurement officer at PMB campus, Mr. Shawn Ball and those of University MMU unit for their invaluable assistance behind the scenes.

To my treasured friends spread across the world, you are few but deeply cherished. Your contributions whether big or small have not gone unnoticed, and I hold each of you in the highest regard. And to my friends in South Africa, thank you for embracing me with warmth and friendship; you made a foreign land feel like home.

Above all, my heart swells with love and gratitude for my life partner, my steadfast wife, **Mrs. Kehinde Halimah Ogundele**. Your sacrifices have been the backbone of this journey. Your unwavering prayers, emotional strength, and steadfast support have carried me through these crucial periods. To my children (Alemilojus), Olatide, Foyinsola, and Akinwumi, your patience and strength during my absence have been profound. My love for you is boundless, and I entrust your future to the hands of Almighty Allah, praying for His infinite blessings upon your lives.

ABSTRACT

Polymer solar cells (PSCs) have emerged as a promising class of photovoltaic technology, valued for their lightweight, flexibility, and potential for cost-effective, large-scale production. The ability to fully harness their potential is dependent on resolving the challenges mitigating their efficient power conversion efficiency (PCE) and environmental stability. As such, various advancements in material engineering have been embarked upon for device optimisation. This study explored the use of compound semiconductor quantum dots (SQDs), as guests in the functional layers of polymer solar cells using both conventional and inverted device architectures. Semiconductor quantum dots represent a class of inorganic materials that have been utilised for matured but expensive organic solar cells not viable for large-scale production. The fascinating inherent features of SQDs are leveraged in their careful introduction into the hole transport, photoactive, and electron transport layers of organic solar cells. The fullerene-based solar cells were fabricated upon the introduction of alloyed, core, and core-shell SQDs in their functional layers in ambient conditions. The II-VI compound SQDs are employed, such as CdTeSe, core ZnS, and core-shell $Cd_xS/Zn_{1-x}S$. The photoactive layer blends are composed of poly(3-hexylthiophene) (P3HT): [6,6]-phenyl-C_{61}-butyric acid methyl ester (P3HT:PCBM) and poly[[4,8-bis[(2-ethylhexyl)oxy]benzo[1,2-b]dithiophene-2,6-diyl][3-fluoro-2-[(2-ethylhexyl)-carbo-nyl]-thieno[3,4-b] thiophenediyl]]:[6,6]-phenyl C_{71} butyric acid methyl ester (PTB7:PC_{71}BM). The as-synthesised SQDs and fabricated devices were subjected to various characterisations. The analysed data collected from various characterisation techniques showed that the incorporation of SQDs in the functional layers broadened the absorption range, improved light harvesting, and enhanced charge transport. These effects translated into better device parameters, as evident in the improved power conversion efficiencies of the modified devices. Ultimately, it can be inferred from this study that the use of semiconductor quantum dots in the various functional layers of PSCs at certain thresholds assisted in the optimisation of the devices, improving their PCE and shelf lives. This study explores the synergy between organic and inorganic materials (hybrid materials) that have positively impacted the performance of various PV technologies.

CONTENTS

LIST OF FIGURES

LIST OF TABLES

LIST OF ABBREVIATIONS AND SYMBOLS

A	Acceptor
a_b	Bohr radius
Ag	Silver
Al	Aluminum
BHJ	Bulk heterojunction
CdS	Cadmium sulphide
CdSe	Cadmium Selenide
$Cd_xS/Zn_{1-x}S$	Core-shell alloy cadmium sulphide/Zinc sulphide
CdTe	Cadmium telluride
CdTeSe	Cadmium telluride selenide
CNT	Carbon Nanotubes
CB	Chlorobenzene
CF	Chlorofoam
CP	Conjugated Pollymers
CIGS	Copper Indium Gallium Diselenide
D	Donor
DIO	1,8, diiodo octane
DSSCs	The dye-sensitised solar cells
EDX	Energy-dispersive (analysis) X-ray
E_g	Energy bandgap

ε_r	dielectric constant
EQE	External quantum efficiency
E_{opt}	Optical band gap energy
ETL	Electron transport layer
ESTL	Electron selective transport layer
FTIR	Fourier transform infrared spectroscopy
FF	Fill factor
FTO	Fluorine doped tin oxide
G_{max}	Maximum exciton generation rate
h	Plank's constant
$\hbar$	Reduced Plank's constant
h^+	Hole charge
HCL	Hydrochloric acid
HNO_3	Nitric acid
HRSEM	High resolution scanning electron microscopy
HRTEM	High resolution transmission electron microscopy
HTL	Hole transport layer
HOMO	Higher occupied molecular orbital
ICP	Intrinsic conducting polymer
ITO	Indium tin oxide
J_{SC}	Short-circuit current density
J-V	Current density-voltage Curve
J_{MAX}	Maximum current density
LEDs	Light emitting diode
LUMO	Lower unoccupied molecular orbital
LiF	Lithium fluoride
m_e	mass of electron
m_e*	Effective mass of electron
m_h	Mass of hole
m_h*	Effective mass of hole
MoO_3	Molybdenum oxide
μ_e	Electron mobility
μ_l	Low field mobility
μ_p	Hole mobility

η_{coll}	charge collection efficiency
η_{diss}	charge dissociation efficiency
η_{IQE}	Internal quantum efficiency
NC	Nanocomposite
NFA	Non-fullerene acceptors
NP	Nanoparticles
V_{OC}	Open-circuit voltage
QD	Quantum dots
ODT	Octanedithiol
OPV	Organic photovoltaic
OSCs	Organic solar cells
P3HT	Poly(3-hexylthiophene)
PCE	Power conversion efficiency
PCBM	[6,6]-phenyl-C61-butyric acid methyl ester
PCPDTBT	Poly[2,6-(4,4-bis-(2-ethylhexyl)-4H-cyclopenta [2,1-b;3,4-b'] dithiophene)-alt-4,7(2,1,3-benzothiadiazole])
PBDTTBT	poly(4,8-bis(2,5-dioctyl-2-thienyl)-benzo[1,2-b:4,5-b']dithiophene -alt-[4,7-bis(2-thienyl)-2,1,3-benzothiadiazole)-5,5'-diyl])
PEDOT:PSS	Poly(ethylene-3-4-dioxy thiophene):poly styrene sulphonate
PL	Photoluminicense
P_{max}	Maximum power
PSCs	Polymer solar cells
PPV	Poly(p-phenylene vinylene)

PTB7	Poly[[4,8-bis[(2-ethyhexyl)oxy]benzo(1,2-b:4,5b)dithiophene2,6diyl] [3fluoro2[(2ethylhexyl)carbonyl]thieno[3,4-b]thiophenediyl]]
PV	Photovoltaic
QDSC	Quantum dot solar cell
R2R	Roll-to-roll
SCLC	Space Charge Limited current
SEM	Scanning electron microscopy
SQD	Semiconductor quantum dots
SRH	Shockley-Read-Hall
R_S	Series resistance
R_SH	Shunt (parallel) resistance
TCOs	Transparent conducting oxides
TFOSCs	Thin film organic solar cells
TFPSCs	Thin film polymer solar cells
TEM	Transmission electron microscopy
TiO_2	Titanium dioxide
TMC	Transition metal Chalcogenides
UV-Vis	Ultra violet-visible
V_{max}	Maximum voltage
V_{oc}	Open-circuit voltage
WF	Work function
WO_3	Tungsten oxide
XRD	X-ray diffractometer
ZnO	Zinc oxide
ZnS	Zinc Sulphide or Zinc sulfide

PREFACE

The research discussed in this thesis was carried out in the School of Chemistry and Physics, College of Agriculture, Engineering and Science of the University of Kwa-Zulu Natal, Pietermaritzburg, from January 2021 until July 2024 by Abiodun Kazeem Ogundele under the supervision of Professor Genene Tessema Mola.

As the candidate's supervisor, I, Professor Genene Tessema Mola, agree to the submission of this thesis.

Signed:..... ..... Date:12 March 2025.....

I, Abiodun Kazeem Ogundele, hereby declare that all the material incorporated in this dissertation are my own original work, except where acknowledgement is made by name or in the form of a reference. The work contained in herein has not been submitted in any form for any degree or diploma to any other institution.

Signed:..... ..... Date:.....12-03-2025.....

CHAPTER 1

INTRODUCTION

1.1 Background of the study

Energy's profound and multifaceted impact on mankind over the last centuries has been transformational, shaping economies, societies, and the environment in complex ways. The discovery and utilisation of coal and fossil fuels stimulated the industrial revolution that heralded unprecedented economic growth, urbanisation, and technological advancement. Despite the significant benefits of energy, access to modern energy services remains inadequate globally, leaving millions of people lacking reliable and clean electricity, especially in developing countries [1, 2]. According to "Our World in Data" reports from 2008 to 2022, non-renewable energy sources have played dominant roles in the global energy mix with a contribution of about 83% [1] (see Figure 1.1a). However, they are not only exhaustible but also pose various serious and painful accruing environmental hazards for the present and future of mankind [3, 4]. Hence, the primary challenges involve accelerating the energy transition and ensuring that energy systems are sustainable, fair, resilient, clean, and renewable. This effort is vital to satisfy the needs of both present and future generations while safeguarding natural resources and maintaining a secure environment. The cleanest energy sources can be referred to as those with minimal detrimental environmental impacts regarding greenhouse gas emissions and other hazardous pollution [5]. Nuclear energy, one of the non-renewable energy sources is relatively clean regarding greenhouse gas emissions. However, it poses a serious threat regarding waste management and operation safety. Likewise, it serves as a security soft target and therefore cannot be depended on for a clean energy transition.

Consequently, the most reliable clean energy options are renewable energy sources, including

geothermal power, wind, bioenergy, marine, ocean, hydroelectric, and solar. Solar energy has gained particular attention due to its modularity, scalability, low operation costs, environmental friendliness, versatility, and inexhaustible abundance. According to 2024 reports from the International Energy Agency, the National Renewable Energy Laboratory (NREL), and other scientific and research institutions, the sun produces an immense amount of energy, far surpassing global energy consumption. These research bodies have consistently highlighted significant potential and technological advancements in solar energy, noting a dramatic increase in international solar energy consumption from 0.2% in 2008 to 21.% in 2022, [1] as depicted in Figure 1.1b.

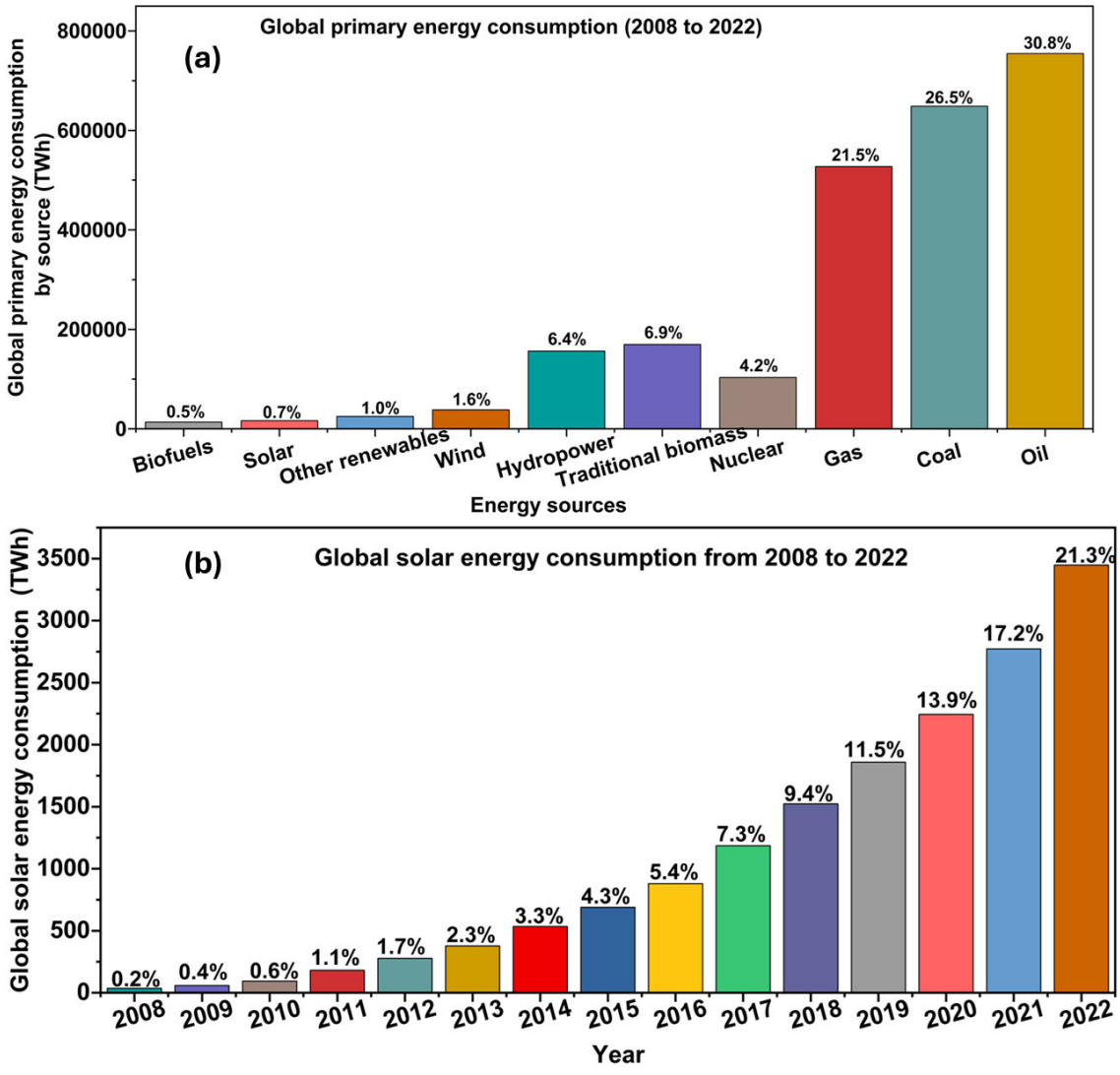

Figure 1.1: (a) Global primary energy consumption by source (b) Global solar energy consumption) [Data source: Energy Institute-Statistical Review of World Energy, 2023].

Solar energy is widely considered one of the best and cleanest forms of renewable energy [6]

due to its numerous benefits. This includes zero greenhouse gas emissions, low environmental impact, renewability, versatility, and potential for job creation [7, 8, 9]. It is transformed into electrical energy through the photovoltaic effect using various routes. Solar photovoltaic systems employ various materials for their operation and can be categorised accordingly. They are inorganic solar cells, polymer solar cells (organic solar cells) and hybrid solar cells as indicated in Figure 1.2. The inorganic solar cells are largely manufactured from inorganic materials via

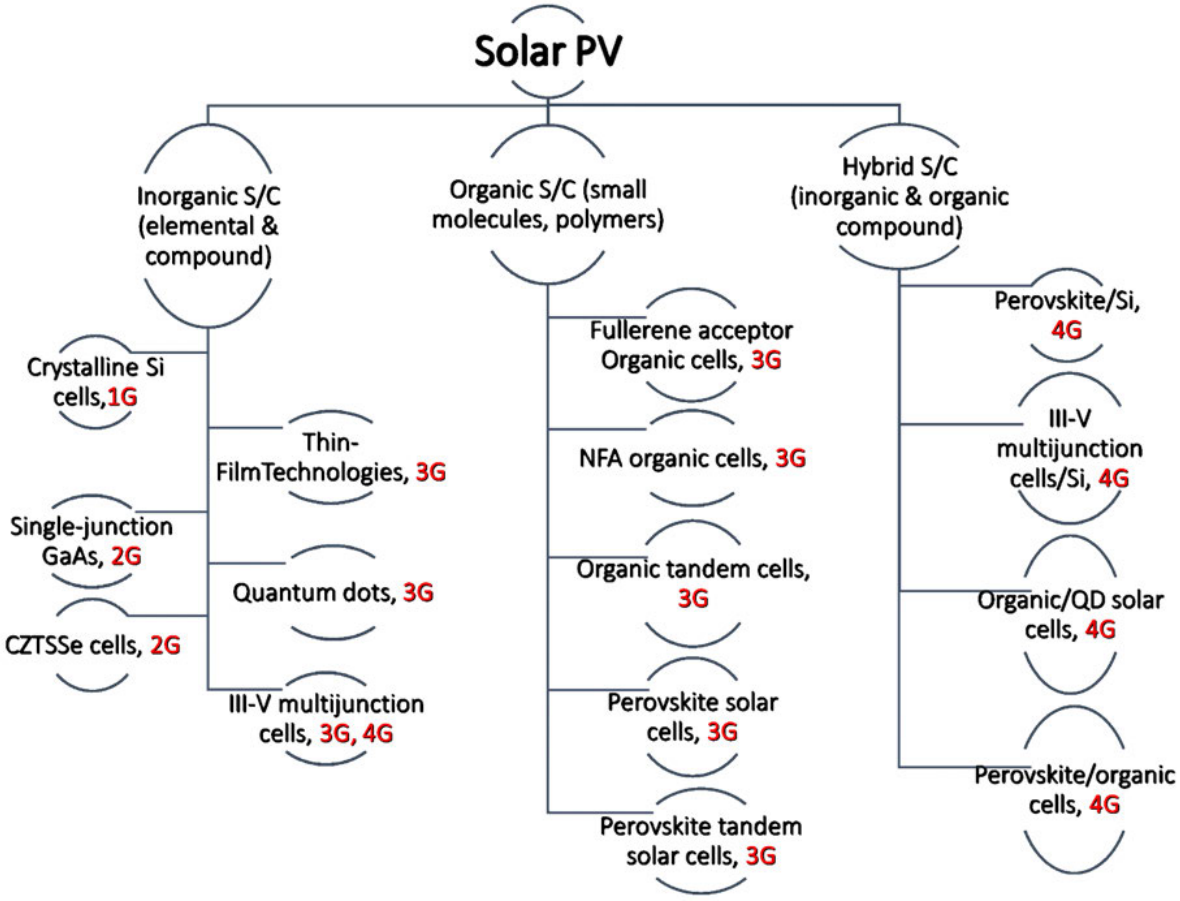

Figure 1.2: Overview of generations of photovoltaic (PV) technology.

complex and cost-intensive processes which cumulated into their high cost of production. The first generation (**1G**) of inorganic solar cells are produced from abundant and efficient elemental crystalline silicon. Similarly, group semiconductor materials like cadmium telluride (CdTe), cadmium selenide (CdSe), and copper indium gallium selenide (CIGS) have been developed to produce second-generation (**2G**) inorganic solar cells. The third generation (**3G**) of inorganic solar cells was achieved via III-V multijunction cells as shown in Figure 1.2. Noticeably, inorganic solar cells are matured technologies due to their relatively superior power conversion efficiencies (PCEs) and environmental stabilities. The intricate manufacturing processes result in high production costs, making it challenging to replace traditional energy sources

with large-scale production of their modules. Conversely, polymer solar cells (PSCs) are made using organic conducting plastics, also known as conducting polymers, through a more economical and simpler process. PSCs are categorised as third-generation PV and have continued to emerge due to their affordability. Additional benefits include their flexibility and lightweight nature [10]. These enable them to be fabricated on flexible substrates like textiles, wearable devices, portable electronics, and plastics, which are not feasible with traditional rigid inorganic solar cells. The versatility of PSC is evident in its adaptation to specific aesthetic usages and integration into architectural elements like windows since it can be manufactured as a transparent or coloured device without compromising the visual appearance. Furthermore, the solution-based manufacturing process employed in the PSCs allows researchers to explore new materials and device architectures. This includes modifying existing ones compared to the more rigid yet cumbersome manufacturing processes involved in the inorganic solar cells [11, 12]. Remarkably, hybrid solar cells leverage the use of inorganic and organic materials for their processes to achieve better PV parameters as well as reduce the cost of production. This latest technology combines the various advantages of previous generations of PV to achieve more desirable benefits which include better cell parameters, flexible structures, and cost-effectiveness. Polymer solar cell breakthrough emanated from the novel bulk heterojunction (BHJ) organic solar cell discovered in the 1990s, while the continual understanding of its working principles has led to various advancements. These include excellent choice of host solvent, the optimal ratio of donor-fullerene-acceptor polymers, stacking of multiple photoactive layers, and optimal tuning of the morphology of functional layers. Other progressions are interfacial layer engineering, use of the solvent additive in the functional layers, solvent annealing of functional layers, development of new acceptor small molecules, and doping of a foreign component material into the functional layers [13, 14, 15, 16, 17, 18, 19, 20, 21, 22]. The applications of these various strategies have led to a PCE of about 19.2% for a single photoactive layer [23]. Nonetheless, some hindrances have continued to mitigate the commercialisation of polymer solar cell modules despite various interesting advantages achieved since its breakthrough.

1.2 Problem statement

The transition from non-renewable to renewable energy sources is slow due to the lack of political will, unavailability of cheap and reliable solar cell technologies as well as efficient renewable energy storage facilities. Also, some of the health challenges facing mankind have been reportedly linked to environmental degradation and climatic changes emanating from the

continuous use of non-renewable energy sources like coal and fossil fuels [24, 25, 26]. On the other hand, ecological security for the present and future of mankind cannot be achieved in isolation without considering the existence of energy poverty even with the present use of fossil fuels. Certainly, there is an apparent need to rapidly provide alternative sources of energy that can compete and gradually replace the present traditional source. This has led to the advancement in PV technology. The mature but expensive inorganic solar energy modules are not capable of replacing these traditional non-renewable sources, leading to a slow energy transitioning process and inefficient energy poverty alleviation. The advent of polymer solar cell technology with its potential to provide cheap energy for mankind has continued to emerge with various technological advancements across various disciplines globally.

1.3 Justifications for the study

Despite the numerous notable and intriguing features of polymer solar cells that highlight their potential to address the energy crisis, some critical obstacles hinder their commercialisation. The power conversion efficiencies of thin-film polymer solar cells (TFPSCs) have yet to reach the levels achieved by mature inorganic solar technologies. For instance, researchers at Helmholtz-Zentrum Berlin recently reported an impressive PCE of 32.5% using silicon tandem solar cells.[27]. Other factors like low mobility of charge carriers, open voltage, photogenerated currents, and external quantum efficiency (EQE) contribute to the limitations of low PCE in TFPSCs.

Furthermore, the degradation of TFPSCs upon exposure to environmental factors like oxygen, moisture, and ultraviolet light is high, and this reduces the stability of the cell parameters thereby reducing their shelf life. Another poser is the material's scalability and purity; for instance, efficient solar cells require high-purity polymers which sometimes are expensive when producing at a scale.

Similarly, energy losses in the interfaces of the functional layers require further interfacial engineering to minimise the losses as imperfections significantly decrease the PCEs. Moreover, the energy level mismatching of various constituents of functional layers between the electrodes inhibits efficient charge extractions thereby depleting the cell parameters.

Additionally, the PSCs are sensitive to fluctuations in temperature which tend to affect the cell parameters of the fabricated devices. Remarkably, the various limiting factors are being

combated in different ways. This includes molecular engineering of the functional layers [28], improved device architecture [29], and interfacial engineering [30, 31, 32]. Importantly, the introduction of inorganic materials as intentionally doped impurity in the functional layers of TFPSCs has led to an increase in photocurrents, better stability, improved work functions of electrodes, optimal energy level alignment and ultimately improved PCEs [33, 34, 35].

Particularly, the emergence of the application of foreign component materials like semiconductor quantum dots (SQD) in appropriate concentrations in the functional layers of PSCs has proven to be a promising route in achieving characteristic efficient and durable solar cells for the present and future generations.

1.4 Aim of the thesis

The primary aim of this research thesis is to experimentally explore potential of semiconductor quantum dots in the functional layers of the devices to enhance the cell parameters of thin-film polymer solar cells. The photoactive blends employed are the fundamental donor-acceptor polymers blends of poly (3-hexylthiophene): (6, 6)-phenyl- C61-butyric acid methyl ester (P3HT:PCBM) and poly[[4,8-bis[(2-ethylhexyl)oxy]benzo[1,2-b]dithiophene-2,6-diyl][3-fluoro-2-[(2-ethylhexyl)cabonyl]thieno [3,4-b]thiophenediyl]]:[6,6]-phenyl C_{71}butyric acid methyl ester (PTB7:PC_{71}BM). These strategies involve the application of as-synthesised semiconductor quantum dots in the functional layers of TFPSCs by way of fabrication using both conventional and inverted architecture in ambient conditions. Convincingly, the successful experimental exploration and optimisation of SQD and polymers under ambient conditions guarantees that better PV metrics would be achieved in a more conducive environment such as a glove box and clean room.

1.5 Specific objectives of the thesis

The research focused on fabricating binary and ternary functional layer module devices. This involves the doping of semiconductor quantum dots in the various functional layers (namely, hole transport layer-HTL, photoactive layer, and electron transport layer-ETL) of TFPSCs comprising fundamental binary (donor-acceptor) polymers (P3HT:PCBM and PTB7:PC_{71}BM). Thus, the doping of SQD into the transport layers (ETL & HTL) and active layer was used to achieve binary and ternary functional layer-modified devices respectively.

(i) Synthesis of core zinc sulphide (ZnS), core-shell (CdS/ZnS), and alloy (CdTeSe) semiconductor quantum dots (SQD) via wet chemistry and microwave-assisted irradiation methods.

(ii) Characterisation of the as-synthesised SQD using high-resolution transmission electron Microscope (HRTEM), high-resolution scanning electron Microscope (HRSEM), Fourier Transform Infrared (FTIR) spectroscopy, photoluminescence spectroscopy and X-ray diffraction (XRD) crystallography Fourier transform.

(iii) Fabrication of thin-film polymer solar cells and their optimisation through the integration of as-synthesised SQD into the functional layers, utilizing both conventional and inverted device architectures.

(iv) Collection and analysis of data derived from the fabrication processes to evaluate the effects of SQD on the performance of thin-film polymer solar cells (TFPSCs).

1.6 Thesis outlines

This thesis summarizes my research findings, implications, and final insights. It is organized into seven chapters. The first three chapters are the Introduction, Literature Review, and Material and Methods while the next three chapters consists of three published papers. The final chapter recaps the findings from different chapters, draws inference from the findings and suggests future research works by offering cohesive statements about the thesis.

Chapter 1 (General Introduction) offers detailed insights into the background of the study, statements of the problem, justification of the study, and general and specific objectives of the research.

Chapter 2 (Literature review) delves into the conceptual, theoretical, and empirical review of thin film polymer solar cells and the impacts of semiconductor quantum dots in thin film solar technologies with a specific focus on thin film polymer solar cells.

Chapter 3 (Materials and methods) discusses various materials resources that were utilised for multiple investigations conducted during the research and the methods employed to accomplish them.

In Chapter 4, we describe the impacts of a ternary (CdTeSe) SQD on the hole transport layer of P3HT:PCBM and it is published as "*Ternary Atoms Alloy Quantum Dot Assisted Hole Transport in Thin Film Polymer Solar Cells*."

Chapter 5 is also a published paper in the Chemosphere journal. It reports the findings of the incorporation of core ZnS SQD, a relatively large band gap SQD in the photoactive layer of TFPSCs. It is titled "*Semiconductor Quantum Dots as a Mechanism to Enhance Charge Transfer Processes in Polymer Solar Cells*."

Chapter 6 is published in the ACS Journal of Energy and Fuels, and it is the result of the investigation of the application of as-synthesised medium band gap core-wide band gap shell ($Cd_xS/Zn_{1-x}S$) SQD in the electron transport layer (ETL) of another polymer blend (PTB7:$PC_{71}BM$). It is titled "*Enhanced Collection of Photo-Current using Core-Shell Quantum Dots Decorated Polymer Composite Films*."

Chapter 7 recapitulates the main findings of the research, draws inference based on the findings from research processes, and suggests future research directions.

References

[1] Ritchie, H., Rosado, P. & Roser, M. Access to energy, Our World in Data. (2024)

[2] Agency, I. World energy outlook, OECD/IEA. (2009)

[3] Perera, F. Pollution from fossil-fuel combustion is the leading environmental threat to global pediatric health and equity: Solutions exist. International Journal of Environmental Research And Public Health. **15**, 16 (2018)

[4] Mishra, M., Sahu, S., Mangaraj, P. & Beig, G. Assessment of hazardous radionuclide emission due to fly ash from fossil fuel combustion in industrial activities in india and its impact on public. Journal of Environmental Management. **328** pp. 116908 (2023)

[5] Ritchie, H. & Roser, M. What are the safest and cleanest sources of energy?, Our World in Data. (2023)

[6] Dixit, S. Solar technologies and their implementations: A review, Materials Today Proceedings. **28** pp. 2137-2148 (2020)

[7] Sayed, M., Ahmed, M., Azlan, W. & Kin, L. Peer to peer solar energy sharing system for rural communities. Cleaner Energy Systems. **7** pp. 100102 (2024)

[8] Dalei, N., Painuly, P., Rawat, A. & Heggde, G. Sustainable energy challenges in realizing sdg 7, Affordable and Clean Energy. Encyclopedia of The UN Sustainable Development Goals. (2021), https://doi.

[9] Raudys, A. & Gaidukevičius, J. Forecasting solar energy generation and household energy usage for efficient utilisation. Energies. **17**, 1256 (2024)

[10] Wang, D., Liu, H., Li, Y., Zhou, G., Zhan, L., Zhu, H., Lu, X., Chen, H. & Li, C. High-performance and eco-friendly semitransparent organic solar cells for greenhouse applications. Joule. **5**, 945-957 (2021)

[11] Dou, Z., Cheng, X., Qin, Z., Wang, K., Xia, W., Qu, Y., Lian, H., Yan, F. & Dong, Q. Solution-processable two-dimensional mose2 quantum dots as a hole transport layer for

highly efficient and stable nonfullerene organic solar cells. Solar RRL. **8**, 2300693 (2024)

[12] Ogundele, A. & Mola, G. Ternary atoms alloy quantum dot assisted hole transport in thin film polymer solar cells. Journal of Physics And Chemistry Of Solids. **171** pp. 110999 (2022)

[13] Oseni, S., Kaviyarasu, K., Maaza, M., Sharma, G., Pellicane, G. & Mola, G. Zno: Cnt assisted charge transport in ptb7: Pcbm blend organic solar cell. Journal of Alloys and Compounds. **748** pp. 216-222 (2018)

[14] Oseni, S. & Mola, G. Properties of functional layers in inverted thin film organic solar cells. Solar Energy Materials and Solar Cells. **160** pp. 241-256 (2017)

[15] Hamed, M., Oseni, S., Kumar, A., Sharma, G. & Mola, G. Nickel sulphide nano-composite assisted hole transport in thin film polymer solar cells. Solar Energy. **195** pp. 310-317 (2020)

[16] Mana, P., Bhujbal, P. & Pathan, H. Fabrication and characterization of zns based photo-electrochemical solar cell. ES Energy & Environment. **12**, 77-85 (2020)

[17] Ogundele, A. & Mola, G. Semiconductor quantum dots as a mechanism to enhance charge transfer processes in polymer solar cells. Chemosphere. **345** pp. 140453 (2023)

[18] McDowell, C., Abdelsamie, M., Toney, M. & Bazan, G. Solvent additives: Key morphology-directing agents for solution-processed organic solar cells. Advanced Materials. **30**, 1707114 (2018)

[19] Liu, X., Li, X., Wang, L., Fang, J. & Yang, C. Synergistic effects of the processing solvent and additive on the production of efficient all-polymer solar cells. Nanoscale. **12**, 4945-4952 (2020)

[20] Ahmed, A., Ike, J., Hamed, M. & Mola, G. Silver decorated magnesium doped photoactive layer for improved collection of photo-generated current in polymer solar cell. Journal of Applied Polymer Science. **140**, 53697 (2023)

[21] Ahmed, A., Hamed, M., Ike, J. & Mola, G. Nickel-doped silver nanoclusters as a mecha-

nism to capture photons. Journal of Materials Science. pp. 1-14 (2024)

[22] Jili, N. & Mola, G. Synergy between light trapping and charge transport for improved collection of photo-current. Advanced Energy and Sustainability Research. pp. 2400114 (2024)

[23] Guo, C., Fu, Y., Li, D., Wang, L., Zhou, B., Chen, C., Zhou, J., Sun, Y., Gan, Z. & Liu, D. A polycrystalline polymer donor as pre-aggregate toward ordered molecular aggregation for 19.3% efficiency binary organic solar cells. Advanced Materials. **35**, 2304921 (2023)

[24] Romanello, M., Napoli, C., Drummond, P., Green, C., Kennard, H., Lampard, P., Scamman, D., Arnell, N., Ayeb-Karlsson, S. & Ford, L. The 2022 report of the lancet countdown on health and climate change: Health at the mercy of fossil fuels. The Lancet. **400**, 1619-1654 (2022)

[25] Lelieveld, J., Klingmüller, K., Pozzer, A., Burnett, R., Haines, A. & Ramanathan, V. Effects of fossil fuel and total anthropogenic emission removal on public health and climate. Proceedings of The National Academy Of Sciences. **116**, 7192-7197 (2019)

[26] Patz, J., Frumkin, H., Holloway, T., Vimont, D. & Haines, A. Climate change: Challenges and opportunities for global health. Jama. **312**, 1565-1580 (2014)

[27] Fu, F., Li, J., Yang, T., Liang, H., Faes, A., Jeangros, Q., Ballif, C. & Hou, Y. Monolithic perovskite-silicon tandem solar cells: From the lab to fab?. Advanced Materials. **34**, 2106540 (2022)

[28] Zhu, L., Zhang, M., Xu, J., Li, C., Yan, J., Zhou, G., Zhong, W., Hao, T., Song, J. & Xue, X. Single-junction organic solar cells with over 19% efficiency enabled by a refined double-fibril network morphology. Nature Materials. **21**, 656-663 (2022)

[29] Zhang, K., Ying, L., Yip, H., Huang, F. & Cao, Y. Toward efficient tandem organic solar cells: From materials to device engineering. ACS Applied Materials & Interfaces. **12**, 39937-39947 (2020)

[30] Wang, J., Zheng, Z., Zu, Y., Wang, Y., Liu, X., Zhang, S., Zhang, M. & Hou, J. A tandem organic photovoltaic cell with 19.6% efficiency enabled by light distribution control.

Advanced Materials. **33**, 2102787 (2021)

[31] Dong, X., Jiang, Y., Sun, L., Qin, F., Zhou, X., Lu, X., Wang, W. & Zhou, Y. Large-area organic solar modules with efficiency over 14%. Advanced Functional Materials. **32**, 2110209 (2022)

[32] Wang, Z., Gao, K., Kan, Y., Zhang, M., Qiu, C., Zhu, L., Zhao, Z., Peng, X., Feng, W. & Qian, Z. The coupling and competition of crystallization and phase separation, correlating thermodynamics and kinetics in opv morphology and performances. Nature Communications. **12**, 332 (2021)

[33] Bi, P., Wang, J., Cui, Y., Zhang, J., Zhang, T., Chen, Z., Qiao, J., Dai, J., Zhang, S. & Hao, X. Enhancing photon utilization efficiency for high-performance organic photovoltaic cells via regulating phase-transition kinetics. Advanced Materials. **35**, 2210865 (2023)

[34] Ding, P., Yang, D., Yang, S. & Ge, Z. Stability of organic solar cells: Toward commercial applications. Chemical Society Reviews. (2024)

[35] Lan, W., Gu, J., Gao, X., Gong, C., Liu, Y., Zhang, W., Sun, Y., Yue, T., Wei, B. & Zhu, F. Efficient and ultraviolet-durable nonfullerene organic solar cells: From interfacial passivation and microstructural modification perspectives. Advanced Materials Interfaces. **9**, 2101894 (2022)

CHAPTER 2

LITERATURE REVIEW

2.1 Introduction

This chapter covers the literature review, which includes the study's conceptual, theoretical, and empirical analysis. The conceptual review identifies key concepts including the relevant ideas, definitions and descriptions of various theories, and models applicable to this study. The theoretical review analyses the frameworks developed in the TFPSCs to understand the status of theoretical knowledge, identify challenges, and suggest possible directions. The empirical review discusses and summarises various findings, about the TFPSCs and SQD in tabular forms. The headway in the development of conducting polymers was the discovery of the first conductive polymer called polyacetylene by Alan Heeger [1], Alan MacDiarmid [2] and Hideki Shirakawa in 1977 [3]. The investigation of chemically doping polyacetylene with bromine led to a significant increase in the conductivity and was rewarded with the Chemistry Nobel Prize in 2000 [4]. This laid the foundation of organic electronics that metamorphosed into the concepts of bulk heterojunction (BHJ) solar cells that have heralded substantial interest in renewable energy for several reasons [5].

2.2 Conductive polymers and organic electronics

Polymers are (natural or synthetic) substances of large, complex molecules formed from long covalent bonded chains of repeating monomers. Natural polymers can be found in nature either produced by living organisms or created through various biological processes in animals, plants, and other organisms. Synthetic polymers derive their sources from man-made processes through intentional chemical processes. Polymers are generally referred to as organic

materials because they are composed of carbon-based molecular structures regardless of their origin. Also, the nature of bonding in polymers ensures the restriction in the movement of free electrons as they are tightly bound within the covalent bonds making them insulators. For instance, conventional polymers have conductivities ranging from 10^{-12} to 10^{-15} S m^{-1} with the band gap (i.e., the distance between the highest unoccupied molecular orbital, HUMO, and lowest unoccupied molecular orbital, LUMO) above 10 eV [6, 7, 8, 9]. Conjugated polymers and conductive polymers can conduct electricity because of the presence of alternating single and double-bond structures along their backbones, which allow the delocalisation of π-electrons, playing an important role in the optoelectronic and electrical conductivity properties of these materials. Conjugated polymers have intrinsic semi-conductivity (moderate conductivity) properties of 1 to 10^{-3} S m^{-1} with a bandgap energy of 3-6 eV, while conductive polymers have enhanced conductivities (up to 10^{3} S cm^{-1}) with bandgap energy of 1-4 eV due to doping [10, 11]. Thus, all conductive polymers are conjugated, but not all conjugated polymers are conductive. Conductive polymers (CP) are polymers with alternating single and double bonds along the polymer backbone, also known as extended π-conjugation systems, with extended conductivities. The extended π-conjugation system enables them to possess mobile charge carriers that enable them to conduct electricity.

The discovery of CPs has since placed them in the spotlight stimulating researchers worldwide to explore their features. Some of the features include ease of preparation, affordable cost of monomers, dielectric, electrical conduction, mechanical flexibility, exciting optical properties (microwave absorption), dual charge transfer (donate or accept electrons), and insignificant environmental hazard [12, 13, 14]. These attributes make CPs important components in electrochemical power sources in developing cost-effective, dependable and ecosystem-friendly energy systems with applications in sensor fabrication, electronics, biomedicals, plastic batteries, light-emitting diodes (LED), supercapacitors, superconductors, fuel cells, organic solar cells, etc. [15, 16, 17, 18, 19, 20, 21]. Therefore, CPs are important ingredients in organic solar energy for the rapid transition into clean energy away from fossil fuels. CPs are synthesised using different methods (see Figure 2.1a) and can be classified based on doping techniques, chemical structure, and their features as shown in Figure 2.1b.

Polymer doping involves the introduction of dopant molecules or ions into the polymer matrix altering the electronic structure that facilitates improved electrical conductivity. This is achieved through induction of charge transfer by creating quasi-particles in the form of

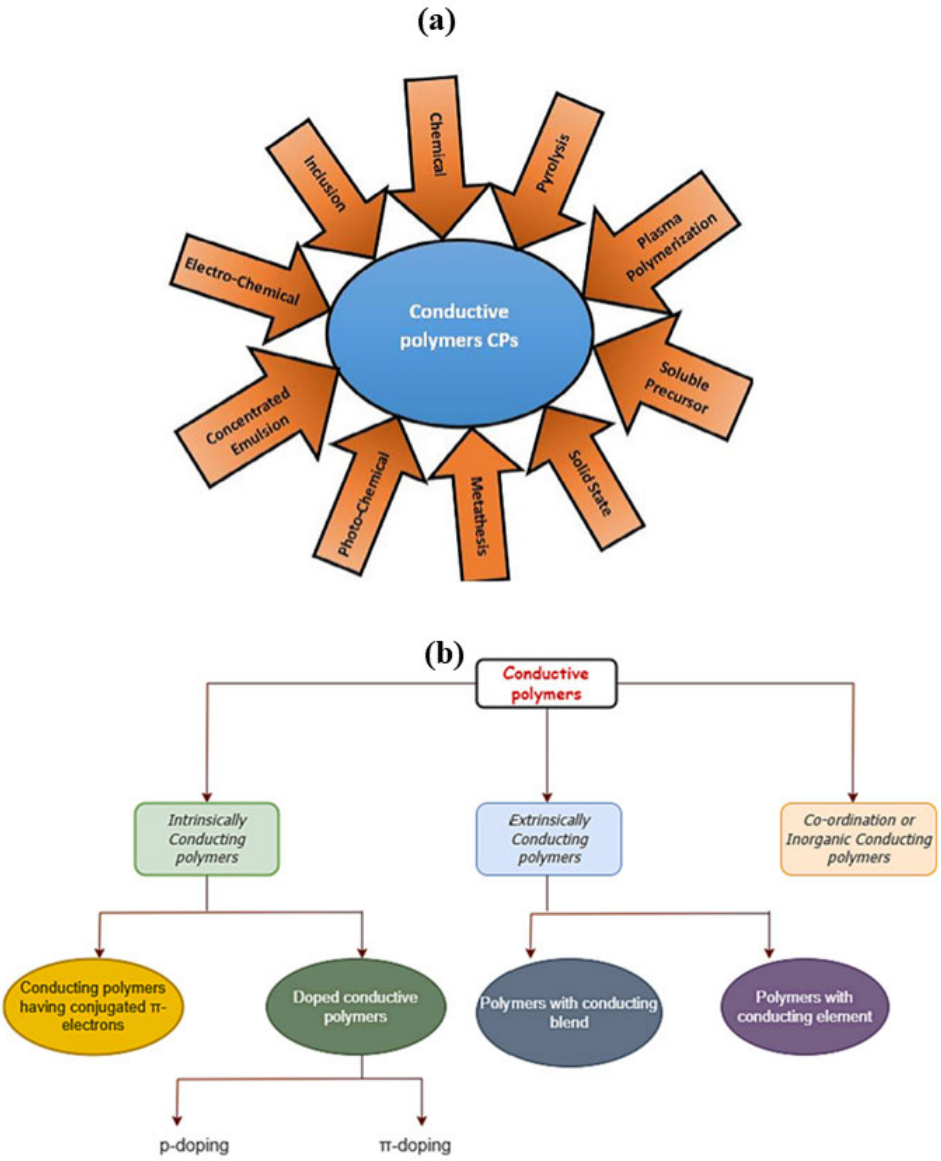

Figure 2.1: (a) Synthesis of conductive polymers via various methods [8] & (b) Classes of conductive polymer [4].

solitons, polarons or bipolarons. These quasi-particles are equipped with a charge and associated distortion that moves along the chain of the polymers enriching the conductivity of the resultant polymers. This process bridges the energy bandgap as shown in Figure 2.2 (i.e., decreasing the LUMO energy levels and increasing the HOMO energy levels). Some of the conductive polymers with intrinsic conductivities include polyphenylene vinylene (PPV), polyacetylene (PA), polypyrrole (PPy), and polyaniline (PANI). Doping is used to achieve electron-rich and electron-deficient polymers. P-type doping involves the removal of electrons from the HOMO matrix of the polymer to the LUMO of the dopant species. This creates a hole in the polymer backbone, leading to the oxidation of the polymer. P-type

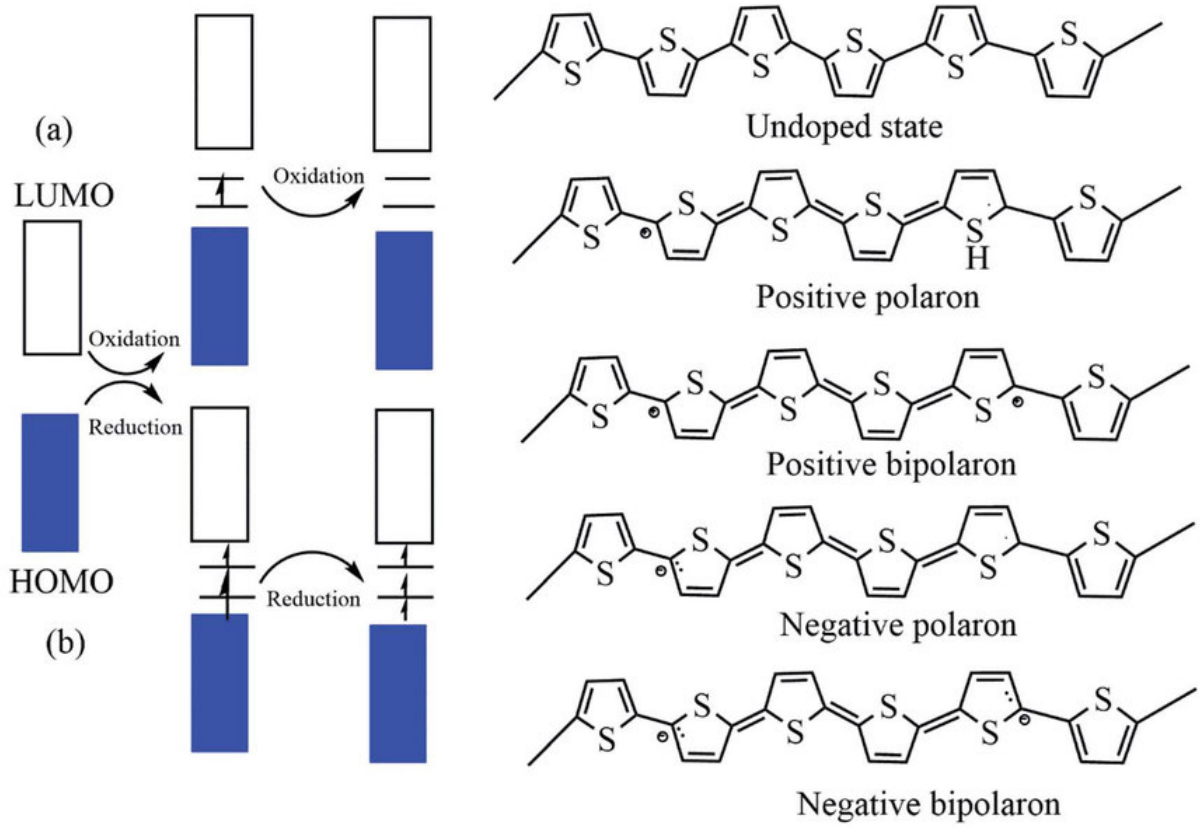

Figure 2.2: The electronic band and chemical structures of polythiophene (PT) with (a) p-type doping and (b) n-type doping [22].

CPs are called donor polymers, having donated electrons to the dopant molecules. Some donor materials are compatible with fullerene-based acceptors, while others are compatible with non-fullerene acceptor materials. Examples of donor polymers used in fullerene acceptors are P3HT - Poly(3-hexylthiophene), PTB7, Poly[[4,8-bis[(2-ethylhexyl)oxy]benzo[1,2-b:4,5-b']dithiophene-2,6-diyl][3-fluoro -2-[(2-ethylhexyl) carbonyl]thieno[3,4-b]thiophenediyl]], PTB7-Th, Poly(4,8-bis(5-(2-ethylhexyl) thiophen-2-yl)benzo[1,2-b:4,5-b']dithiophene-2,6-diyl-alt-(4-(2-ethylhexyl)-3-fluorothieno[3,4-b] thiophene)-2-carboxylate-2,6-diyl). Donor materials used with NFAs include Poly[(2,6-(4,8-bis(5-(2-ethylhexyl)-4-fluorothiophen-2-yl)-benzo[1,2-b;4,5-b']dithiop
hene))-alt-(5,5-(1',3'-di-2-thienyl-5',7'-bis(2-ethylhexyl)benzo[1',2'-c:4',5'-c']dithiophene-4,8-dione))] (PBDB-T-2F), widely known as PM6.

Conversely, the n-type polymer is achieved when the dopant species experiences the movement of an electron from its HOMO to the LUMO matrix of the polymer. This polymer gets reduced in this redox reaction (see Figure 2.2). The n-type CPs are called acceptor polymers

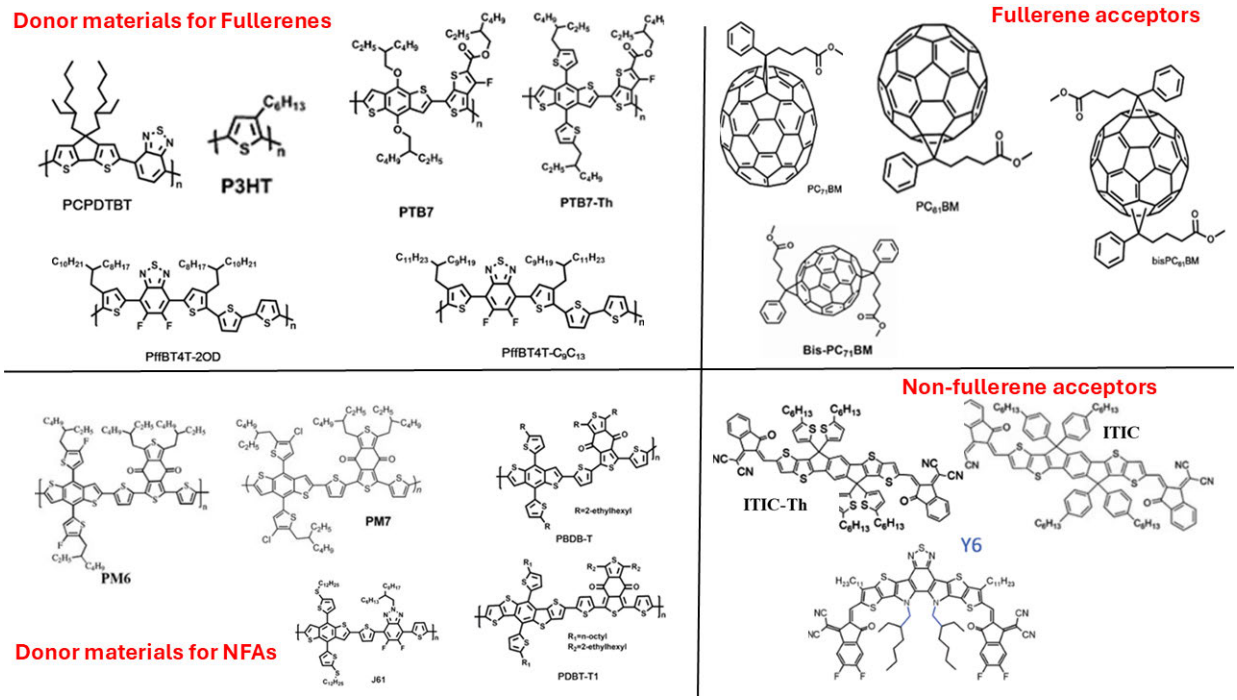

Figure 2.3: Chemical structures of representative donor materials with their various fullerene and non-fullerene acceptors respectively.

due to the gain of electrons from the dopant molecule species. They can be subdivided into fullerene-based and non-fullerene-based acceptors (NFA). NFA employs a wide range of organic molecules and polymers as electron acceptors, while fullerene-based materials are spherical carbon molecules, mainly C_{60} and its derivatives (see Figure 2.3). Fullerenes have rich electron transport characteristics that ensure high charge carrier mobility and excellent electron affinity, aiding effective charge separation compared to the NFAs [23, 24, 25, 26]. On the other hand, NFAs have better morphological stability and a wider absorption spectrum, which assists in harvesting light within a broader range of the solar spectrum. NFAs exhibit lower energy loss and possess more modifiable molecular structures that facilitate solubility and energy level compatibility with donor polymers. They are relatively easier and more cost-effective to synthesise and purify compared to fullerene-based alternatives [27, 28, 29, 30]. Examples of fullerene-based acceptor materials are [6, 6]-phenyl-C_{61}-butyric acid methyl ester ($PC_{61}BM$), [6, 6]-phenyl-C_{71}-butyric acid methyl ester ($PC_{71}BM$), Indene-C_{60} bis-adduct (ICBA), etc. Non-fullerene based acceptor materials include Indacenodithieno[3,2-b]thiophene-C_{60} fullerene adduct (ITIC), Indacenodithieno[3,2-b]thiophene-C_{60}-Thieno[3,2-b]thiophene (ITIC-Th), and 2,2'-((2Z,2'Z)-((12,13-bis(2-butyloctyl)-3,9-diundecyl-12,13-dihydro-[1,2,5]thiadiazolo[3,4-e]thieno[2,2-g]thieno[2,3-b]indole-2,7-diyl)bis(methanylylidene))bis(5,6-difluoro-3-oxo-2,3-dihydro-1H-inden-1-ylidene))dimalononitrile, also known as BTP-4F or Y6. Some of the

representative chemical structures of donor materials applicable to fullerene and non-fullerene acceptors respectively are shown in Figure 2.3.

2.2.1 Mechanism of electrical conduction in polymers

Electrical conduction in conductive polymers (CPs) occurs through various mechanisms and can be influenced by the types and structures of the polymers. For instance, conjugate polymers (also known as intrinsic conducting polymers-ICP) exhibit intrinsic electrical conductivity arising from the presence of single and double bonds in their conjugated structures. ICP conductivities can be enhanced by disruption of delocalisation of π-electrons via hopping conduction. This process leads to a surge in the charge carriers (electrons or holes) enabling them to hop between localised sites (various defects or impurities or varied structural sites) in the polymer matrix. Another way of increasing conduction is through blended or composite polymers. The blended polymers can be made from donor-acceptor polymers like P3HT:PCBM, and PM6:Y6 to achieve better electrical conductivities. Similarly, composite polymers involve the use of a foreign component nanoparticle like carbon nanotube (CNT), SQD in the blended polymers to achieve better electrical conduction [31, 32, 33, 34, 35]. The foreign component material acts as a conduction filler through the material, enhancing the conductivity of the materials. They also create conductive pathways within the matrix of the polymers by enabling free movement of electrons. The optimal concentration of a conduction filler determines the percolation threshold required to form a favourable conductive network in the materials [25]. Generally, the electrical conduction in polymers is dependent on some factors like temperature, mobility of carriers, morphology, (crystallinity of the polymers, molecular weight), environmental conditions (relative humidity, choice solvent), and doping level [36, 37, 38]. The mathematical consequence of conduction is further illustrated with equation (2.1). This shows that the conductivity (σ) is directly proportional to the carrier concentration (n), and carrier mobility (μ), (where e is an electronic charge),

$$\sigma = ne\mu. \tag{2.1}$$

The conventional or undoped polymer has a high energy gap, leading to low carrier concentrations that result in low intrinsic conductivity even when the polymer is equipped with high carrier mobility. The carrier concentration can be enhanced through various levels of doping, while the mobility of carriers can be improved by raising the temperatures and improving the polymer's structural attributes, as demonstrated by the Arrhenius-type temperature depen-

dence equation (2.2) below.

$$\mu(T) = \mu_0 e^{-\frac{E_a}{k_B T}}, \tag{2.2}$$

where $\mu(T)$ is the mobility at temperature T, μ_0 is the mobility at a pre-exponential factor, k_B is Boltzmann's constant, T is the absolute temperature, and E_a is the activation energy. Specifically, if conduction in polymers is dominated by hopping, the hopping conduction is guided by the following Mott's variable range hopping (VRH) model equations (2.3), (2.4) and (2.5) for 1, 2, and 3-dimensional systems respectively [39]:

$$\sigma(T) = \sigma_0 e^{-(T_0/T)^{1/2}}, \tag{2.3}$$

$$\sigma(T) = \sigma_0 e^{-(T_0/T)^{1/3}}, \tag{2.4}$$

$$\sigma(T) = \sigma_0 e^{-(T_0/T)^{1/4}}, \tag{2.5}$$

where $\sigma(T)$ is the conductivity at temperature T, σ_0 is the conductivity at a pre-exponential factor that is weakly dependent on the temperature, T is the absolute temperature, and T_0 is the characteristic temperature, which depends on the density of states at the Fermi level and the localisation length, given by equation (2.6) below.

$$T_0 = \frac{\beta}{k_B N(E_F) \xi^3}, \tag{2.6}$$

where β is a numerical constant that depends on the specific hopping mechanism and dimensionality, $N(E_F)$ is the density of states at the Fermi level, and ξ is the localisation length, which describes the spatial extent of the localized electronic states. Moreover, the conduction in polymer-composites is also guided by a relevant composite conduction equation that takes into account conductive fillers using power law percolation theory for 3-dimension given by equation (2.5) [40, 41] to achieve equation (2.7).

$$\sigma_{\text{eff}} = \sigma_m (p - p_c)^t, \tag{2.7}$$

where $\sigma(m)$ is the matrix conductivity (conductivity of the polymer without fillers, p is the volume fraction of the conductive filler, p_c is the percolation threshold (the critical volume fraction at which the composite starts to conduct and p_c . Generally, the mathematical implications of various factors regulating electrical conductivity in polymers and polymer composites showed that the temperature dependency on ICPs and ionic conductors. This can be appraised with Arrhenius-type equations, while hopping-dominated conductivity requires the use of various (VRH) model equations. The morphological factor also revealed that the arrangements of chains along the polymer influence the mobility and conductivity. Analogously, the degree

of doping affects charge carriers' density which has a linear or near-linear relationship with conductivity. A conscious mastery of these concepts and their mathematical implications is invaluable in optimizing the synthesis of polymers and composite fillers, as well as in designing and fabricating different devices. The advantageous properties of p-type and n-type polymers are investigated in polymer solar cell technology by combining their features to create bulk heterojunction (BHJ) polymer solar cells.

2.3 Polymer solar cells

Polymer solar cells (PSCs) involve the design, synthesis, characterisation, and application of conductive polymers (or organic small molecules) to generate electricity via the photovoltaic effect. The organic molecules (polymers) employed in TFPSCs are electronically tunable, lightweight, flexible, semi-transparent, solution-processable, and cost-effective [42, 43, 44, 45, 46, 47]. They have great potential for mass production due to for various reasons, including continuous improvements in their PV metrics, with PCE currently above 19% [48, 49, 50, 51]. Due to their high optical absorption coefficients, they can absorb large amounts of sunlight with materials that have a thickness in the nanometer range. Likewise, they produce lower environmental hazards during manufacturing and operation processes. The main challenges inhibiting their large-scale production are low power conversion efficiency PCE and limited shelf lives. Compared to the matured inorganic solar cells, which have robust PCEs and longer lifespans, these are shortcomings. However, matured inorganic solar cells have huge fabrication costs due to infrastructural requirements like a clean room, cumbersome manufacturing, and energy-intensive processes [52, 53, 54, 55]. These factors contribute to the challenge of making established inorganic solar cells a reliable alternative to fossil fuels. There are three functional layers in PSCs: electron transport layer (ETL), photoactive layer, and hole transport layer.

The photoactive layer metamorphosed from a single layer (a single component of an organic polymer layer is placed between two electrodes) at the early stage between the 1950s and 1980s [56] to the bilayer (the use of a distinct polymer donor layer and a distinct polymer acceptor layer placed between front electrode and back electrode) in the late 1980s and early 1990s. The invention and development of BHJ in the mid-1990s can be largely attributed to the pioneering works of Alan MacDiarmid, Hideki Shirakawa, and Hideki Shirakawa on conducting polymers and organic electronics. The developments in organic photovoltaic (OPV) gave rise to BHJ. Likewise, BHJ have continued to birth other methods like tandem organic solar cells which is the stacking of two or more different cells on top of each other. Tandem organic solar cells

can be classified into homo-tandem OSC - stacking of two or more similar cells and hetero-tandem OSC - stacking of different cells. The tandem OSC have multiple BHJ depending on the number of sub-cells. The design architecture involved in TFPSCs can be categorised into conventional and inverted architecture.

2.4 Bulk Heterojunction polymer solar cells

Bulk heterojunction (BHJ) polymer solar cells' revolutionary advancement in the field of renewable energy is one of the immediate derivatives of the invention of conducting polymers. BHJ has improved the PV metrics of solar cell technology. It represents a significant improvement over single and bilayer layers that have been used as solar absorbers producing better PV metrics [57, 58, 59, 60]. This process entails optimally blending an organic polymer donor

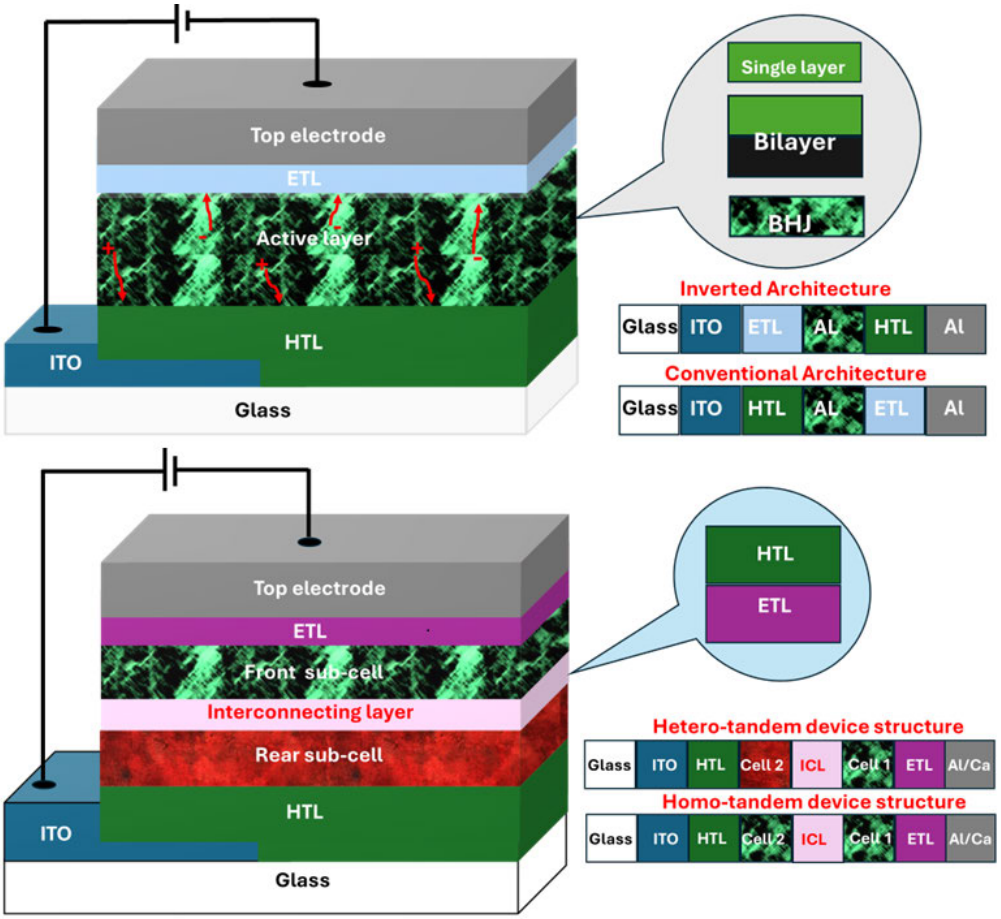

Figure 2.4: Schematic diagrams for single layer, bilayer, single BHJ and multiple BHJ (tandem) TFPSCs and their architectures.

with a polymer acceptor material (either fullerene or NFA) to create the solar cell's photoactive layer, which is then positioned between the front and back electrodes. The electrodes are

shielded from direct contact with the photoactive layer with the use of a buffer layer which can be a hole transport layer (HTL) or an electron transport layer (ETL) as shown in Figure 2.4. The donor-acceptor blend produces nanoscale inter-percolation pathways which assist the dissociation of excitons, efficient charge carriers' separation and collection of charges at their respective electrodes via enhanced interface area between donor and acceptor layers. This design applies to single, bilayer, tandem and BHJ TFPSCs as shown in Figure 2.4.

2.4.1 Design and working principle of BHJ polymer solar cells

The modes of operation in BHJ polymer solar cells can be divided into five processes. These are the absorption of photons and generation of excitons, diffusion of excitons, dissociation of excitons, transport, and collection of charge carriers at the electrodes as shown in Figure 2.5. Upon absorption of a photon with energy that is in the order of the band gap of the

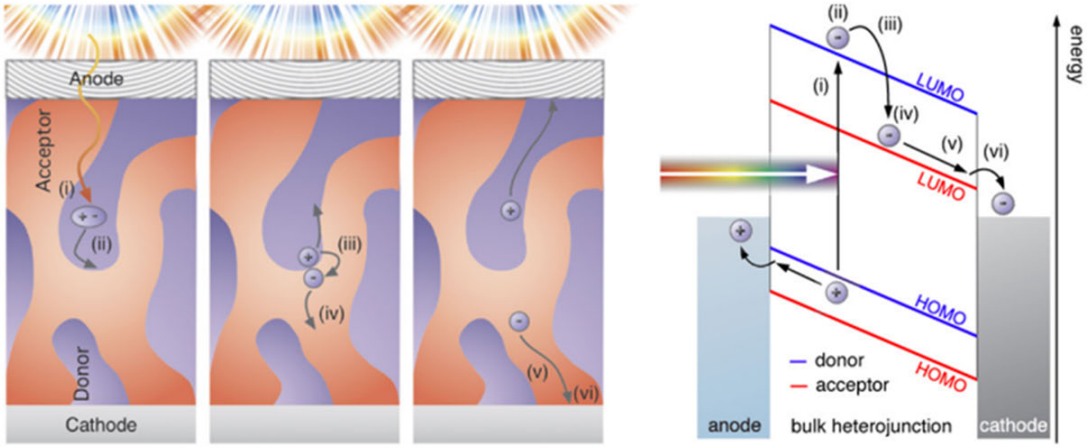

Figure 2.5: Donor-acceptor polymer matrix blend and sequential working processes of BHJ polymer solar cells [61].

semiconductor (donor material), an exciton (a bound electron-hole pair) is generated (stage i). Within a short lifetime, the exciton reaches the donor-acceptor interface (stage ii) where it is dissociated into interfacial charge carriers via the charge transfer (CT) process (stage iii). At this point, the electron occupies the LUMO energy level of the acceptor domain while the hole remains at the HOMO energy level of the donor phase, weakly bound by the Coulomb force. The weakly bound excitons by Coulomb's attractive force [62, 63] are then spatially separated by an in-built electric field of the device associated with the difference in the work function of the anode and cathode electrodes (stage iv). At this point, those excitons that cannot be separated contribute to geminate energy loss (see section 2.6.1). Excitons that successfully undergo interfacial dissociation and separate into free charge carriers are transported towards

their respective electrodes through ineffective hopping from one localised state to another within the polymer matrix (stage v). This contradicts the effective band transport observed in crystalline semiconductors [61]. Again, at this stage (v), some of the separated charge carriers are lost via non-geminate recombination (see section 2.6.2) by injection into the organic matrix blend. The stage (vi) depicts the photogenerated charges successfully collected at their respective electrodes.

2.5 Characterisation of polymer solar cells

2.5.1 J-V characteristics

The performance of TFPSC can be accessed by measuring the J-V characteristics under dark and illuminated conditions using a solar simulator. The J-V curve under illumination conditions provides a deep understanding of important parameters like short-circuit current (J_{sc}), maximum power point current density (J_{MPP}), open circuit voltage (V_{oc}), maximum power point voltage (V_{MPP}). These parameters can be used to determine the power conversion efficiency, (PCE), fill factor (FF) and maximum power of the solar cells as shown in Figure 2.6a. In the same vein, the J-V curve under dark conditions extracts crucial information (Figure 2.6b) about the quality of the TFPSCs. For instance, a significant amount of leakage current could point towards defects in the active layer while the lower amount of dark current in the forward bias condition is either a sign of poor contact between the active layer/buffer layer/electrodes or inefficient transport of charge carrier from the active layer to the electrodes [64]. The series and shunt resistances can be determined from the J-V curve under dark conditions. The series resistance is evaluated from the tangent on the forward bias side of the illumination curve. Also, the shunt resistance is evaluated from the tangent on the reverse bias side of the dark condition curve, as revealed in Figure 2.6b. Moreover, the difference between the illumination current (J_L) and dark current (J_D) gives photocurrent density (J_{ph}). The plot of J_{ph} against V_{eff} (where $V_{eff} = V_o - V_{app}$, and V_o is the voltage corresponding to the point when $J_L - J_D = 0$) can be used to analyze the events occurring at different stages of the working mechanism of TFPSCs (see Figure 2.6c). The J_{ph} vs. V_{eff} plot is divided into three regimes, namely linear, transition, and saturation regimes. In the linear regime, a low injection level of photogenerated charge carriers is driven by an electric field created by the applied voltage, leading to an increase in current that varies linearly with the applied voltage. The transition regime operates at a higher voltage than the linear regime, with the rate of increase in photocurrent slowing down. At this point, almost all the photogenerated carriers dissociate into

free charge carriers until they reach the plateau point, preceding the onset of the saturation regime. The saturation regime is characterized by the leveling of the photocurrent density, with almost all the photogenerated free charge carriers being collected at this point. Beyond this point, a further increase in the effective voltage leads to a negligible rise in J_{ph}. Other parameters that can be evaluated from the curve are the saturation current (J_{sat}), maximum exciton generation ($G_{\text{max}} = \frac{J_{\text{sat}}}{qL}$, where L is the active layer thickness and q is the electronic charge), and the probabilities of charge dissociation (η_{diss}) and collection (η_{coll}) evaluated using $\frac{J_{\text{ph}}}{J_{\text{sat}}}$ under short-circuit and maximum power point conditions, respectively [65]. The pink rectangle with coordinates ($V_{\text{MPP}}, J_{\text{MPP}}$) signifies the maximum power delivered by TFPSCs in Figure 2.6a, while the grey square represents the product of J_{SC} and V_{OC}. The fill factor is the ratio of the maximum power delivered by the TFPSCs to the product of open circuit voltage and short-circuit current density, as shown in equation (2.8):

$$FF = \frac{P_{MPP}}{V_{oc} \times J_{sc}} = \frac{J_{MPP} \times V_{MPP}}{V_{oc} \times J_{sc}}, \tag{2.8}$$

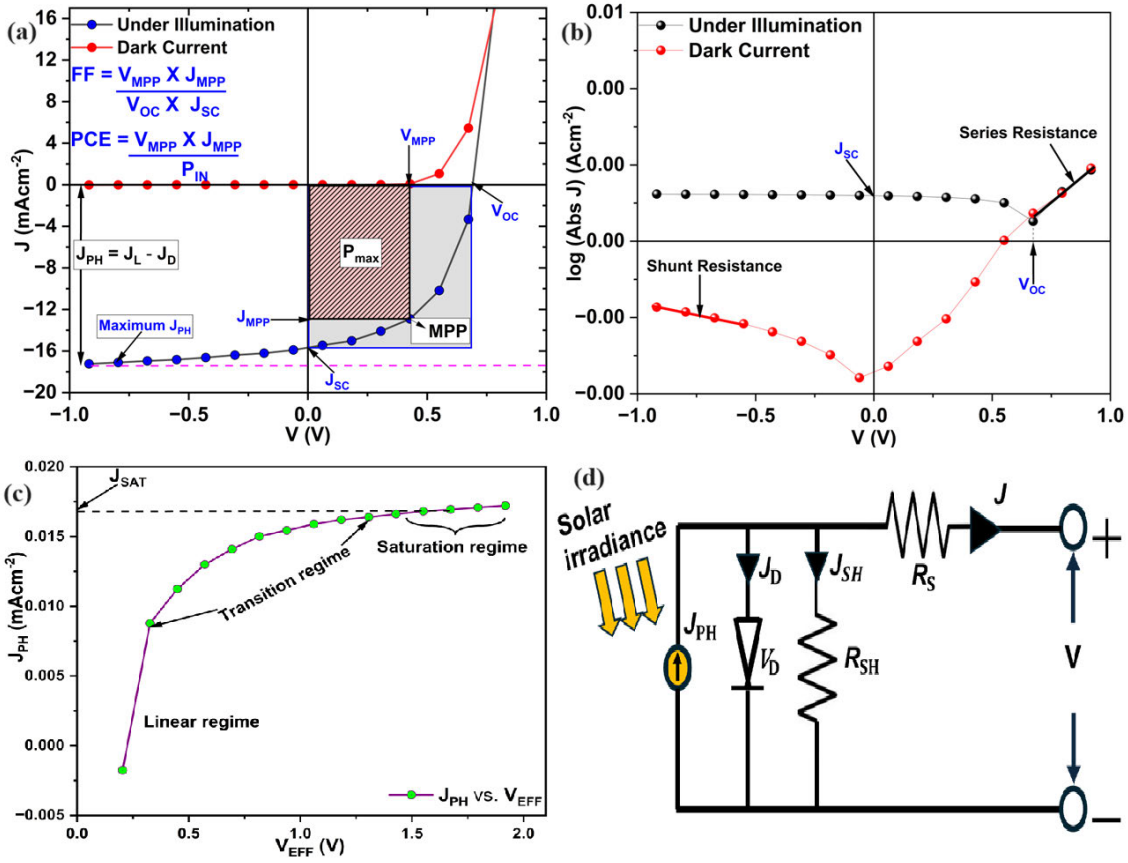

Figure 2.6: (a) Linear (b) Semilogarithmic schematic J-V characteristics (c) Photocurrent vs. voltage and (d) Equivalent circuit diagram of a typical bulk heterojunction solar cell.

An ideal TFPSC (without parasitic resistors) with values of V_{MPP} and J_{MPP} approximately equal to those of open circuit voltage and short circuit density respectively has a unity FF and a perfect square. Hence, the fill factor measures the squareness and quality of TFPSC J-V characteristics. A solar cell's power conversion efficiency (PCE) is the ratio of the maximum extractable power output P_{MAX} to the incident optical power radiated by the sun P_{sun} (usually got from air-mass (AM) 1.5 G solar simulator radiating at 1000 Wm^{-2}, mathematically denoted in equation (2.9):

$$\mathrm{PCE} = \frac{P_{\mathrm{max}}}{P_{\mathrm{sun}}} = \frac{V_{\mathrm{MPP}} \times J_{\mathrm{MPP}}}{P_{\mathrm{sun}}} = \frac{V_{\mathrm{OC}} \times J_{\mathrm{SC}} \times FF}{P_{\mathrm{sun}}}. \tag{2.9}$$

Equation (2.9) implies that a good solar cell depends on these three vital parameters, V_{OC},J_{SC}, and FF. Figure 1.6d gives a schematic equivalent circuit diagram of a typical solar cell, the Shockley diode equation was initially derived from inorganic devices but has been modified to cater for the photocurrent J_{ph}, shunt resistance R_{SH}, and series resistance R_{S} in the solar cell circuit. The ideal diode equation (2.10) can be used to achieve a peculiar equation for the Shockley equation for solar cells:

$$J_D = J_0 \left(e^{\frac{V_D}{nV_T}} - 1 \right), \tag{2.10}$$

where J_{D} is current density through the diode, J_0 is reverse saturation (or dark) current density, n is the ideality factor, V_{D} is the voltage across the diode, and V_{T} is thermal voltage (given by $V_T = \frac{K_B T}{q}$ is Boltzmann's constant, T is the absolute temperature and q is the elementary charge). From Figure (2.6), the current, (J) through the solar cell under illumination conditions is the difference in the photon-current J_{ph} and current through the diode J_{D} given by equation (2.11):

$$J = J_{\mathrm{ph}} - J_D - J_{\mathrm{SH}} = J_{\mathrm{ph}} - J_0 \left(e^{\frac{V_D}{nV_T}} - 1 \right) - J_{\mathrm{SH}}. \tag{2.11}$$

The voltage drops across the series resistance (R_{S}) in the circuit account for the difference in the terminal voltage V and the diode voltage (V_{D}) given by V_{D} =V+JR_{S}. On the other hand, the current through the shunt resistance (R_{SH}) is given by $J_{\mathrm{SH}} = \frac{V + JR_S}{R_{\mathrm{SH}}}$. Substituting the expression for the V_{D} and J_{SH} into equation (2.11) yields equation (2.12) below:

$$J = J_{\mathrm{ph}} - J_0 \left(e^{\frac{V + JR_S}{nV_T}} - 1 \right) - \frac{V + JR_S}{R_{\mathrm{SH}}}. \tag{2.12}$$

The equation (2.12) represents the practical solar cell equation with parasitic resistances (R_{SH} and R_{S}). When the output terminal of the equivalent circuit is short-circuited, the output voltage becomes zero, and then we have the maximum short-circuit current represented as

(J_{SC} and the equation (2.12) changes to equation (2.13):

$$J_{\mathrm{SC}} = \frac{1}{1+\frac{R_S}{R_{\mathrm{SH}}}}\left[J_{\mathrm{ph}} - J_0\left(e^{\frac{J_{\mathrm{SC}}R_S}{nV_T}} - 1\right)\right]. \tag{2.13}$$

If the equivalent circuit is open, no current flows through it and the output voltage is maximum corresponding to open-circuit voltage (V_{OC} as shown in equation (2.14):

$$V_{\mathrm{OC}} = nV_T \ln\left(1+\frac{J_{\mathrm{ph}}}{J_0} - \frac{V_{\mathrm{OC}}}{J_0 R_{\mathrm{SH}}}\right). \tag{2.14}$$

If the thermal voltage is much greater than the voltage dropped across the series resistance, $V_T \gg J_{\mathrm{SC}}R_S$, the short-circuit current density becomes approximately equal to the photocurrent, $J_{\mathrm{SC}} \approx J_{\mathrm{ph}}$. This indicates that the quality of the solar cell is high, operating in a near-ideal condition with very insignificant resistive losses and high efficiency.

In the same vein, if the shunt resistance is large such that $R_{SH} \to \infty$, equation (2.14) becomes equation (2.15) below.

$$V_{OC} = nV_T \ln\left(1+\frac{J_{\mathrm{ph}}}{J_0}\right) = n\frac{k_B T}{q} \ln\left(1+\frac{J_{\mathrm{ph}}}{J_0}\right). \tag{2.15}$$

Generally, J_{SC} depends on the solar cell's level of solar irradiance, defined area, and material characteristics while V_{OC} varies strongly with the temperature, and the quality of the material used in the solar cell. A practical solar cell approaching a near-ideal solar cell must therefore have a very high shunt resistance tending to infinity to reduce the leakage current to as low as possible. Also, its series resistance must tend to zero to maximise short-circuit current density.

2.5.2 Spectral response of PSCs

The spectral response $S(\lambda)$ of a solar cell to a single-wavelength light (monochromatic spectral response) is the ratio of the photocurrent density J_{ph} of the solar cell to the irradiance intensity I, which is usually about 1000 $\mathrm{W/m^2}$. This knowledge is often used in spectroscopy instruments for the calibration of light of specific wavelengths to achieve accurate sensitivity. The mathematical relation for spectral response is given by equation (2.16):

$$S(\lambda) = \frac{J_{\mathrm{ph}}(\lambda)}{I(\lambda)}. \tag{2.16}$$

The FTIR also gives crucial information about the interaction of molecular composition of the functional layer (electron transport layer, hole transport layer or active layer) of polymer solar cells and their response to infrared light. For instance, the absorption spectrum or emission spectrum in the infrared region can be used to appraise the performance of solar

cells. This proves very useful when the PSC functional layer is doped with a foreign component nanoparticle or quantum dot [66, 67, 68, 69]. The FTIR extract information from the plot of infrared light intensity vs. wavelength of light. FTIR information assists in comparing the spectral response of the modified functional layer to the pristine device without a foreign component material. External quantum efficiency (EQE) can also be used to measure the spectral response of PSCs [70, 71]. It measures the rate of conversion of absorbed photons into electric charge carriers by comparing it with the total incident light reaching the solar cell. It is mathematically represented by equation (2.17):

$$\mathrm{EQE}(\lambda) = S(\lambda)\frac{h\nu}{q} = \frac{\text{number of electrons collected}}{\text{number of incident photons}} = \frac{J_{\mathrm{ph}}(\lambda)}{q\varphi_{\mathrm{in}}(\lambda)}, \tag{2.17}$$

where h is Planck's constant, ν is the photon frequency ($\nu = \frac{c}{\lambda}$), c is the speed of light, q is the elementary charge, and $\varphi_{\mathrm{in}}(\lambda)$ is the incident photon flux at wavelength λ measured in photons $\mathrm{m}^{-2}\mathrm{s}^{-1}$. An EQE measurement system like the PV measurement QEX series can measure the EQE. The internal quantum efficiency (IQE) can also be used to appraise the spectral response of solar cells at the initial stage compared to the EQE. It measures the rate at which the solar cell can absorb the incident photons. It is the ratio of the number of photons collected to the number of photons absorbed by the solar cells. It is given mathematically by equation (2.18):

$$\mathrm{IQE}(\lambda) = \frac{\text{number of electrons collected}}{\text{number of absorbed photons}} = \frac{\mathrm{EQE}(\lambda)}{1-R(\lambda)-T(\lambda)}, \tag{2.18}$$

where $R(\lambda)$ is the reflectance at wavelength λ, representing the amount of incident light reflected at the solar cell surface. $T(\lambda)$ is the transmittance at wavelength λ, denoting the amount of incident light that passes through the solar cells and is potentially absorbed. IQE evaluation can therefore assist in identifying possible loss mechanisms before the photon are collected.

Importantly, photoluminescence (PL) intensity measurement of functional layers in thin-film polymer solar cells (TFPSCs) can be used to investigate the emission of light excited at a particular wavelength using a PL spectrophotometer. The information obtained from PL output can assist in selecting the appropriate foreign component material needed in the solar cells. Foreign component materials are commonly referred to as third component materials when doped in active layer. They include semiconductor quantum dots, plasmonic materials, and transition metal chalcogenides among others.

For instance, materials exhibiting downward conversion photoluminescence (DCPL) properties

can absorb high-energy photons and re-emit at lower energy (infrared region), thereby extending the solar spectrum and harvesting more photons for electricity conversion [72, 73, 74]. Similarly, PL is used to investigate upward conversion photoluminescence (UCPL), a phenomenon where lower energy photons are absorbed, converted into higher energy photons, and re-emitted at shorter wavelengths. This can be accomplished by incorporating rare-earth ions into the functional layer of TFPSCs [75, 76, 77, 78]. Additionally, PL can be used to investigate quenching in thin-film solar cells by observing the transfer of energy from the donor polymer to the acceptor, noted by a decrease in PL intensity of the emitted light.

2.6 Mechanism of energy loss in PSCs

The processes of energy loss in thin film polymer solar cells can be linked to different phases of the charge transfer processes involved in solar energy conversion. The most underlying loss mechanisms are transmission and thermalisation losses in both organic and inorganic-based solar cells. Transmission loss is a preliminary loss that occurs at the initial stage of photon absorption. It occurs when the absorbed photon energy is lower than the bandgap energy of the solar material. In this case, photocurrent can hardly be produced since no exciton is generated. Thermalisation losses are traceable to the secondary stages when photons with much higher energy than the energy band gap of the material are absorbed. They occur when photons with higher energy than the band gap are absorbed and generate hot excitons that rapidly relax to the solar cell materials' band edge, losing the excess energy as heat or by emission of light. The transmission loss limits the short-circuit current while the thermalisation loss accounts for the limitation of (V_{OC}). The losses associated with a successful absorption of photons are generally related to either the recombination or poor contact at the electrodes. Poor contact at the electrode interface can lead to energy loss via parasitic resistances (high series resistance and/or low shunt resistance) or energy mismatch of the work function of electrodes. Aside from the fundamental losses associated with the thresholds of absorbed photons from the sun. The other losses are associated with the recombination of charge carriers before, during, or after excitons have dissociated into free carriers at any of the stages listed in the working principle of solar cells. The losses are accompanied by the emission of light (radiative loss), the release of heat (non-radiative loss), or both. The recombination can be broadly categorised into geminate, non-geminate, and trap-assisted recombination in organic or polymer solar cells. These types of recombination are also found in inorganic solar cells.

2.6.1 Geminate recombination

The recombination of charge carriers from the same pairs of generated excitons upon absorption of light before dissociating into free charge carriers at the interface is referred to as geminate recombination. The hole-electron pairs are produced from the same source via the absorption of photon energy greater than the bandgap of organic material. The geminate recombination can be accompanied by the emission of photons (radiative) or dissipation of heat (non-radiative). In polymer solar cells, the radiative geminate recombination can be less detrimental if the emitted photons are re-absorbed otherwise, it can limit the photoluminescence thereby reducing the efficiency. Conversely, the non-radiative geminate recombination is more detrimental because it is not accompanied by the emission of photons but rather dissipates heat via lattice vibrations or defects in the materials. Ultimately, non-radiative geminate recombination is more detrimental to the performance of organic solar cells. Therefore, geminate recombination limits the number of excitons available for dissociation into free-charge carriers which reduces the possible short-circuit current that could eventually be produced at the end of the working cycle of PSC. The limitation of (J_{SC}) eventually reduces power conversion as shown in equation (2.8). The geminate recombination adversely affects the fill factor [79] and the parasitic resistances, characterised by high series resistance and low shunt resistance [80]. The increased series resistance reduces the possible maximum point voltage because of a large voltage drop across (R_S) while the low shunt (R_{SH}) resistance accounts for increased leakage current reducing the short circuit current. Eventually, the various cell parameters like FF and PCE are negatively impacted by the presence of geminate recombination since there is a reduction in the power point voltage and power point current that determine the fill factor of the PSCs (see equations (2.8) and (2.9)). Since the recombination originates from a unique bounded exciton which does not need the existence of additional carriers, the geminate recombination is not considered as bimolecular recombination.

2.6.2 Non-Geminate recombination

Non-geminate recombination occurs after the initially generated bounded excitons have dissociated into free charge carriers. The dissociated charge carriers from different pairs of excitons encountering one another in the materials recombine without being generated from the same pairs. This type of recombination is also called bimolecular recombination. Again, this type of recombination can be accompanied by either the emission of photons (radiative) or the release of heat (non-radiative). The radiative non-geminate recombination is not desirable in solar

cells because it decimates the available energy of carriers. However, the non-radiative loss in non-geminate recombination is more detrimental to the performance of organic solar cells than radiative because the recombined hole-pairs energy is converted into phonon vibrational energy. The Langevin recombination concept can be used to further illustrate non-geminate recombination [81] as shown in Figure 2.7 . This recombination is explained by the Langevin recombination rate (L_R) with the equation (2.19) [61]:

$$L_R = \beta(np - n_i^2), \tag{2.19}$$

where p, and n are the number of carriers per unit volume of holes and electrons, respectively n_i is the intrinsic carrier per unit volume. The Langevin recombination prefactor β can be expressed with equation (2.20) below:

$$\beta = \frac{q(\mu_p + \mu_n)}{\varepsilon}, \tag{2.20}$$

where ε is the permittivity of the medium ($\varepsilon = \varepsilon_0\varepsilon_r$), ε_0 is the permittivity of free space, ε_r is the dielectric permittivity of the material, μ_p and μ_n are the carrier mobilities of holes and electrons, respectively. Staudigel *et al* [82] modified equation (2.19) to accommodate recombination at the interface ($L_{R_{\text{int}}}$) given by equation (2.21):

$$L_{R_{\text{int}}} = \gamma\beta\left(n^D p^A - n_0^A p_0^D\right), \tag{2.21}$$

where γ ranges from 10^{-4} to 10^{-1} for BHJ, n^D and p^A are the electron and hole densities in the donor and acceptor materials, respectively; n_0^A and p_0^D are the intrinsic densities of electrons and holes in the donor and acceptor materials, respectively. The bimolecular recombination

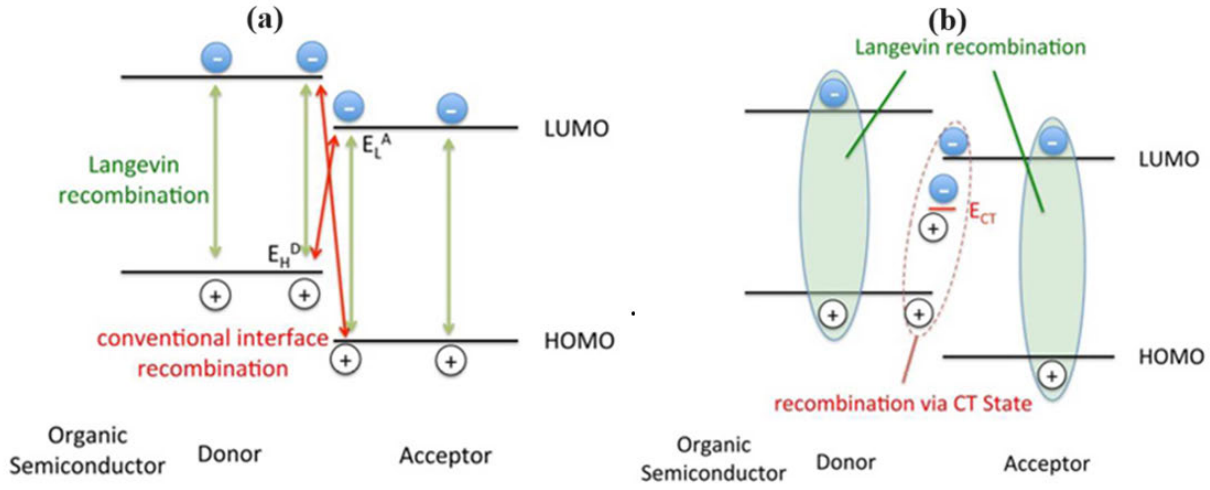

Figure 2.7: Schematic of (a) HOMO-LUMO energy level heterointerface diagrams for polymer solar cell and (b) bimolecular interface recombination [81].

at the interface between electrons and holes is directly proportional to the product of the electron and hole carrier concentrations in the donor and acceptor materials ($n^D p^A$), which are greater than the intrinsic concentration product ($n_0^A p_0^D$). The non-geminate recombination energy loss limits the short-circuit current due to a decrease in the volume of charge carriers reaching the electrodes for current conduction. Non-geminate recombination of charge carriers often leads to splitting quasi-Fermi levels, causing an energy mismatch that reduces the open-circuit voltage. Therefore, organic solar cell PV metrics (PCE and FF) are reduced due to non-geminate recombination. The routes to mitigate and regulate the adverse effects of non-geminate recombination include the design and utilisation of narrow bandgap non-fullerene acceptors and solvent-additive strategies [83, 84].

2.6.3 Trap-assisted recombination

It occurs due to impurities in the material involving one of the charge carriers. The different types of material defects act as trap sites for charge carriers. This type of recombination can be both monomolecular and bimolecular. This type of recombination is associated with both geminate and non-geminate recombination because of the defects in the materials. In the case of geminate recombination, the bound neutral exciton is captured by the trap (or localised state) in the material. This can be referred to as monomolecular trap-assisted recombination. However, in the case of trap-assisted non-geminate recombination, the free carriers can be captured at the trap sites individually before or after recombination. Since these pairs of hole-electrons are independently generated from different excitons, it can be referred to as bimolecular trap-assisted recombination. This type of recombination is more pronounced in inorganic semiconductor materials with quantum sizes because of the discrete energy levels. This can be largely mitigated using high-purity materials, improved surface morphology and efficient interfacial engineering.

2.6.4 Contact-loss

This phenomenon can occur at a low electric field during the working mechanism of the solar cells. At a low electric field, there is competition between the drift photogenerated carriers and the diffusion of photogenerated carriers. The diffused photogenerated carriers are ion random motion determined by generation gradient, this leads to some of the holes and electrons being collected at the wrong electrodes. This set of photogenerated carriers does not lead to the conduction of current and reduces the net current since only a few drift photogenerated carriers are available leading to a small current. However, if the electric field is high, the

photogenerated carriers are extracted by drifting towards the electrodes. The contact loss can be greatly reduced by choosing electrodes with the right work function and ensuring good contact at the electrodes.

2.6.5 Auger recombination

This type of recombination is less prominent in organic solar cells but very prominent in inorganic materials. It occurs when a conduction band (CB) electron with high energy transfers its excess energy to another CB electron. The first electron relaxes to the ground level after losing its energy due to phonon interaction (non-radiative mode) and recombines with a hole the hole in the valence band (VB). The excess energy released is therefore converted to heat rather than emitting light (non-radiative). The newly generated carrier gets excited to a higher energy state within the CB interface of the donor and acceptor. It eventually relaxes to a lower level after dissipating its excess energy as heat within the material. Ultimately, the Auger recombination decimates the number of free charge carriers available for extraction at the electrodes leading to a reduced short-circuit current, PCE and FF. The strategies for preventing Auger recombination include adequate matching of the energy level of the donor material with the acceptor material. However, semiconductor quantum dots with inherent discrete energy levels could lead to the carrier multiplication of excitons.

2.7 Strategies for enhancing PV metrics of PSCs

Researchers worldwide are tirelessly exploring various approaches to overcome the fundamental challenges of inadequate power conversion efficiency (PCE) and limited shelf life that hinder the commercial viability of polymer solar cells. These strategies include molecular engineering of donor polymer and acceptor materials, device architectural design and interfacial engineering, and doping of a foreign component materials into the functional layers in PSCs.

Molecular engineering of donor and acceptor polymers involves the design, synthesis, and optimisation of existing and new materials for improved performance of PSCs. This includes the new design of chemical structures, sidechain modification, and inter-copolymerisation of monomers of donor materials and acceptor materials for a broader spectrum, tunable bandgaps, efficient charge transport and better phase separation respectively [85, 86, 87, 88, 89, 90]. These approaches led to the improved PV metrics of modified devices. Also, the device's architectural design and interfacial engineering involve the layout and optimisation of interfaces between the

functional layers of PSCs. For instance, the use of inverted architecture designs has proved to be beneficial for the device stability of organic solar cells [91, 92, 93, 94]. Also, Tang *et al* in their review [95] reported that the interfacial engineering and the use of tandem architecture yielded PCEs of over 19% in single-junction [96] and 20% in tandem OSCs respectively. Interfacial engineering also involves the application of solvent additives and solvent annealing in the functional layers of the PSCs.

Additionally, the incorporation of foreign impurities into any of the functional layers of the PSCs has been reported to enhance charge transport in TFPSCs [97, 98, 74, 99, 100, 65, 101]. These have been employed in the various layers of conventional and inverted architectures of organic solar cells, some of them include metallic, bimetallic nanocomposites, plasmonic nanocomposites and semiconductor quantum dot (SQD), which have been found to significantly improve the carriers' dissociation, charge transfer, photon harvesting and reduced energy loss [102, 103, 104, 105, 106, 107]. The main focus of this research is the investigation of the doping impact of SQD in the functional layers of PSCs containing fundamental donor polymers and fullerene-based acceptor materials

2.8 Evolution of semiconductor quantum dots

Semiconductors quantum dots (SQD) were first discovered in a glass matrix in 1981 by Russian scientist Alexey Ekimov at the Vavilov State Institute in St. Petersburg while Louis Brus discovered the colloidal quantum dots when he was working on semiconductors at the AT & T Bell Laboratories in New Jersey 1983. SQD can be described as a unique type of semiconducting material made up of tiny nanocrystals with diameters of 2-10 nm. They can exhibit both photoluminescence and electro-luminescence features. Quantum dots are capable of confining electrons due to the quantum confinement effect when their sizes approach the materials' exciton Bohr radius and glow when stimulated by an external source (for example UV light). Constituents' number of atoms determines the size of quantum dot materials, while the size of quantum dot also determines the colour of light emitted. Quantum dots (QDs) exhibit several notable physical and chemical properties, including a tunable bandgap, large intrinsic dipole moments [108, 109] that often result in rapid charge separation, and the potential to surpass the Shockley-Queisser limit [110] through multiple exciton generation (MEG) [111, 112]. Another feature are high photon absorption rate, which helps minimize non-radiative energy loss [113, 114]. When an incident photon with sufficient energy is absorbed by a QD-based solar cell, bandgap excitation occurs inducing formations of electron-hole bound pair within the ma-

trix of QD, this is followed by diffusion of excitons with electrons infiltrating up to the LUMO while holes remain in the HOMO of the organic matrix, the excitons then dissociated into free charge carriers and eventually travelled to their respective electrodes exhibiting special features like quantum confinement and multiple exciton generation in the process that ultimately lead to the generation of electric current. This phenomenon is further explained in sections **2.8.2 and 2.8.3**.

SQD can be classified into core-type, core-shell and alloy according to their constituent atoms and structure. The concepts of quantum yields, luminescence, and reduced fluorescent quantum efficiency are influenced by both non-radiative and radiative processes, affecting the three different classifications of SQD in various ways. Quantum yield refers to the ratio of emitted photons to the absorbed photons, while the reduced fluorescence quantum yield is a measure of the decrease in the efficiency at which a substance emits fluorescence relative to its maximum capability. On the other hand, luminescence is one of the important traits of SQDs that occurs via the decay of excitons (recombination of charged carriers) via radiative pathways and affects the quantum yields in different types of quantum dots, especially the core-type SQDs. Core SQDs are single-component materials with uniform internal atoms such as chalcogenides of metals (e.g. CdS, ZnS. CdTe, CdSe etc.). The Core-shell QDs can be achieved by growing a small region of a particular material within the shell of another material with a wider bandgap. This method assists in improving the efficiency and fluorescence of semiconductor materials, CdS/ZnS, and CdSe/ZnS are examples of core-shell QDs with CdS and CdSe serving as the core and ZnS being the shell. The shell assists in passivizing the non-radiative locations thereby improving the quantum yields and adapting them to various applications [115, 116, 117, 118]. Alloyed QDs are achieved when the alloy of two semiconductors is used to produce a new one with distinct properties from the parent semiconductors as well as bulk counterparts, examples are CdTeSe, CdSSe/ZnS. The inherent problem that arises because of tuning properties of QDs via modification of their sizes is taken care of with alloyed SQDs. It is possible to tune the properties of SQDs without necessarily changing the crystallite size (especially for some size-restricted applications) except the composition and internal structure of the QDs. For instance, different sizes of CdS_xSe_{1-x}/ZnS QD were synthesised to emit lights of different wavelengths by altering the compositions of the reactants [119]. SQDs are typically synthesized from elements in the II-VI, III-V, and IV-VI groups, as shown in Table 2.1. Quantum size effect and multiple electron generation are crucial attributes of QDs and can be likened to the particle in a well or box.

Table 2.1: Some semiconductors widely used as quantum dots in solar cells.

Semiconductor Material	**Periodic Group**	**Bohr Radius (nm)**	**Bandgap (eV)**
PbS	IV-VI	40.0	0.41
GaAs	III-V	28.0	1.43
CdTe	II-VI	15.0	1.50
CdSe	II-VI	10.6	1.74
ZnSe	II-VI	8.40	2.58
CdS	II-VI	5.60	2.53

2.8.1 Particle in a box

The particle in a well or box is a concept in quantum mechanics that provides a theoretical background to understand some of the features of semiconductor quantum dots. Consider a one-dimensional box in which a particle being sandwiched between two impenetrable barriers is free to move to and forth along a straight line. If the walls of the box are assumed to be regions of space with immensely large potential energy, while the inside of the box has zero potential energy. This indicates that the particle is free to move within the box without any net forces acting on it. The high potential energy at the walls prevents the particle from escaping by repelling it at either boundary. The solution to the time-independent Schrödinger equation (TISE) for a one-dimensional system is used to obtain the energy levels of trapped particle and their wavefunction as shown in equations (2.22) and (2.23) below:

$$\hat{H}\psi(x) = E\psi(x), \tag{2.22}$$

$$-\frac{\hbar^2}{2m}\frac{d^2\psi(x)}{dx^2}+V(x)\psi(x) = E\psi(x), \tag{2.23}$$

where $\hbar$ is the reduced Planck's constant ($\hbar = \frac{h}{2\pi}$), m is the particle's mass, $\psi(x)$ is the time-independent wave function, $V(x)$ is the potential energy, and E is the eigenvalue of the energy. The general solution of the time-independent Schrödinger equation (TISE) is given in equation (2.24):

$$\psi(x) = A\sin(kx)+B\cos(kx), \tag{2.24}$$

where A, B, and k are constants. Upon applying the boundary conditions $\psi(0) = 0$ or $\psi(L) = 0$, the constant k is found to be $\sqrt{\frac{2mE}{\hbar^2}}$, with the wave function $\psi(x) = A\sin\left(\sqrt{\frac{2mE}{\hbar^2}}x\right)$. Applying the boundary conditions again, $\psi(x) = A\sin\left(\frac{n\pi}{L}x\right)$ (where n is a positive integer

$1, 2, 3, \ldots$). The probability of finding the particle inside the box is determined by normalizing the wave function, resulting in the normalisation constant $A = \sqrt{\frac{2}{L}}$. Ultimately, the wavefunction and the allowed energy are given as shown in equations (2.25) and (2.26):

$$\psi_n(x) = \sqrt{\frac{2}{L}} \sin\left(\frac{n\pi}{L}x\right), \tag{2.25}$$

$$E_n = \frac{\hbar^2\pi^2 n^2}{2mL^2} = \frac{h^2 n^2}{8mL^2}, \tag{2.26}$$

where L is the width of the box. If the particle in a box is extended to a three-dimensional sphere such that the boundary condition is $V(r) = 0$ for $0 \leq r \leq R$ and $V(r) = -\infty$ or ∞ elsewhere, where R is the radius of the sphere, the energy level of the spherical particle in equation (2.26) changes to equation (2.27) below.

$$E_n = \frac{h^2 n^2}{8mR^2} = \frac{h^2 n^2}{8m_e^* R^2} + \frac{h^2 n^2}{8m_h^* R^2}. \tag{2.27}$$

where m_e^* and m_h^* are effective masses of electrons and holes respectively. This is because of the interaction with the crystal lattice and is usually expressed in terms of the electron rest mass, m_o. The ground state energy is the minimum energy when $n = 1$ as provided by equation (2.28):

$$E_1 = \frac{h^2}{8m_e^* R^2} + \frac{h^2}{8m_h^* R^2}. \tag{2.28}$$

The approximate Hamiltonian for equation (2.25) and electrostatic interaction between electrons and holes have been resolved by Atkins *et al* [120] using the same boundary condition to obtain confinement and exciton energy which is combined to form the Brus model equation as shown in equation (2.29) below:

$$E_{QD} = E_g^{\text{Bulk}} + \frac{\hbar^2\pi^2}{2R^2}\left(\frac{1}{m_e^*} + \frac{1}{m_h^*}\right) - \frac{1.8e^2}{4\pi\varepsilon_0 R}. \tag{2.29}$$

The solution of a particle in a box as seen from the above equation (2.25) showed that the energy of a particle is quantized as obtainable in semiconductor quantum dots. Also, the minimum or lowest possible energy of a particle is not zero which indicates the particle always has kinetic energy. The evidence above distinguishes bulk semiconductors from those of semiconductor quantum dots. However, the confinement in three dimensions by QD introduces extra effects. These are Coulomb interactions and confinement effects as shown in Luis Brus model equation (2.26) (2nd and 3rd term of equation (2.29)) for semiconductor quantum dots. These exceptional complexities introduce unique dimensions to their optical and electronic properties, making them invaluable for applications in photonics, quantum computing, and optoelectronics. One of the sharp differences between the bulk semiconductor and semiconductor quantum dots is the presence of discrete energy levels that occur via the quantum size effect.

2.8.2 Quantum confinement effect

In bulk semiconductors, when sufficient energy that is equal to or greater than the exciton binding energy is applied, electrons are excited from the valence band to a higher energy level, overcoming the energy bandgap. The resulting vacant position behaves as if it were a positive charge and is referred to as a hole, which remains in the valence band. When the electrons return to their equilibrium and stable state, the excess energy is emitted as light at a specific wavelength. These electron-hole pairs (i.e., excitons, which are hydrogen-like atoms) are weakly bound at about 100 Å (especially at low temperatures). The average distance at which the electron-hole pair is attracted by Coulomb force is called the exciton Bohr radius (a_B). In bulk semiconductors, excitons have ample space to move without confinement. Consequently, the energy levels in these materials create a continuous density of states, where the energy levels are closely spaced and merge to form energy bands. On the contrary, as the size of semiconductor bulk material is reduced, there is a decrease in the number of atoms in the material which can be explained by a property of a material known as Fermi energy (E_F), which represents the energy level of an electron in a system, as given in equation (2.30):

$$E_F = \frac{h^2}{8m}\left(\frac{3N}{\pi V}\right)^{\frac{2}{3}}, \tag{2.30}$$

where m is the mass of the material, h is the plank's constant, and N/V is no of atoms per volume. Since E_F is proportional to the N/V, the decrease in the materials' size will ultimately lead to fewer electrons in the materials. As the number of atoms N decreases due to a reduction in volume, the spacing between energy states widens. The Fermi energy stays constant, this decrease in the number of states results in the formation of discrete energy levels. Quantum confinement occurs when a material's size is reduced to the nanometer scale, comparable to the exciton Bohr radius. When one or more dimensions of a material shrink to this extent, the electronic density of states is altered, indicating the material is confined as indicated in Figure 2.8b. This explains the reason bulk semiconductor material is a 3-dimensional material system, while SQD is a zero-dimensional system in which the motion of the electron is confined in 3-dimension. Similarly, the confinement of electron motion in 1 dimension is referred to as a quantum well, while confinement in 2-dimension is referred to as a quantum wire. The confinements in quantum dots lead to an increase in the separation distance of energy levels such that the spacing between energy levels is greater than K_BT (where k_B is the Boltzmann constant and T is temperature). This leads to the restriction of electrons and hole mobility in the crystal. Subsequently, there is an increase in the energy gap (distance between LUMO and HOMO) such that the spacing between the energy states can

be estimated using $\Delta E = E_F/N$. This distinct feature gives rise to interesting and explorable electronic and optical properties for semiconductor quantum dots in which the QD with the smallest size emits blue light, and the largest size gives off red light. The ranges of sizes between the smallest and largest are responsible for other visible lights. This underscores that the use of SQD with varying sizes can broaden the absorption spectrum range. Hence, the tunability of SQD, makes them suitable for a wide range of applications which includes bioimaging, organic electronics, quantum computing, and photovoltaic technology. The confinement energies of the electron and hole levels can be related to the Bohr radius of the particle (e.g., electron, hole) using equation (2.31):

$$a^*_{\text{exc}} = \left(\frac{\epsilon_r}{\mu}\right) a_B = \epsilon_r \left(\frac{m^*_e + m^*_h}{m^*_e m^*_h}\right) a_B, \tag{2.31}$$

where a^*_{exc} is the Bohr radius of the exciton, ϵ_r is the dielectric constant of the material, a_B is the Bohr radius of the electron (0.53 nm), m^*_e and m^*_h are effective masses of electrons and holes respectively μ is the reduced effective mass of exciton, $\mu = \frac{m^*_e m^*_h}{m^*_e + m^*_h}$ [121]. It is important to state that the energies involved in quantum dots are the energies due to the bandgap of the bulk material, confinement, and excitation. The second term of energy spherical quantum dot stated above in equation (2.29) is confinement energy $\frac{\hbar^2\pi^2}{2R^2}\left(\frac{1}{m^*_e} + \frac{1}{m^*_h}\right)$, which is divided into three regimes namely strong confinement regime, moderate confinement regime and weak confinement regime. The strong confinement regime occurs when the QD radius $R \ll a_h$ and $R \ll a_e$ is achieved, the intermediate confinement regime is when the radius R of the QD satisfies either $R \ll a_h$ or $R \ll a_e$while the weak confinement regime is when the radius R of QD is greater than both the Bohr radius of the electron (a_e) and the hole (a_h). This explains reasons semiconductor QDs are employed in applications like single electron transistors, such as Light emitting diode (LED), optical detectors in optoelectronics, biomedical imaging, optical amplifiers, quantum computing, optical fibres communications, and solar cells [122, 123, 124]. The average diameters can therefore be estimated based on the obtained bandgaps [125]. For instance, Mousa [121] obtained various sizes of lead sulphide QDs by varying the injection temperatures. The results showed that an increase in injection temperature leads to an surge in QD sizes, while their bandgaps reduce. In the same vein, another group [126] used the hydrothermal liquid phase synthesis method to obtain PbS QDs. The group achieved different sizes of QD by varying the concentration of reaction solution and their results showed that the grain size of PbS decreased with the concentrations of the reactants. Moreover, the appearance of discrete energy levels has been associated with a delay in hot carriers' relaxation time. In bulk semiconductors, excited electrons typically emit light, but in semiconductor quantum dots, they instead induce the formation of another electron-hole pair in a phenomenon known

as carrier multiplication or multiple exciton generation (MEG).

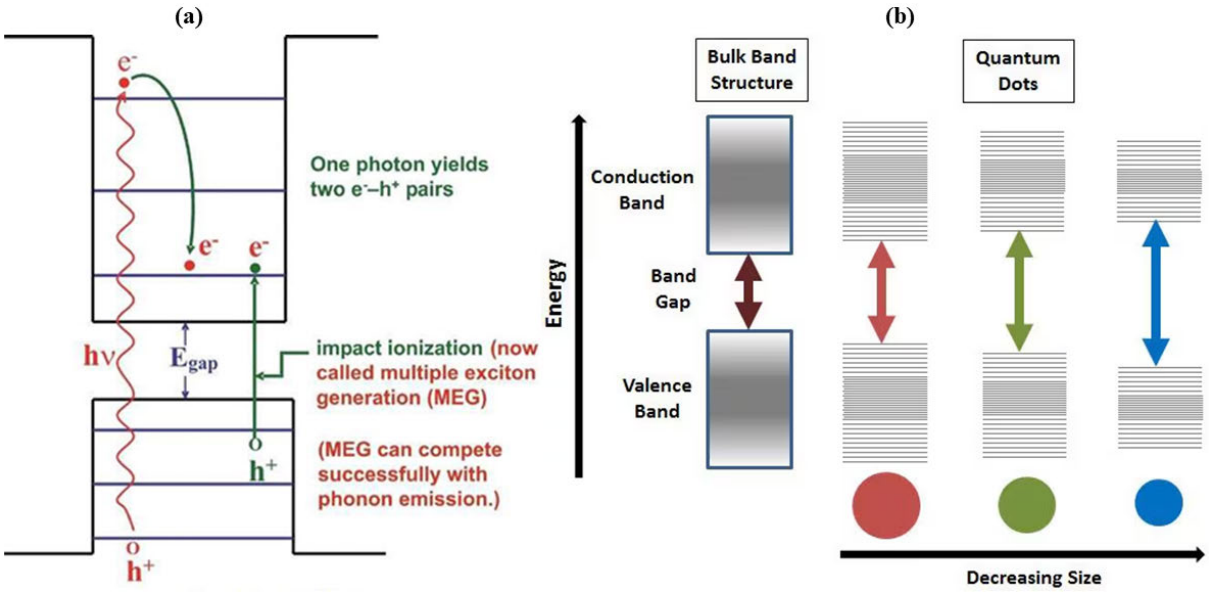

Figure 2.8: (a) Multiple exciton generation of SQD [127] (b) Splitting of energy levels in SQD due to the quantum confinement effect [128].

2.8.3 Multiple exciton generation

Multiple exciton generation (MEG) is a phenomenon in which the absorption of a single photon of energy results in the creation of more than one excitons (see Figure 2.8a). The electron-hole pairs generated are referred to as excitons. This phenomenon is similar to impact ionisation that has been recognized for more than five decades in photo-current of bulk p-n junctions in some bulk semiconductors like silicon, germanium, lead sulphide, lead selenide and indium antimony [129, 130]. However, the impact ionisation in bulk semiconductors is not efficient because a certain threshold of incident energy must be exceeded for impact ionisation to take place. For example, impact ionisation only becomes noticeable in silicon when incident photon energy exceeds 3.5 eV [131] which is almost unrealistic. However, the spatial confinement in quantum dots facilitates the efficient generation of multiple excitons from a single photon. This occurs as a result of excess energy, ΔE_{exc} ($\Delta E_{\text{exc}} \gg E_G$) of absorbed photons used to create additional excitons instead of being dissipated as heat [132]. Despite the advantage of incorporating SQD into the organic solar cells, there is inefficient random hopping among discrete particles. Another shortcoming is the phase separation between inorganic QDs from organic matrix causing an inability to form bicontinuous morphology [133, 134]. This challenge was reportedly addressed by introducing a hybrid nanomaterial consisting of Indium Phosphate (InP) QD/N- doped multi-walled carbon nanotubes (NCNT) in an organic blend

of P3HT/ICBA [135]. The pristine of P3HT/ICBA yielded a power conversion efficiency of 4.68% with fill factor of 58.3%. Also, the addition of InP QD led to a very minimal increase in the open circuit voltage V_{OC} and short circuit current density J_{SC} while the PCE and FF dropped compared to the pristine. Interestingly, there was a significant increase in all the parameters when the hybrid InP/NCNT was introduced to the blend giving a PCE of 6.11%. This showed that synergy between SQD/CNT could promote rapid charge separation, and the transportation of dissociated charges via their high aspect ratio in 1-dimensional nanostructures [136, 137, 138].

2.8.4 Downward and upward conversion phenomena

The tunable bandgap of semiconductor quantum dots plays an important role in these phenomena. Downward conversion photoluminescence (DCPL) is a process in which semiconductor quantum dots absorb high-energy photons and re-emit them at a lower energy (longer wavelength). This phenomenon is beneficial for converting high-energy ultraviolet photons into visible and near-infrared light, thereby enhancing photon absorption. Semiconductor quantum dots with relatively large bandgaps can be utilised in the functional layers of solar devices to improve spectral matching and broaden the photon absorption range. This aligns with Stokes' law of photoluminescence, which states that emitted light typically has lower energy than the absorbed light due to energy losses. The occurrence of DCPL in solar devices leads to improved photovoltaic (PV) performance by providing more useful photons, increasing the short-circuit current density, reducing thermalisation losses, and enhancing spectral matching. The use of quantum dots such as ZnS, CdS, and CdSe in polymer solar cells serves as a viable optimisation strategy. Conversely, upward conversion photoluminescence (UCPL) occurs when two or more low-energy photons are simultaneously absorbed and re-emitted as a single high-energy photon. The occurrence of UCPL is less probable due to the requirement for multi-photon absorption. However, its primary advantage lies in extending light absorption into the infrared region, enabling greater utilization of the solar spectrum.

2.8.5 Shockley-Queisser limit

Shockley-Queisser limit describes the calculation of the maximum theoretical efficiency of a single p-n junction solar cell. It was first calculated by William Shockley and Hans Queisser in 1961 [139]. The theory describes that the maximum current and voltage of the solar cells is dependent on the energy distribution of photons from the sun. The maximum efficiency calculated was about 33.3% for CZGSe semiconductor material with bandgaps ranging from

about 1.36 eV [140, 141]. The solar spectrum contains photons with energies ranging from 0.5 – 3.5 eV. For a photon to be absorbed, it must have an energy that is equal to or greater than the bandgap energy of the material. If the incident photon energy $h\nu$ exceeds the bandgap energy E_G of the material, the photon is absorbed upon interaction with the material, creating hot excitons. The total excess kinetic energy $\Delta E_{\text{exc}} = h\nu - E_G$ that is the difference between photon energy and the bandgap energy. In bulk semiconductors, the kinetic energy is shared between the electrons and holes depending on their effective masses with the carrier with lower effective masses getting more of the excess kinetic energy [131]. The highest loss in the Shockley-Queisser limit is the loss due to excess energy of an absorbed photon that is thermally dissipated via electron-phonon scattering when the carriers return to equilibrium. To increase the efficiency above 31%, there is a need to reduce loss by employing tandem solar cell architecture. The higher energy photons are first absorbed by the higher bandgap semiconductor while the lower energy photons are absorbed by the lower bandgap semiconductor reducing the radiative loss. It is noteworthy that the Shockley-Queisser limit has been used to estimate the PCE of devices that employed QD absorbers capable of exhibiting MEG [131] and the results were compatible with previous calculations [142, 143] on ideal solar cells with a single bandgap that have more than unity quantum yield as a result of impact ionisation. The existence of discrete quantized levels assists in the cooling of photo-generated excitons in SQD semiconductors, thereby controlling the efficiency of exciton multiplication as seen in Figure 2.8a.

2.9 Application of SQD in functional layers of PSCs

Owing to sustained global research, organic solar cells have evolved from single-layer organic materials to bilayer and bulk heterojunction architectures. This progress has increased the power conversion efficiency of fullerene-based organic solar cells to over 14% and non-fullerene-based cells to greater than 19.2%. However, the challenges limiting the currently achieved parameters must be appreciated to proffer ways forward. The fundamental way of achieving better organic solar cells is by focusing on strategies to improve their excitons dissociation, charge separation, and reducing energy losses. These approaches ultimately lead to improved parameters like open-circuit voltage, current density and power conversion efficiency. For instance, the drawback in the use of PCBM in bulk heterojunction (BHJ) includes a high symmetry that is associated with C60-based fullerenes acceptors in polymer-PCBM. This contributes to the inefficient absorption in both visible and NIR regions leading to weak charge generation [142, 143]. Another issue with PCBM is related to the confined possibility of varying its

bandgap owing to a few different chemical structures that can be formed simultaneously with the C60:C70 core being intact [144, 145]. Also, the crystallisation and aggregation of spherical structured PCBM fullerene acceptors reduce the long-term stability of devices [146, 147]. These shortcomings have been overcome with the advent of NFAs. Both fullerene and non-fullerene acceptors have also been utilised to complement each other. The photoactive layers consisting of polymer-fullerene, polymer-polymer, and polymer-non-fullerene acceptors have been employed to generate considerable power conversion efficiencies over the years.

Ongoing efforts to optimise various parameters to position organic solar cells at the forefront of commercial OPV production. The applications of quantum dots in organic solar systems have recently gained momentum in polymer solar cells and other emerging solar technologies. This involves the use of semiconductor QD in the functional layers or interlayers of the PSC. Another way involves the use of QD together with other materials like carbon nanotubes in other to assist transportation of free carriers to the electrodes.

Lee *et al* [135] reported the synthesis and fabrication of indium phosphide quantum dots (QDs) and N-doped carbon nanotubes (CNTs) synthesised by pyrolysis and employed in the active layer of poly(3-hexylthiophene) (P3HT):ICBA (indene-C60 bisadduct), achieving a power conversion efficiency (PCE) of 6.11% compared to the pristine device, which gives 4.68% using conventional architecture ITO/PEDOT:PSS/P3HT:ICBA/QD:NCNT/WO3/Al. The use of core CdSe and core-shell CdSe@ZnS QDs as an interlayer between the electron transport layer (ETL) polyethylenimine ethoxylated (PEIE) polymer and the active blend of PTB7-Th:$PC_{71}BM$ was explored by Park *et al* [148] achieving optimal performance with core CdSe QD via interfacial engineering of inverted polymer solar cells (iPSCs).

Savva *et al* doped carbon quantum dots (CQDs) into the polyethylenimine ethoxylated (PEIE) electron transport layer to improve the charge transport characteristics. The CQD-doped PEIE layer was sandwiched between an indium tin oxide (ITO) electrode and an active layer consisting of PTB7-Th:PC71BM. By varying the concentrations of CQDs, the optimal photovoltaic metrics were achieved: a power conversion efficiency (PCE) of 9.468% compared to 8.549%, an open-circuit voltage (V_{oc}) of 0.781 V compared to 0.783 V, a short-circuit current density (J_{sc}) of 17.751 $mAcm^{-2}$ versus 16.824 $mAcm^{-2}$, and a fill factor (FF) of 0.683 compared to 0.649 [149]. This improvement in charge transport characteristics led to a decrease in the rate of charge recombination due to reduced charge accumulation at the interface. The inherent multiple exciton generation feature of quantum dots (QDs) was effectively explored. Similarly, the

inadequacies of hybrid ternary blends of surface-modified quantum dots (SQDs) due to charge carrier loss resulting from SQDs acting as recombination points as well as clustering and aggregation of QDs in the organic matrix were addressed by Nam *et al* [150]. This was achieved by inserting a PbS quantum dot layer between the organic blend and the top electrode as a separate layer. The architecture (ITO-glass/PEIE/organic BHJ layer/PbS QD/MoO3/Ag) led to the attainment of a power conversion efficiency (PCE) of 10.12% compared to 8.84% for the device without the PbS QD layer.

Table 2.2: Fullerene-based PSCs with semiconductor quantum dots in the buffer layer.

Device Structure	**V_{oc} (V)**	**J_{sc} (mA/cm^2)**	**FF (%)**	**PCE (%)**	**R_S A (Ωcm^2)**	**R_{SH} A (kΩcm^2)**	**Ref.**	**Year**
Conventional architecture								
Glass/ITO/PEDOT:PSS/PTB7 :$PC_{71}BM$/MoO_3/Ag	0.72	18.10	57.0	7.24	-	-	[152]	2021
GlassITO/PEDOT:PSS:MoS_2 QD/PTB7:$PC_{71}BM$ /MoO_3/Ag	0.74	19.40	60.0	8.32	-	-	”	
Glass/ITO/PEDOT:PSS/PTB7 -Th:$PC_{71}BM$ /MoO_3/Ag	0.82	19.10	62.0	9.49	-	-	[152]	2021
Glass/ITO/PEDOT:PSS:MoS_2 /PTB7-Th:$PC_{71}BM$ /MoO_3/Ag	0.81	20.30	66.0	10.57	-	-	”	
Glass/ITO/PEDOT:PSS:/P3HT :PCBM/LiF/Al	0.55	9.37	49.72	2.30	10.48	0.218	[74]	2022
Glass/ITO/PEDOT:PSS/CdTeSe :/P3HT:PCBM/LiF/Al	0.55	14.65	61.21	4.87	8.24	0.680	”	
Glass/ITO/PEDOT:PSS:CdTeSe /P3HT:PCBM/LiF/Al	0.55	8.50	54.01	2.55	3.70	-	[101]	2023
Glass/ITO/PEDOT:PSS:CdTeSe /P3HT:PCBM:3% CdTeSe QD +CN/LiF/Al	0.58	16.87	53.19	5.18	2.92	-	”	
Inverted architecture								
Glass/ITO/PEIE/PTB7-Th: $PC_{71}BM$/MoO_3/Al	0.72	14.13	69.90	7.17	5.47	1.53	[148]	2020
Glass/ITO/PEIE/CdSe@ZnS/ PTB7-Th:$PC_{71}BM$/MoO_3/Al	0.70	14.80	70.31	7.31	5.47	1.87	”	
Glass/ITO/PEIE/CdSe/ PTB7-Th:$PC_{71}BM$/MoO_3/Al	0.74	15.39	71.00	8.13	4.61	3.51	”	
Glass/ITO/PEIE/PTB7-Th: $PC_{71}BM$/MoO_3/Al	0.783	16.82	64.9	8.549	5.68	-	[149]	2021
Glass/ITO/PEIE/CQD/ PTB7-Th:$PC_{71}BM$/MoO_3/Al	0.781	17.75	68.3	9.468	3.61	-	”	
Glass/ITO/PEDOT:PSS/PbS/ PTB7-Th:$PC_{70}BM$ /Al	0.78	17.12	65.0	8.84	-	-	[150]	2021
Glass/ITO/PEIE/PTB7-Th: $PC_{70}BM$/PbS/MoO_3/Ag	0.78	19.43	67.0	10.12	-	-	”	
Glass/ITO/ZnO/PTB7-Th: $PC_{71}BM$/MoO_3/Al	0.69	15.67	53.63	5.78	8.16	246	[154]	2024
Glass/ITO/ZnO:CdS/ZnS/ PTB7-Th:$PC_{71}BM$/MoO_3/Al	0.67	19.50	56.24	7.13	6.42	247	”	

Table 2.3: Fullerene-based PSCs with semiconductor quantum dots in the active layer.

Device Structure	$\mathbf{V_{oc}}$ (V)	$\mathbf{J_{sc}}$ (mA/cm^2)	**FF** (%)	**PCE** (%)	$\mathbf{R_S A}$ (Ω cm^2)	$\mathbf{R_{SH} A}$ (kΩ cm^2)	**Ref.**	**Year**
Inverted architecture								
Glass/ITO/ZnO/PTB7-Th:$PC_{71}BM$ /MoO_3/Ag	0.788	16.56	65.7	8.58	-	-	[151]	2021
Glass/ITO/ZnO/PTB7-Th:$PC_{71}BM$ /5% wt.CdSe QD/MoO_3/Ag	0.804	18.76	63.4	9.57	-	-	”	
Conventional architecture								
ITO/PEDOT:PSS/PTB7-Th:$PC_{71}BM$ /PDINO/Ag	0.79	16.42	68.35	8.87	4.38	0.805	[70]	2022
ITO/PEDOT:PSS/PTB7-Th:$PC_{71}BM$:CdSe/PDINO/Ag	0.81	17.31	69.56	9.77	4.07	0.907	”	
GLASS/ITO/PEDOT:PSS/P3HT :PCBM/LiF/Al	0.55	8.45	54.95	2.55	5.52	-	[153]	2023
GLASS/ITO/PEDOT:PSS/P3HT :PCBM:3% CdTeSe QD+CN/LiF/Al	0.58	14.81	58.72	5.07	4.44	-	”	
GLASS/ITO/PEDOT:PSS:CdTeSe /P3HT:PCBM/LiF/Al	0.55	8.50	54.01	2.55	3.70	-	[101]	2023
GLASS/ITO/PEDOT:PSS:CdTeSe/ P3HT:PCBM:3%CdTeSeQD+CN/LiF/Al	0.58	16.87	53.19	5.18	2.92	-	”	

Yang *et al* [151] also employed cadmium selenide quantum dots (QDs) as the third component in the photoactive layer consisting of PTB7-Th:PC71BM, which improved the power conversion efficiency (PCE) and short-circuit current density (J_{SC}) by 13% and 11%, respectively. The issue of device stability when using ethylene diamine tetraacetic acid (EDT) and molybdenum trioxide (MoO_3) as the interfacial layer was addressed by Becker-Koch *et al* [71]. It was demonstrated that an organic solar cell based on poly[bis(4-phenyl)(2,4,6-trimethylphenyl)amine] (PTAA) polymer doped with $C_{60}F_{48}$ is a more efficient hole extraction layer compared to EDT and MoO_3, achieving a maximum PCE of 10.41% compared to 8.16% with EDT and 9.08% with PTAA/MoO_3. The improved photovoltaic performance of the device is attributed to the fast extraction of holes enabled by the high conductivity of doped PTAA:$C_{60}F_{48}$ layers and the high blocking ability of PTAA due to its low electron affinity. The effect of the size of MoS_2 quantum dots employed in donor-acceptor active layers of PTB7:$PC_{71}BM$ and PTB7-Th:$PC_{71}BM$ was reported by [152]. The 5 and 10 nanometer thickness layers of MoS_2 QDs were deposited on PEDOT:PSS/ITO as the hole transport layer. The modified HTL devices produced better PV metrics. The device with a 5 nm MoS_2 layer gave optimal performance compared with the 10 nm MoS_2 with PCE of (8.32%

vs. 7.80%), (V_{OC}) of (0.74 V vs. 0.73 V), (J_{SC}) of (19.40 mA cm^{-2} vs.19.20 mAcm^{-2}. This result is in perfect agreement with the size tunability of QDs highlighted in Table 2.1 above. The experiment also showed that optimisation of donor polymer or active layer with the incorporation of QD as a separate layer on the ITO/PEDOT:PSS provided better photovoltaic performance. Likewise, the use of CdSe QD with different PL emissions (462, 525, 623 nm) incorporated into PTB7:$PC_{71}BM$ BHJ active layers were demonstrated by Zicha *et al* [70] with improved PV metrics by all the modified active layers compared to a pristine device without CdSe QD. The device with 623 nm CdSe QD produced the best performance traceable to its photon harvesting in the ultraviolet region. The exemplary nature of typical alloy QD was demonstrated by Mola *et al* [74] by incorporating CdTeSe QD dispersed in ethylene glycol in HTL of PEDOT:PSS in the conventional fabrication of thin film organic solar cell comprising P3HT:PCBM to achieve improved PV parameters indicated in Table 2.2. The same group also demonstrated the simultaneous use of alloy QD in the buffer and active layers of TFOSCs [153, 101] resulting in better PV parameters (see Table 2.3). Another group [70] recently reported doping of a 3% concentration of Cadmium selenide (CdSe) QD at different photoluminescence (PL) emission wavelengths into the photoactive layer. The optimum performance parameter was achieved at PL with a wavelength of 623 nm (V_{OC} – 0.81 V; J_{sc} – 17.31 mA/cm^2, FF – 69.56%; PCE – 9.77%). The series resistance was found to increase with PL wavelengths which is like what was obtainable in the work reported by Amole *et al*. The incorporation of core-shell $Cd_xS/Zn_{1-x}S$ QD in the electron transport layer of organic solar cell in inverted architecture was recently found to be beneficial for PCE enhancement in ambient environmental conditions [154].

Table 2.4: NFA-based PSCs with semiconductor quantum dots in the buffer/inter layer.

Device Structure	$\mathbf{V_{oc}}$ (V)	$\mathbf{J_{sc}}$ (mA/cm^2)	**FF** (%)	**PCE** (%)	$\mathbf{R_SA}$ (Ω cm^2)	$\mathbf{R_{SH}A}$ (kΩ cm^2)	**Ref.**	**Year**
Conventional architecture								
ITO/PEDOT:PSS/PM6:Y6 /PFN-Br/Al	0.827	23.56	71.03	13.78	2.89	0.318	[155]	2021
ITO/PEDOT:PSS/PM6:Y6/ PFN-Br/1% BPQD/Al 3000 rpm	0.834	25.46	74.44	15.20	2.71	1.97	”	
Device Structure	$\mathbf{V_{oc}}$ (V)	$\mathbf{J_{sc}}$ (mA/cm^2)	**FF** (%)	**PCE** (%)	$\mu_h\times10^{-4}$ (cm^2 V^{-1} s^{-1})	$\mu_e\times10^{-4}$ (cm^2 V^{-1} s^{-1})	**Ref.**	**Year**
ITO/PEDOT:PSS/PM6:Y6 /MoO_3/Al	0.85	25.80	71.25	15.63	6.7	2.1	[32]	2022
ITO/CdSe@ZnS/PEDOT:PSS /PM6:Y6/MoO_3/Al	0.84	25.54	71.67	15.47	6.0	1.2	”	
ITO/PEDOT:PSS/PM6:Y6 /MoO_3/Al+UV1000 min	0.82	15.75	59.14	7.64	4.9	2.1	[32]	2022
ITO/CdSe@ZnS/PEDOT:PSS/ PM6:Y6/MoO_3/Al + UV 1000 min	0.77	21.64	61.44	10.24	6.4	1.2	”	
ITO/PEDOT:PSS/PBDB-T :ITIC/MoO_3/Al	0.88	16.18	67.49	9.61	-	-	[32]	2022
ITO/CdSe@ZnS/PEDOT:PSS/ PBDB-T:ITIC/MoO_3/Al	0.88	15.89	67.00	9.37	-	-	”	
ITO/PEDOT:PSS/PBDB-T:ITIC /MoO_3/Al+UV 1000 min	0.84	12.52	51.30	5.40	-	-	[32]	2022
ITO/CdSe@ZnS/PEDOT:PSS/ PBDB-T:ITIC/MoO_3/Al+UV1000 min	0.81	14.28	56.96	6.59	-	-	”	
Glass/ITO/PEDOT:PSS/D18:Y6 /PDINN/Ag	0.86	27.47	70.10	16.63	1.24	-	[156]	2023
Glass/ITO/PEDOT:PSS+0.5% $PdSe_2$ /D18:Y6/PDINNO/Ag	0.86	28.53	74.22	18.12	1.70	-	”	
Glass/ITO/PEDOT:PSS/PM6:L8-BO/ PDINN/Ag	0.88	25.62	72.92	17.11	3.21	-	[156]	2023
Glass/ITO/PEDOT:PSS+$PdSe_2$/ PM6:L8-BO/PDINN/Ag	0.88	26.31	76.99	18.29	4.13	-	”	
Glass/ITO/PEDOT:PSS /PBDB-T:ITIC/PFN-Br/Al	0.89	15.16	69.14	9.31	1.99	-	[31]	2024
Glass/ITO/$MoSe_2$/PBDB-T :ITIC/PFN-Br/Al	0.89	15.29	68.39	9.34	3.29	-	”	
Glass/ITO/PEDOT :PSS/PM6:Y6/PFN-Br/Al	0.83	25.76	72.37	15.51	1.99	-	[31]	2024
Glass/ITO/$MoSe_2$/PM6 :Y6/PFN-Br/Al	0.83	26.45	70.04	15.36	3.29	-	”	
Glass/ITO/PEDOT:PSS/ PM6:L8-BO/PFN-Br/Al	0.89	26.33	78.70	18.22	1.99	-	[31]	2024
Glass/ITO/$MoSe_2$/PM6: L8-BO/PFN-Br/Al	0.89	26.34	77.88	18.29	3.29	-	”	

The utilisation of some selected polymer donors and non-fullerene acceptors was reported [32]

with cadmium selenide doped with zinc sulphide QD (CdSe@ZnS). The QDs were used as hole extraction layers in conventional architecture with and without CdSe@ZnS QD as an interlayer between the PEDOT:PSS and the active layer. The results revealed that devices with a modified PEDOT:PSS hole extraction layer (HEL) degraded more slowly compared to the pristine devices after exposure to UV light for 1000 minutes. The durability of the modified HEL devices was found to be greater; however, their power conversion efficiencies (PCEs) and other performance parameters were similar to those of the pristine devices before UV exposure (see Table 2.4). The modification with quantum dots (QDs) proved to be significant for the stability of the devices. Palladium diselenide ($PdSe_2$), a group 10 transition metal chalcogenide, demonstrated great potential in the optoelectronic field upon its incorporation into PEDOT:PSS, yielding better PCE values for different photoactive layers [156]. Lately, the potential use of semiconductor QDs as hole transport materials was explored and reported by Dou *et al* [31]. They investigated the use of 2-dimensional $MoSe_2$ QDs as a hole transport layer (HTL) instead of the popular and traditional HTL, PEDOT:PSS. The experiment was performed using three different non-fullerene-based photoactive layers: PBDB-T:3,9-bis(2-methylene(3-(1,1-dicyanomethylene)-indanone))-5,5,11,11-tetrakis(4-hexylphenyl)dithieno-[2,3-d:2,3-d]-s-indaceno[1,2-b:5,6-b]dithiophene (ITIC) and PM6:Y6, and PM6:L8-BO. The results showed better stability for all three photoactive layers and improved PCEs for both PBDB-T:ITIC and PM6:L8-BO, as detailed in Table 2.4.

2.10 Group II-VI semiconductors

Group II-VI semiconductors are among the most extensively studied and explored semiconductors. They are composed of at least one electropositive element from Group II and one chalcogen element from Group 16 of the periodic table, which includes oxygen (O), sulfur (S), selenium (Se), tellurium (Te), and polonium (Po). These materials can exist as binary, ternary, or quaternary compounds and exhibit a broad range of electronic energy bandgaps. Their direct energy bands traverse the entire light spectrum, from ultraviolet to near-infrared regions [157]. Due to their outstanding thermal, electronic, and optical properties, these materials are invaluable in various fields, including organic and optoelectronic technologies, energy storage, and energy conversion technologies. This is largely due to their controlled, facile, and environmentally friendly synthesis methods, as well as their versatility and high quantum yields [158, 159, 160]. The semiconductor quantum dots of II-VI can be achieved once their size ranges between 1 to 10 nm. Their SQD is divided into core, core-shell and alloy SQD. The group

II-VI core SQD (e.g. CdTe, CdSe, ZnTe, and ZnS) and core-shell (CdSe/ZnS. CdTe/ZnS, CdS/ZnS) have been reported to exhibit high absorption coefficients with excellent tunable bandgap energy [157, 161] which underscore their suitability in solar cell fabrication. The alloy SQQ like CdTeSe, CdSeS, CdZnTe, and HgCdTe displayed distinct characteristics from their constituent elements and have proved to be useful in photodetector gadgets, bio-imaging investigation, sensor devices and PV technologies [162].

Hence, the group II-VI SQD's unique features have made them choice materials for emerging solar cell technologies and energy storage applications. They have great potential to overcome the current PCE limits, reduce production costs, stabilise evolving hybrid-solar technologies and facilitate rapid energy transition from fossil fuels.

References

[1] Heeger, A. Semiconducting and metallic polymers: The fourth generation of polymeric materials. (ACS Publications,2001)

[2] MacDiarmid, A. A novel role for organic polymers. Rev. Mod. Phys. **73** pp. 701 (2001)

[3] Shirakawa, H. Nobel prize in chemistry 2000 electrically conductive plastic the discovery of polyacetylene film: The dawning of an era, Angew. Chem. Int. Ed. **40**, 2574-2580 (2001)

[4] Goyal, M., Singh, K. & Bhatnagar, N. Conductive polymers: A multipurpose material for protecting coating. Progress In Organic Coatings. **187** pp. 108083 (2024)

[5] Chiang, C., Druy, M., Gau, S., Heeger, A., Louis, E., MacDiarmid, A., Park, Y. & Shirakawa, H. Synthesis of highly conducting films of derivatives of polyacetylene,(ch) x. Journal Of The American Chemical Society. **100**, 1013-1015 (1978)

[6] Skotheim, T. Handbook of conducting polymers. (CRC press,1997)

[7] Bakhshi, A. & Bhalla, G. Electrically conducting polymers: Materials of the twentyfirst century. (2004)

[8] Poddar, A., Patel, S. & Patel, H. Synthesis, characterisation and applications of conductive polymers: A brief review. Polymers For Advanced Technologies. **32**, 4616-4641 (2021)

[9] Zare, Y. & Rhee, K. Calculation of the electrical conductivity of polymer nanocomposites assuming the interphase layer surrounding carbon nanotubes. Polymers. **12**, 404 (2020)

[10] Inal, S., Rivnay, J., Suiu, A., Malliaras, G. & McCulloch, I. Conjugated polymers in bioelectronics. Accounts of Chemical Research. **51**, 1368-1376 (2018)

[11] Yu, X., Chen, L., Li, C., Gao, C., Xue, X., Zhang, X., Zhang, G. & Zhang, D. Intrinsically stretchable polymer semiconductors with good ductility and high charge mobility through reducing the central symmetry of the conjugated backbone units. Advanced Materials. **35**, 2209896 (2023)

[12] Kaur, G., Adhikari, R., Cass, P., Bown, M. & Gunatillake, P. Electrically conductive polymers and composites for biomedical applications. RSC Advances. **5**, 37553-37567 (2015)

[13] Abshirini, M., Marashizadeh, P., Saha, M., Altan, M. & Liu, Y. Three-dimensional printed highly porous and flexible conductive polymer nanocomposites with dual-scale porosity and piezoresistive sensing functions. ACS Applied Materials & Interfaces. **15**, 14810-14825 (2023)

[14] Ibanez, J., Rincón, M., Gutierrez-Granados, S., Chahma, M., Jaramillo-Quintero, O. & Frontana-Uribe, B. Conducting polymers in the fields of energy, environmental remediation, and chemical–chiral sensors. Chemical Reviews. **118**, 4731-4816 (2018)

[15] Shahabuddin, S., Mazlan, N., Baharin, S. & Sambasevam, K. Introduction to conducting polymers, Advances in hybrid conducting polymer technology. (2021)

[16] Kausar, A. Overview on conducting polymer in energy storage and energy conversion system. Journal of Macromolecular Science, Part A. **54**, 640-653 (2017)

[17] Tadesse, M., Ahmmed, A. & Lübben, J. Review on conductive polymer composites for supercapacitor applications. Journal Of Composites Science. **8**, 53 (2024)

[18] Hou, W., Xiao, Y., Han, G. & Lin, J. The applications of polymers in solar cells: A review. Polymers. **11**, 143 (2019)

[19] Murad, A., Iraqi, A., Aziz, S., Abdullah, S. & Brza, M. Conducting polymers for optoelectronic devices and organic solar cells: A review. Polymers. **12**, 2627 (2020)

[20] Wu, P., Xu, Y., Zhan, J., Li, Y., Xue, H. & Pang, H. The research development of quantum dots in electrochemical energy storage. Small. **14**, 1801479 (2018)

[21] Xu, Q., Niu, Y., Li, J., Yang, Z., Gao, J., Ding, L., Ni, H., Zhu, P., Liu, Y. & Tang, Y. Recent progress of quantum dots for energy storage applications. Carbon Neutrality. **1**, 13 (2022)

[22] Le, T., Kim, Y. & Yoon, H. Electrical and electrochemical properties of conducting polymers. Polymers. **9**, 150 (2017)

[23] Kang, H., Lee, W., Oh, J., Kim, T., Lee, C. & Kim, B. From fullerene–polymer to all-polymer solar cells: The importance of molecular packing, orientation, and morphology control. Accounts of Chemical Research. **49**, 2424-2434 (2016)

[24] Saleem, R., Farhat, A., Khera, R., Langer, P. & Iqbal, J. Designing of small molecule non-fullerene acceptors with cyanobenzene core for photovoltaic application. Computational and Theoretical Chemistry. **1197** pp. 113154 (2021)

[25] Yin, H., Yan, J., Ho, J., Liu, D., Bi, P., Ho, C., Hao, X., Hou, J., Li, G. & So, S. Observing electron transport and percolation in selected bulk heterojunctions bearing fullerene derivatives, non-fullerene small molecules, and polymeric acceptors. Nano Energy. **64** pp. 103950 (2019)

[26] Hamada, F. & Saeki, A. Mobility relaxation of holes and electrons in polymer: Fullerene and polymer: Non-fullerene acceptor solar cells. ChemSusChem. **14**, 3528-3534 (2021)

[27] Li, D., Sun, C., Yan, T., Yuan, J. & Zou, Y. Asymmetric non-fullerene small-molecule acceptors toward high-performance organic solar cells. ACS Central Science. **7**, 1787-1797 (2021)

[28] Zhu, L., Zhang, M., Zhong, W., Leng, S., Zhou, G., Zou, Y., Su, X., Ding, H., Gu, P. & Liu, F. Progress and prospects of the morphology of non-fullerene acceptor based high-efficiency organic solar cells. Energy & Environmental Science. **14**, 4341-4357 (2021)

[29] Ma, L., Zhang, S. & Hou, J. Crystal structures in state-of-the-art non-fullerene electron acceptors. Journal of Materials Chemistry A. **11**, 481-494 (2023)

[30] Zhu, C., An, K., Zhong, W., Li, Z., Qian, Y., Su, X. & Ying, L. Design and synthesis of non-fullerene acceptors based on a quinoxalineimide moiety as the central building block for organic solar cells. Chemical Communications. **56**, 4700-4703 (2020)

[31] Dou, Z., Cheng, X., Qin, Z., Wang, K., Xia, W., Qu, Y., Lian, H., Yan, F. & Dong, Q. Solution-processable two-dimensional mose2 quantum dots as a hole transport layer for highly efficient and stable nonfullerene organic solar cells. Solar RRL. **8**, 2300693 (2024)

[32] Lan, W., Gu, J., Gao, X., Gong, C., Liu, Y., Zhang, W., Sun, Y., Yue, T., Wei, B. &

Zhu, F. Efficient and ultraviolet-durable nonfullerene organic solar cells: From interfacial passivation and microstructural modification perspectives. Advanced Materials Interfaces. **9**, 2101894 (2022)

[33] Wali, L., Dheyab, A. & Alwan, A. Study the influence of shell thickness in bimetallic Ag core & Au shell configurations integrated in bare si pn junction solar cells. Materials Science and Engineering: B. **288** pp. 116210 (2023)

[34] Wei, R., Tang, N., Jiang, L., Yang, J., Guo, J., Yuan, X., Liang, J., Zhu, Y., Wu, Z. & Li, H. Bimetallic nanoparticles meet polymeric carbon nitride: Fabrications, catalytic applications and perspectives. Coordination Chemistry Reviews. **462** pp. 214500 (2022)

[35] Omrani, M., Fallah, H., Choy, K. & Abdi-Jalebi, M. Impact of hybrid plasmonic nanoparticles on the charge carrier mobility of p3ht: Pcbm polymer solar cells. Scientific Reports. **11**, 19774 (2021)

[36] Li, Z., Fu, J., Zhou, X., Gui, S., Wei, L., Yang, H., Li, H. & Guo, X. Ionic conduction in polymer-based solid electrolytes. Advanced Science. **10**, 2201718 (2023)

[37] Guo, Y., Ruan, K., Shi, X., Yang, X. & Gu, J. Factors affecting thermal conductivities of the polymers and polymer composites: A review. Composites Science and Technology. **193** pp. 108134 (2020)

[38] Xu, Y., Wang, X. & Hao, Q. A mini review on thermally conductive polymers and polymer-based composites. Composites Communications. **24** pp. 100617 (2021)

[39] Gochnauer, D. & Gilani, T. Conduction mechanism in electrically conducting polymers. American Journal of Undergraduate Research. **14** (2018)

[40] Rahaman, M., Aldalbahi, A., Govindasami, P., Khanam, N., Bhandari, S., Feng, P. & Altalhi, T. A new insight in determining the percolation threshold of electrical conductivity for extrinsically conducting polymer composites through different sigmoidal models. Polymers. **9**, 527 (2017)

[41] Brigandi, P. Electrically conductive multiphase polymer blend carbon-based composites. (Lehigh University,2017)

[42] Liu, Q., Jiang, Y., Jin, K., Qin, J., Xu, J., Li, W., Xiong, J., Liu, J., Xiao, Z. & Sun, K. 18% efficiency organic solar cells. Science Bulletin. **65**, 272-275 (2020)

[43] Mihailetchi, V., Xie, H., Boer, B., Koster, L. & Blom, P. Charge transport and photocurrent generation in poly (3-hexylthiophene): Methanofullerene bulk-heterojunction solar cells. Advanced Functional Materials. **16**, 699-708 (2006)

[44] Li, G., Shrotriya, V., Huang, J., Yao, Y., Moriarty, T., Emery, K. & Yang, Y. High-efficiency solution processable polymer photovoltaic cells by self-organisation of polymer blends. Nature Materials. **4**, 864-868 (2005)

[45] Sariciftci, N., Smilowitz, L., Heeger, A. & Wudl, F. Photoinduced electron transfer from a conducting polymer to buckminsterfullerene. Science. **258**, 1474-1476 (1992)

[46] Yu, G., Gao, J., Hummelen, J., Wudl, F. & Heeger, A. Polymer photovoltaic cells: Enhanced efficiencies via a network of internal donor-acceptor heterojunctions. Science. **270**, 1789-1791 (1995)

[47] Lu, H., Liu, W., Ran, G., Liang, Z., Li, H., Wei, N., Wu, H., Ma, Z., Liu, Y. & Zhang, W. High-pressure fabrication of binary organic solar cells with high molecular weight d18 yields record 19.65% efficiency. Angewandte Chemie. **135**, 202314420 (2023)

[48] Chen, Z., Zhu, J., Yang, D., Song, W., Shi, J., Ge, J., Guo, Y., Tong, X., Chen, F. & Ge, Z. Isomerisation strategy on a non-fullerene guest acceptor for stable organic solar cells with over 19% efficiency. Energy & Environmental Science. **16**, 3119-3127 (2023)

[49] Fan, Q., Ma, R., Bi, Z., Liao, X., Wu, B., Zhang, S., Su, W., Fang, J., Zhao, C. & Yan, C. 19.28% efficiency and stable polymer solar cells enabled by introducing an nir-absorbing guest acceptor. Advanced Functional Materials. **33**, 2211385 (2023)

[50] Guo, C., Fu, Y., Li, D., Wang, L., Zhou, B., Chen, C., Zhou, J., Sun, Y., Gan, Z. & Liu, D. A polycrystalline polymer donor as pre-aggregate toward ordered molecular aggregation for 19.3% efficiency binary organic solar cells. Advanced Materials. **35**, 2304921 (2023)

[51] Han, C., Wang, J., Zhang, S., Chen, L., Bi, F., Wang, J., Yang, C., Wang, P., Li, Y. & Bao, X. Over 19% efficiency organic solar cells by regulating multidimensional intermolecular

interactions. Advanced Materials. **35**, 2208986 (2023)

[52] Ballif, C., Haug, F., Boccard, M., Verlinden, P. & Hahn, G. Status and perspectives of crystalline silicon photovoltaics in research and industry. Nature Reviews Materials. **7**, 597-616 (2022)

[53] Heath, G., Silverman, T., Kempe, M., Deceglie, M., Ravikumar, D., Remo, T., Cui, H., Sinha, P., Libby, C. & Shaw, S. Research and development priorities for silicon photovoltaic module recycling to support a circular economy. Nature Energy. **5**, 502-510 (2020)

[54] Liu, F., Zeng, Q., Li, J., Hao, X., Ho-Baillie, A., Tang, J. & Green, M. Emerging inorganic compound thin film photovoltaic materials: Progress, challenges and strategies. Materials Today. **41** pp. 120-142 (2020)

[55] Luceño-Sánchez, J., Díez-Pascual, A. & Capilla, R. Materials for photovoltaics: State of art and recent developments. International Journal Of Molecular Sciences. **20**, 976 (2019)

[56] Chamberlain, G. Organic solar cells: A review, Solar cells 8. (1983)

[57] Yuan, J., Zhang, C., Qiu, B., Liu, W., So, S., Mainville, M., Leclerc, M., Shoaee, S., Neher, D. & Zou, Y. Effects of energetic disorder in bulk heterojunction organic solar cells. Energy & Environmental Science. **15**, 2806-2818 (2022)

[58] Li, D., Deng, N., Fu, Y., Guo, C., Zhou, B., Wang, L., Zhou, J., Liu, D., Li, W. & Wang, K. Fibrillisation of non-fullerene acceptors enables 19% efficiency pseudo-bulk heterojunction organic solar cells. Advanced Materials. **35**, 2208211 (2023)

[59] Xu, X., Jing, W., Meng, H., Guo, Y., Yu, L., Li, R. & Peng, Q. Sequential deposition of multicomponent bulk heterojunctions increases efficiency of organic solar cells. Advanced Materials. **35**, 2208997 (2023)

[60] Gao, W., Qi, F., Peng, Z., Lin, F., Jiang, K., Zhong, C., Kaminsky, W., Guan, Z., Lee, C. & Marks, T. Achieving 19% power conversion efficiency in planar-mixed heterojunction organic solar cells using a pseudosymmetric electron acceptor. Advanced Materials. **34**, 2202089 (2022)

[61] Deibel, C. & Dyakonov, V. Polymer–fullerene bulk heterojunction solar cells. Reports on Progress in Physics. **73**, 096401 (2010)

[62] Deibel, C., Strobel, T. & Dyakonov, V. Role of the charge transfer state in organic donor–acceptor solar cells. Advanced Materials. **22**, 4097-4111 (2010)

[63] Clarke, T. & Durrant, J. Charge photogeneration in organic solar cells. Chemical Reviews. **110**, 6736-6767 (2010)

[64] Wehenkel, D. Physical processes in organic solar cells. (2012)

[65] Ashagre, S., Ogundele, A., Ike, J., Gebremichael, B., Bekele, M., Sharma, G. & Mola, G. Synergistic contribution of potassium sulfide doped with silver nanoparticles on the performance of thin film organic solar cells. Journal of Physics and Chemistry of Solids. **177** pp. 111290 (2023)

[66] Hamed, M. & Mola, G. Copper sulphide as a mechanism to improve energy harvesting in thin film solar cells. Journal of Alloys And Compounds. **802** pp. 252-258 (2019)

[67] Bi, P., Wang, J., Cui, Y., Zhang, J., Zhang, T., Chen, Z., Qiao, J., Dai, J., Zhang, S. & Hao, X. Enhancing photon utilisation efficiency for high-performance organic photovoltaic cells via regulating phase-transition kinetics. Advanced Materials. **35**, 2210865 (2023)

[68] Li, J., Zhang, C., Sun, X., Wang, H., Hu, H., Wang, K. & Xiao, M. Small molecule donor third component incorporating thieno [3, 2-b] thiophene unit enables 19.18% efficiency ternary organic solar cells with improved operational stability. Nano Energy. **125** pp. 109542 (2024)

[69] Wang, K., Sun, C., Zhang, C., Bai, H., Sang, S., Li, Y., Chen, Z., Li, X., Meng, L. & Li, Y. Fine-tuning of film morphology through addition of a third component enables organic solar cells with efficiency over 18%, Materials Chemistry Frontiers. (2024)

[70] Li, Z., Song, D., Xu, Z., Qiao, B., Zhao, S., Wageh, S., Al-Ghamdi, A. & Huo, X. Improved uv sensitivity and charge transport in ptb7-th: Pc 71 bm solar cells doped with cadmium selenide quantum dots. Sustainable Energy & Fuels. **6**, 2053-2061 (2022)

[71] Becker-Koch, D., Albaladejo-Siguan, M., Hofstetter, Y., Solomeshch, O., Pohl, D., Rellinghaus, B., Tessler, N. & Vaynzof, Y. Doped organic hole extraction layers in efficient pbs and agbis2 quantum dot solar cells. ACS Applied Materials & Interfaces. **13**, 18750-18757 (2021)

[72] Zhang, X., Justo, Y., Maes, J., Walravens, W., Zhang, J., Liu, J., Hens, Z. & Johansson, E. Slow recombination in quantum dot solid solar cell using p–i–n architecture with organic p-type hole transport material. Journal of Materials Chemistry A. **3**, 20579-20585 (2015)

[73] Ueno, K., Oshikiri, T., Sun, Q., Shi, X. & Misawa, H. Solid-state plasmonic solar cells. Chemical Reviews. **118**, 2955-2993 (2017)

[74] Ogundele, A. & Mola, G. Ternary atoms alloy quantum dot assisted hole transport in thin film polymer solar cells. Journal Of Physics And Chemistry Of Solids. **171** pp. 110999 (2022)

[75] Zafar, M., Kim, B. & Kim, D. Improvement in performance of inverted organic solar cell by rare earth element lanthanum doped zno electron buffer layer. Materials Chemistry And Physics. **240** pp. 122076 (2020)

[76] Zhang, G., Chen, Q., Zhang, Z., Gao, Z., Xiao, C., Wei, Y. & Li, W. Niox nanoparticles hole-transporting layer regulated by ionic radius-controlled doping and reductive agent for organic solar cells with efficiency of 19.18%. Advanced Materials. **36**, 2310630 (2024)

[77] Jaffri, S., Ahmad, K., Abrahams, I., Kousseff, C., Nielsen, C. & Almutairi, B. Rare earth (sm/eu/tm) doped zro2 driven electro-catalysis, energy storage, and scaffolding in high-performance perovskite solar cells. International Journal of Hydrogen Energy. **48**, 29119-29141 (2023)

[78] Yuliantini, L., Nursam, N., Pranoto, L., Hidayat, J., Sova, R., Rahayu, E., Djamal, M., Yasaka, P., Boonin, K. & Kaewkhao, J. Photon up-conversion in er3+ ion-doped zno-al2o3-bao-b2o3 glass for enhancing the performance of dye-sensitised solar cells. Journal Of Alloys And Compounds. **954** pp. 170163 (2023)

[79] Zhang, Y., Dang, X., Kim, C. & Nguyen, T. Effect of charge recombination on the fill

factor of small molecule bulk heterojunction solar cells. Advanced Energy Materials. **1**, 610-617 (2011)

[80] El-Mahalawy, A., Amin, F., Wassel, A. & Salam, M. Overcoming the poor performance of n-cds/p-sns solar cells by plasmonic effect of gold and silver nanoparticles. Journal Of Alloys And Compounds. **923** pp. 166484 (2022)

[81] Liu, Y., Zojer, K., Lassen, B., Kjelstrup-Hansen, J., Rubahn, H. & Madsen, M. Role of the charge-transfer state in reduced langevin recombination in organic solar cells: A theoretical study. The Journal Of Physical Chemistry C. **119**, 26588-26597 (2015)

[82] Staudigel, J., Stößel, M., Steuber, F. & Simmerer, J. A quantitative numerical model of multilayer vapor-deposited organic light emitting diodes. Journal Of Applied Physics. **86**, 3895-3910 (1999)

[83] Vollbrecht, J., Lee, J., Ko, S., Brus, V., Karki, A., Le, W., Seifrid, M., Ford, M., Cho, K. & Bazan, G. Design of narrow bandgap non-fullerene acceptors for photovoltaic applications and investigation of non-geminate recombination dynamics. Journal Of Materials Chemistry C. **8**, 15175-15182 (2020)

[84] Huo, M., Hu, R., Zhang, Q., Chen, S., Gao, X., Zhang, Y., Yan, W. & Wang, Y. Morphology and carrier non-geminate recombination dynamics regulated by solvent additive in polymer/fullerene solar cells. RSC Advances. **10**, 23128-23135 (2020)

[85] Wang, Z., Wang, X., Tu, L., Wang, H., Du, M., Dai, T., Guo, Q., Shi, Y. & Zhou, E. Dithienoquinoxalineimide-based polymer donor enables all-polymer solar cells over 19% efficiency. Angewandte Chemie. **136**, 202319755 (2024)

[86] Son, D., Nasrun, R. & Kim, J. Tuning photovoltaic parameters in polymer solar cells through side-chain modification of donor polymer based on cyclopenta [c] thiophene-4, 6 (5h)-dione. Organic Electronics. **129** pp. 107059 (2024)

[87] Tian, L., Liu, C. & Huang, F. Recent progress in side chain engineering of y-series non-fullerene molecule and polymer acceptors. Science China Chemistry. **67**, 788-805 (2024)

[88] Scharber, M. & Sariciftci, N. Low band gap conjugated semiconducting polymers. Ad-

vanced Materials Technologies. **6**, 2000857 (2021)

[89] Lee, J., Lee, H., Oh, E., Lee, S., Phan, T., Li, S., Kim, T. & Kim, B. Rigid-and soft-block-copolymerized conjugated polymers enable high-performance intrinsically stretchable organic solar cells. Joule. **8**, 204-223 (2024)

[90] Jiang, Y., Sun, S., Xu, R., Liu, F., Miao, X., Ran, G., Liu, K., Yi, Y., Zhang, W. & Zhu, X. Non-fullerene acceptor with asymmetric structure and phenyl-substituted alkyl side chain for 20.2% efficiency organic solar cells. Nature Energy. pp. 1-12 (2024)

[91] Li, S., Xiao, Z., Li, J., Hu, Z., Yang, Y., Kan, B., Guo, D., Wan, X., Yao, Z. & Li, C. Calixarenes enabling well-adjusted organic-inorganic interface for inverted organic solar cells with 18.25% efficiency and multifold improved photostability under max power point tracking. Science China Chemistry. **66**, 195-201 (2023)

[92] Yang, Y., Xiao, Y., Xu, B. & Hou, J. Cross-linkable cathode interlayer for inverted organic solar cells with enhanced efficiency and stability. Advanced Energy Materials. **13**, 2301098 (2023)

[93] Huang, Q., Jing, J., Zhang, K., Chen, Y., Song, A., Liu, Z. & Huang, F. Simultaneous improvement of efficiency and stability of inverted organic solar cell via composite hole transport layer. Journal Of Materials Chemistry A. **10**, 23973-23981 (2022)

[94] Yang, S. & Yu, H. The modification of zno surface with natural antioxidants to fabricate highly efficient and stable inverted organic solar cells. Chemical Engineering Journal. **452** pp. 139658 (2023)

[95] Tang, H., Bai, Y., Zhao, H., Qin, X., Hu, Z., Zhou, C., Huang, F. & Cao, Y. Interface engineering for highly efficient organic solar cells. Advanced Materials. **36**, 2212236 (2024)

[96] Cui, Y., Xu, Y., Yao, H., Bi, P., Hong, L., Zhang, J., Zu, Y., Zhang, T., Qin, J. & Ren, J. Single-junction organic photovoltaic cell with 19% efficiency. Advanced Materials. **33**, 2102420 (2021)

[97] Zhao, H., Lin, B., Xue, J., Naveed, H., Zhao, C., Zhou, X., Zhou, K., Wu, H., Cai, Y. & Yun, D. Kinetics manipulation enables high-performance thick ternary organic solar cells

via r2r-compatible slot-die coating. Advanced Materials. **34**, 2105114 (2022)

[98] Wang, J., Zhang, M., Lin, J., Zheng, Z., Zhu, L., Bi, P., Liang, H., Guo, X., Wu, J. & Wang, Y. An asymmetric wide-bandgap acceptor simultaneously enabling highly efficient single-junction and tandem organic solar cells. Energy & Environmental Science. **15**, 1585-1593 (2022)

[99] Ma, Q., Jia, Z., Meng, L., Zhang, J., Zhang, H., Huang, W., Yuan, J., Gao, F., Wan, Y. & Zhang, Z. Promoting charge separation resulting in ternary organic solar cells efficiency over 17.5%. Nano Energy. **78** pp. 105272 (2020)

[100] Ogundele, A. & Mola, G. Semiconductor quantum dots as a mechanism to enhance charge transfer processes in polymer solar cells. Chemosphere. pp. 140453 (2023)

[101] Oseni, S., Osifeko, O., Boyo, A. & Mola, G. Simultaneous inclusion of quantum dots in multi-functional layers of thin film organic solar cells. AIP Advances. **13** (2023)

[102] Bi, P., Zheng, F., Yang, X., Niu, M., Feng, L., Qin, W. & Hao, X. Dual förster resonance energy transfer effects in non-fullerene ternary organic solar cells with the third component embedded in the donor and acceptor. Journal Of Materials Chemistry A. **5**, 12120-12130 (2017)

[103] Ma, X., Mi, Y., Zhang, F., An, Q., Zhang, M., Hu, Z., Liu, X., Zhang, J. & Tang, W. Efficient ternary polymer solar cells with two well-compatible donors and one ultranarrow bandgap nonfullerene acceptor. Advanced Energy Materials. **8**, 1702854 (2018)

[104] Hu, Z., Yang, L., Gao, W., Gao, J., Xu, C., Zhang, X., Wang, Z., Tang, W., Yang, C. & Zhang, F. Over 15.7% efficiency of ternary organic solar cells by employing two compatible acceptors with similar lumo levels. Small. **16**, 2000441 (2020)

[105] Li, K., Wu, Y., Tang, Y., Pan, M., Ma, W., Fu, H., Zhan, C. & Yao, J. Ternary blended fullerene-free polymer solar cells with 16.5% efficiency enabled with a higher-lumo-level acceptor to improve film morphology. Advanced Energy Materials. **9**, 1901728 (2019)

[106] Xie, L., Yang, C., Zhou, R., Wang, Z., Zhang, J., Lu, K. & Wei, Z. Ternary organic solar cells based on two non-fullerene acceptors with complimentary absorption and balanced

crystallinity. Chinese Journal Of Chemistry. **38**, 935-940 (2020)

[107] Ma, X., An, Q., Ibraikulov, O., Lévêque, P., Heiser, T., Leclerc, N., Zhang, X. & Zhang, F. Efficient ternary organic photovoltaics with two polymer donors by minimizing energy loss. Journal Of Materials Chemistry A. **8**, 1265-1272 (2020)

[108] Shim, M. & Guyot-Sionnest, P. Permanent dipole moment and charges in colloidal semiconductor quantum dots. The Journal Of Chemical Physics. **111**, 6955-6964 (1999)

[109] Xu, H., Song, J., Zhou, P., Song, Y., Xu, J., Shen, H., Fang, S., Gao, Y., Zuo, Z. & Pina, J. Dipole–dipole-interaction-assisted self-assembly of quantum dots for highly efficient light-emitting diodes. Nature Photonics. **18**, 186-191 (2024)

[110] Arquer, F., Talapin, D., Klimov, V., Arakawa, Y., Bayer, M. & Sargent, E. Semiconductor quantum dots: Technological progress and future challenges. Science. **373**, 8541 (2021)

[111] Melnychuk, C. & Guyot-Sionnest, P. Multicarrier dynamics in quantum dots. Chemical Reviews. **121**, 2325-2372 (2021)

[112] Deng, Y., Lin, X., Fang, W., Di, D., Wang, L., Friend, R., Peng, X. & Jin, Y. Deciphering exciton-generation processes in quantum-dot electroluminescence. Nature Communications. **11**, 2309 (2020)

[113] Carey, G., Abdelhady, A., Ning, Z., Thon, S., Bakr, O. & Sargent, E. Colloidal quantum dot solar cells. Chemical Reviews. **115**, 12732-12763 (2015)

[114] Dou, Y., Zhou, R., Wan, L., Niu, H., Zhou, J., Xu, J. & Cao, G. Nearly monodisperse pbs quantum dots for highly efficient solar cells: An in situ seeded ion exchange approach. Chemical Communications. **54**, 12598-12601 (2018)

[115] Sapra, S. & Sarma, D. Electronic structure and spectroscopy of semiconductor nanocrystals, The Chemistry of Nanomaterials: Synthesis. Properties And Applications. pp. 371-404 (2004)

[116] Smith, A. & Nie, S. Next-generation quantum dots. Nature Biotechnology. **27**, 732-733

(2009)

[117] Vastola, G., Zhang, Y. & Shenoy, V. Experiments and modeling of alloying in self-assembled quantum dots. Current Opinion In Solid State And Materials Science. **16**, 64-70 (2012)

[118] Dorfs, D. & Eychmüller, A. Multishell semiconductor nanocrystals. Zeitschrift Für Physikalische Chemie. **220**, 1539-1552 (2006)

[119] Chung, Y., Yang, C., Zheng, H., Tsai, P. & Wang, T. Synthesis and characterisation of Cd_xSe_{1-x} alloy quantum dots with composition-dependent band gaps and paramagnetic properties. RSC Advances. **8**, 30002-30011 (2018)

[120] Atkins, P. Paula j. Atkins' physical chemistry. (Oxford university press,2006)

[121] Mousa, A. Synthesis and characterisation of Pbs quantum dots. (2011)

[122] Jahangir, S., Frost, T., Stark, E., Deshpande, S. & Bhattacharya, P. A monolithic ingan/gan disk-in-nanowire electrically pumped edge-emitting green (λ = 533 nm. Laser On (001) Silicon, 72nd Device Research Conference, IEEE. pp. 35-36 (2014)

[123] Taleb, H. & Abedi, K. Modeling and design of photonic crystal quantum-dot semiconductor optical amplifiers. IEEE Transactions On Electron Devices. **61**, 2419-2426 (2014)

[124] Tamura, Y., Higo, A., Kiba, T., Thomas, C., Yunpeng, W., Sodabanlu, H., Yamashita, I., Sugiyama, M., Nakano, Y. & Murayama, A. Narrow line-width photoluminescence spectrum of gaas nanodisks fabricated using bio-template ultimate top-down processes. 14th IEEE International Conference On Nanotechnology, IEEE. pp. 221-224 (2014)

[125] Yang, C. & Li, S. Size, dimensionality, and constituent stoichiometry dependence of bandgap energies in semiconductor quantum dots and wires. The Journal Of Physical Chemistry C. **112**, 2851-2856 (2008)

[126] Zeng, P., Li, W., Zhao, Y. & Liu, M. Band gap modulation of lead sulfide QDs. Nano. **13**, 1850060 (2018)

[127] Nozik, A. Nanoscience and nanostructures for photovoltaics and solar fuels. *Nano Letters.* **10**, 2735-2741 (2010)

[128] Reimann, S. & Manninen, M. Electronic structure of quantum dots. *Reviews Of Modern Physics.* **74**, 1283 (2002)

[129] Tauc, J. Electron impact ionisation in semiconductors. Journal Of Physics And Chemistry Of Solids. **8** pp. 219-223 (1959)

[130] Vavilov, V. On photo-ionisation by fast electrons in germanium and silicon. Journal Of Physics And Chemistry Of Solids. **8** pp. 223-226 (1959)

[131] Nozik, A. Multiple exciton generation in semiconductor quantum dots. Chemical Physics Letters. **457**, 3-11 (2008)

[132] Binks, D. Multiple exciton generation in nanocrystal quantum dots–controversy, current status and future prospects. Physical Chemistry Chemical Physics. **13**, 12693-12704 (2011)

[133] Coe-Sullivan, S., Steckel, J., Woo, W., Bawendi, M. & Bulović, V. Large-area ordered quantum-dot monolayers via phase separation during spin-casting. Advanced Functional Materials. **15**, 1117-1124 (2005)

[134] Xia, Y., Nguyen, T., Yang, M., Lee, B., Santos, A., Podsiadlo, P., Tang, Z., Glotzer, S. & Kotov, N. Self-assembly of virus-like self-limited inorganic supraparticles from nanoparticles. Nature Nanotechnology. **6** pp. 580-587 (2011)

[135] Lee, J., Kwon, B., Park, H., Kim, H., Kim, M., Park, J., Kim, E., Yoo, S., Jeon, D. & Kim, S. Exciton dissociation and charge-transport enhancement in organic solar cells with quantum-dot/n-doped cnt hybrid nanomaterials. Advanced Materials. **25**, 2011-2017 (2013)

[136] Hwang, S., Lee, J., Kim, S., Park, J., Park, H., Ahn, C., Lee, K., Lee, T. & Kim, S. Flexible multilevel resistive memory with controlled charge trap b-and n-doped carbon nanotubes. Nano Letters. **12**, 2217-2221 (2012)

[137] Park, J., Lee, J., Hwang, S., Lee, S., Lee, H., Lee, B., Park, H., Kim, J., Yoo, S. &

Song, M. A zno/n-doped carbon nanotube nanocomposite charge transport layer for high performance optoelectronics. Journal Of Materials Chemistry. **22**, 12695-12700 (2012)

[138] Tung, V., Huang, J., Kim, J., Smith, A., Chu, C. & Huang, J. Towards solution processed all-carbon solar cells: A perspective. Energy & Environmental Science. **5**, 7810-7818 (2012)

[139] Vos, A. Detailed balance limit of the efficiency of tandem solar cells. Journal Of Physics D: Applied Physics. **13**, 839 (1980)

[140] Kim, S. & Walsh, A. Ab initio calculation of the detailed balance limit to the photovoltaic efficiency of single pn junction kesterite solar cells. Applied Physics Letters. **118** (2021)

[141] Shockley, W. & Queisser, H. Detailed balance limit of efficiency of p–n junction solar cells. Renewable Energy, Routledge. pp. 2 35- 32 54 (2018)

[142] Vos, A. Thermodynamics of photovoltaics. (Springer,2000)

[143] Landsberg, P. & Badescu, V. Solar cell thermodynamics including multiple impact ionisation and concentration of radiation. Journal Of Physics D: Applied Physics. **35**, 1236 (2002)

[144] Zhan, X., Tan, Z., Domercq, B., An, Z., Zhang, X., Barlow, S., Li, Y., Zhu, D., Kippelen, B. & Marder, S. A high-mobility electron-transport polymer with broad absorption and its use in field-effect transistors and all-polymer solar cells. Journal Of The American Chemical Society. **129**, 7246-7247 (2007)

[145] Few, S., Frost, J., Kirkpatrick, J. & Nelson, J. Influence of chemical structure on the charge transfer state spectrum of a polymer: Fullerene complex. The Journal Of Physical Chemistry C. **118**, 8253-8261 (2014)

[146] Jørgensen, M., Norrman, K., Gevorgyan, S., Tromholt, T., Andreasen, B. & Krebs, F. Stability of polymer solar cells. Advanced Materials. **24**, 580-612 (2012)

[147] Cheng, P. & Zhan, X. Stability of organic solar cells: Challenges and strategies. Chemical Society Reviews. **45**, 2544-2582 (2016)

[148] Park, Y., Lee, K., Lim, G., Seo, H., Kim, S., Kim, M., Yi, Y., Lee, H. & Son, D. Role of cdse and cdse@ zns quantum dots interlayers conjugated in inverted polymer solar cells. Organic Electronics. **82** pp. 105707 (2020)

[149] Park, S., Lee, H., Park, S., Kim, T., Park, S., Jung, Y. & Cho, S. Improved exciton dissociation efficiency by a carbon-quantum-dot doped workfunction modifying layer in polymer solar cells. Current Applied Physics. **21** pp. 140-146 (2021)

[150] Nam, M. Synergistic enhancement of charge generation and transfer in organic solar cells via a separate pbs quantum dot layer. Organic Electronics. **93** pp. 106150 (2021)

[151] Yang, X., Qiao, J., Chen, Z., Wen, Z., Yin, H. & Hao, X. Cdse quantum dot organic solar cells with improved photovoltaic performance. Journal Of Physics D: Applied Physics. **54**, 115504 (2021)

[152] Park, K., Jung, S., Kim, J., Ko, B., Shim, W., Hong, S. & Song, S. Boosting photovoltaic performance in organic solar cells by manipulating the size of mos2 quantum dots as a hole-transport material. Nanomaterials. **11**, 1464 (2021)

[153] Oseni, S., Osifeko, O., Boyo, A. & Mola, G. Tri-metallic quantum dot under the influence of solvent additive for improved performance of polymer solar cells. Journal Of Applied Polymer Science. **140**, 53293 (2023)

[154] Ogundele, A. & Mola, G. Enhanced collection of photocurrents using core–shell quantum dots decorated polymer composite films. Energy & Fuels. (2024)

[155] Lin, X., Wang, Y., Wu, J., Tang, Z., Lin, W., Nian, L. & Yi, G. Black phosphorus quantum dots based heterostucture boosting electron extraction for non-fullerene organic solar cells surpassing 15% power conversion efficiency. ACS Applied Energy Materials. **4**, 5905-5912 (2021)

[156] Sun, Y., Wei, Z., Zhao, C., Zhang, G., Zhang, G., Zhou, S., Zhang, Z., Yu, Y., Zhang, Q. & Li, X. Pdse2 quantum dots for improving the photovoltaic performance of nonfullerene organic solar cells. Solar RRL. **7**, 2200965 (2023)

[157] Shalaan, E., Ibrahim, E., Al-Marzouki, F. & Al-Dossari, M. Observation of mixed types

of energy gaps in some ii–vi semiconductors nanostructured films: Towards enhanced solar cell performance. Applied Physics A. **126**, 852 (2020)

[158] Al-Douri, Y., Khan, M. & Jennings, J. Synthesis and optical properties of ii–vi semiconductor quantum dots: A review. Journal Of Materials Science: Materials In Electronics. **34**, 993 (2023)

[159] Diroll, B., Guzelturk, B., Po, H., Dabard, C., Fu, N., Makke, L., Lhuillier, E. & Ithurria, S. 2d ii–vi semiconductor nanoplatelets: From material synthesis to optoelectronic integration. Chemical Reviews. **123**, 3543-3624 (2023)

[160] Wang, J., Xing, Y., Wan, F., Fu, C., Xu, C., Liang, F. & Luo, L. Progress in ultraviolet photodetectors based on ii–vi group compound semiconductors. Journal Of Materials Chemistry C. **10**, 12929-12946 (2022)

[161] Mayabadi, A., Mirabbaszadeh, K., Pawbake, A., Rondiya, S., Rokade, A., Waykar, R., Kulkarni, R., Pathan, H. & Jadkar, S. Electrochemical deposition of p-cdte nanoparticle thin films for solar cell applications. Journal Of Materials Science: Materials In Electronics. **28** pp. 18745-18754 (2017)

[162] Kurban, M., Malcıoğlu, O. & Erkoç, Ş. Ternary ii-vi alloys promising for application in photodetectors. Handbook Of ii-vi Semiconductor-based Sensors And Radiation Detectors. **1** pp. 87-107 (2023)

CHAPTER 3

MATERIALS, METHODS AND INSTRUMENTATION

3.1 Introduction

This chapter details the range of processes, materials, instruments, and methods utilized in the experimental procedures undertaken in this thesis. Firstly, the materials are categorised into optimising foreign component materials, transport/buffer layer materials, polymers and substrates used in the various experiments. The names of the suppliers, purity and specifications listed by the suppliers are later provided in each of the experimental sections of the papers. Also, the various synthesis methods and characterisation techniques are listed, stating the different instruments used for the characterisation. Moreover, the stages involved in the fabrication of devices are equally highlighted. The environmental conditions under which the experiments were conducted are also discussed. Finally, the instrumentation employed in analysing the data, the software used and the error in the analysis are accounted for in this chapter to ensure the reproducibility of the experiments.

3.2 Material resources

3.2.1 Transport/buffer layer materials

The transport layer materials used as hole transport and electron transport layers are poly(3,4-ethylene dioxythiophene):poly(styrene sulfonate) (PEDOT:PSS) and zinc oxide nano-particle ink suspension, respectively. The PEDOT:PSS (with a purity of 95–97% and a density of 1.011 g/mL) was supplied by Ossila Company Ltd., UK. The zinc oxide (CAS 793361) nanoparticle ink suspension was procured from Aldrich Chemical Company, Milwaukee, USA, with 99% purity (0.8 g/mL). The buffer layer materials, which are intermediate between the transport

and photoactive layers, include lithium fluoride (LiF) and molybdenum trioxide (MoO_3). These were used as purchased from Aldrich Chemical Company, Milwaukee, USA, with 99.97% purity. The choice of device architecture determines the selection of transport and buffer layers, as discussed in Chapters 4 to 6 of this thesis.

3.2.2 Photoactive materials

The polymers used as the photoactive functional layer in the various investigations are composed of donor and acceptor polymers. The donors are poly(3-hexylthiophene) (P3HT) and poly[4,8-bis[(2-ethylhexyl)oxy]benzo[1,2-b:4,5-b']dithiophene-2,6-diyl][3-fluoro-2-[(2-ethylhexyl)carbonyl]thieno[3,4-b]thiophenediyl] (PTB7). The acceptor materials are (6,6)-phenyl-C_{61}-butyric acid methyl ester ($PC_{60}BM$) and [6,6]-phenyl-C_{71}-butyric acid methyl ester ($PC_{71}BM$). They were procured from Ossila Company Ltd., UK, with 95-97% purity and used as received.

3.2.3 Anode and cathode materials

The anode and cathode materials are crucial in fabricating TFPSCs. The transparent conducting oxide material used in all the investigations carried out in this thesis is an indium-doped tin oxide (ITO) glass substrate. The unpatterned ITO glass substrates, measuring 30 by 30 cm^2, were purchased from Aldrich Chemical Company, Milwaukee, USA. The ITO was etched before use, as described in the experimental sections of Chapters 4 to 6. The top electrode employed in all the investigations is an aluminium coil, procured from Aldrich Chemical Company, Milwaukee, USA.

3.2.4 Semiconductor impurities

Foreign component materials are nanoparticles that are not fundamentally part of the functional layers of organic solar cells. Group II-VI semiconductor quantum dots (QDs) are the foreign component materials used in the investigations reported in this thesis. They include alloyed CdTeSe, ZnS, and core-shell CdS/ZnS QDs. The alloy QDs exhibit distinct properties that differ from their constituent elements due to bandgap engineering, lattice strain and defects, as well as surface state and composition distribution [1, 2, 3, 4]. This feature was leveraged when CdTeSe QDs were doped into the hole transport layer (PEDOT:PSS) in the fabrication of polymer solar cells. Furthermore, the importance of energy level alignment in enhancing charge separation, reducing voltage and energy losses, and improving the open-circuit voltage (V_{oc}) [5, 6, 7] was explored using ZnS QDs. The energy level alignment of SQDs

within the functional layers of polymer solar cells (PSCs) is governed by their conduction and valence band positions relative to the LUMOs and HOMOs of the donor and acceptor polymers. Specifically, effective electron transfer is achieved when the conduction band edge of the SQD is positioned below the LUMO of the donor polymer but above that of the acceptor polymer, thereby enabling efficient charge transport. The intermediate LUMO energy level ($\sim 3.49\,\text{eV}$) of ZnS QDs, which lies between the LUMO energy levels of P3HT ($\sim 3.2\,\text{eV}$) and PCBM ($\sim 4.4\,\text{eV}$), was exploited by incorporating them into the photoactive layer of P3HT:PCBM. Moreover, stable, enhanced absorption and better surface passivation can be achieved using core-shell QDs [8, 9]. Core-shell QDs ($Cd_xS/Zn_{1-x}S$), composed of a medium bandgap QD as the core and a relatively wide bandgap QD as the shell, were incorporated into the electron transport layer (ETL) of PTB7:$PC_{71}BM$.

3.3 Methods

3.3.1 Synthesis

Nanoparticles are commonly produced in nanotechnology through two main methods: the top-down and bottom-up approaches [10, 11]. The top-down approach involves sequentially breaking down bulk materials into smaller particles mainly through physical or mechanical processes (see Figure 3.1). Examples of top-down synthesis are ball milling, mechanical cutting, laser ablation, etching and lithography. In contrast, the bottom-up approach builds complex structures like nanoparticles or quantum dots by assembling atoms or molecules through chemical processes shown in Figure 3.1. Examples of bottom-up methods are chemical vapour deposition (CVD), sol-gel method, self-assembly, atomic layer deposition (ALD), colloidal synthesis, hydrothermal and solvothermal processes, and microwave-assisted synthesis. The top-down approach exhibits several disadvantages including surface defect, lack of precision, material waste, cumbersome in achieving desired morphologies, and lack of precision. However, the bottom-up approach displays interesting advantages including better precision, controlled size and morphology, fewer defects and versatility [12, 13, 14].

In this study, semiconductor quantum dots were synthesised using hydrothermal and microwave-assisted methods, both of which are bottom-up approaches. Hydrothermal synthesis offers benefits, such as precise control over nanoparticle size, shape, and crystallinity. The slow reaction rate promotes uniform particle growth, resulting in consistent particle distribution. This technique is also well-suited for producing materials that are sensitive to

elevated temperatures. Furthermore, its scalability and versatility allow the production of various materials, including sulphides, oxides, and complex composites [15, 16, 17]. Similarly, microwave-assisted synthesis ensures faster reaction time from hours to minutes by enabling direct interaction of microwaves with reactants. Also, it encourages energy efficiency reducing energy costs and cheaper synthesis processes. Moreover, it produces uniform particle growth by providing uniform volumetric heating. Above all, microwave-assisted synthesis produces a higher yield of QDs and purer products due to facile reaction rates and reduced exposure to impurities [18, 19, 20].

3.3.2 Characterisation techniques

The as-synthesised semiconductor quantum dots were subjected to various characterisations for various reasons. Firstly, it was essential to verify the successful synthesis of the intended nanoparticles, which was confirmed through energy-dispersive X-ray spectroscopy (EDS) analysis. Also, other morphologies (size, structural, phase purity, functional group etc.) of the as-

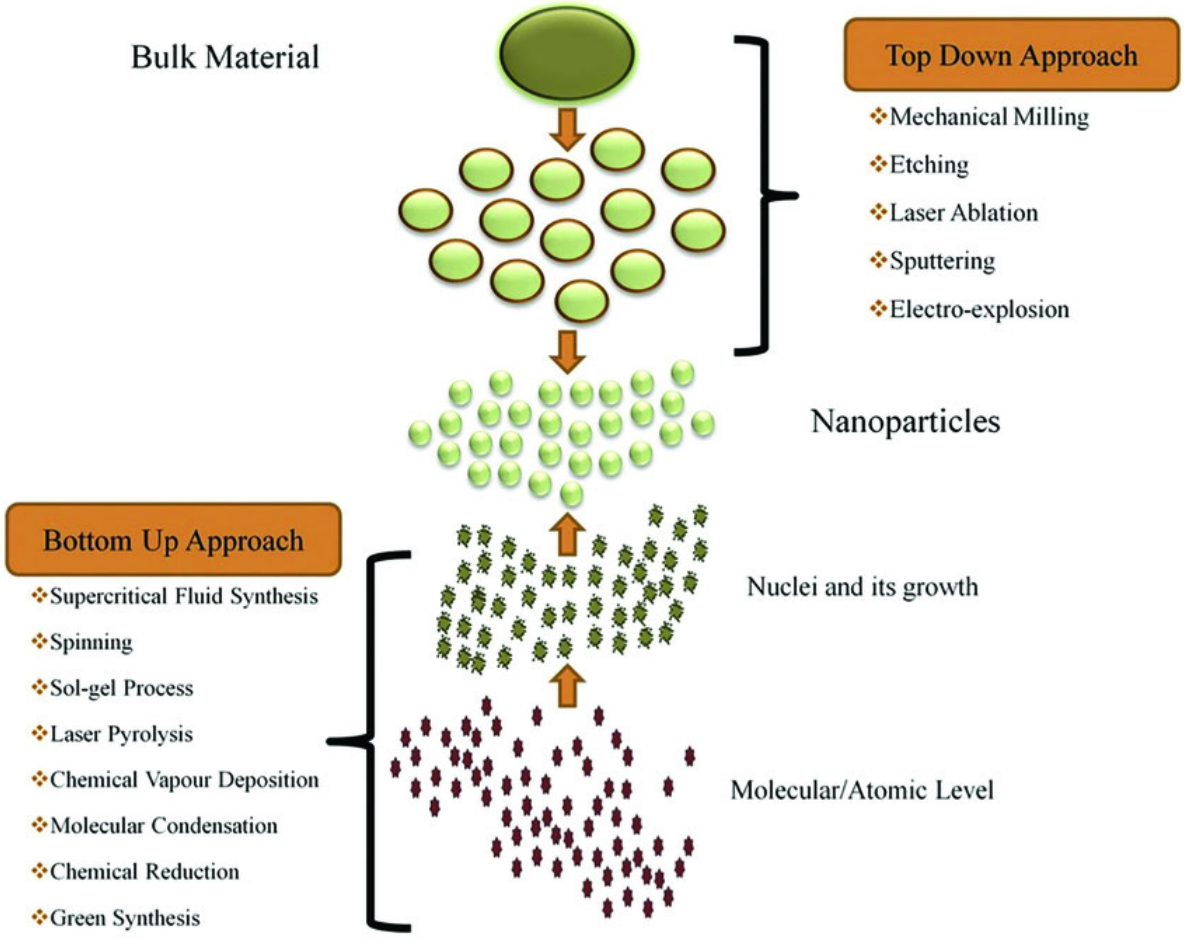

Figure 3.1: Synthesis of nanoparticles (NPs) via top-down and bottom-up approaches [10].

synthesised QDs were observed using scanning electron microscope (SEM), transmission electron microscope (TEM) and Fourier transform infrared spectroscopy (FTIR). The electronic and optical properties such as energy bandgap determination, quenching behaviour, charge transfer capabilities, exciton binding energy and quantum yields of quantum dots (QDs) were investigated both with and without the functional layer of PSCs using UV-visible absorption and photoluminescence (PL) spectroscopy.

3.3.3 Device Fabrication

Upon satisfactory analysis of the electronic and optical properties of the as-synthesised quantum dots (QDs), the fabrication process follows using the required device architectures. The semiconductor quantum dot (SQD) material can be applied in the photoactive layer, transport layers, or between the layers. N-type QDs and p-type QDs can be applied in the electron transport layer (ETL) and hole transport layer (HTL), respectively. Both types can also be applied in the photoactive layer or as interlayers for hole extraction or electron extraction. In this study, the alloyed QD was used in the HTL, core QDs in the active layer, and core-shell QDs in the ETL, under ambient conditions with relatively low humidity between 25% and 35%. The performance parameters are reported in Chapters 4 to 6. The important stages in the fabrication process include the preparation of ITO-doped glass substrates, spin-coating of layers, annealing, and mounting of the finished device onto masks. The first transport layer is usually coated on the back electrode, followed by the coating of the active layer. The other transport layers (ETL or HTL) are typically deposited using a vacuum chamber along with the top electrode. The films are thermally annealed between spin-coating processes (see Sections 4.3.3, 5.3.3, and 6.3.3). The fabricated devices are subjected to electrical measurements using solar simulators. The current-voltage characteristics, under both dark and illuminated conditions, are used to obtain important data for evaluating the device performance, as explained in Section 2.5.1. The spectral responses of device films are also evaluated using UV-visible absorption and photoluminescence (PL) spectroscopy (see Section 2.5.2).

3.4 Instrumentation

The characterisation and fabrication processes were carried out using key instruments listed in sections 3.3.2 and 3.3.3. Each instrument was carefully chosen to align with the objectives established in the investigations. For instance, the UV-visible and photoluminescence (PL) measurements were conducted using the Rayleigh UV1601 and PerkinElmer LS-45 fluorescence

spectrophotometers, respectively. The use of the UV1601 spectrophotometer followed standard operating procedures (SOP), where the baseline must first be acquired to ensure precision in the measurements. The PL PerkinElmer LS-45 fluorescence spectrophotometer followed similar, but more extensive, SOPs, with various stages of procedures required before use. SOPs were also followed for the FTIR spectrophotometer.

The X-ray diffraction (XRD), scanning electron microscopy (SEM), and transmission electron microscopy (TEM) instruments were located in the university's microscopy units and managed by highly skilled staff. The XRD system is a Bruker D8 Discover X-ray Diffractometer equipped with a Cu-Kα radiation source. The SEM and TEM instruments are specified as SEM-JEOL JSM6100, Zeiss Evo SEM, and TEM-JEOL JEM1010, respectively. The spin-coater (KW-4A, made in the USA) was used for coating, powered by a vacuum pump model TW-1A with a vacuum pressure of 10 Pa. The computer-interfaced Keithley (HP2420) source meter, under 1.5 AM solar simulator illumination (model SS50AAA) calibrated to a light intensity of 100 W/cm^2, was utilised. The Edward Auto 306 vacuum deposition unit was operated at a pressure of 10^{-6} mBar, and the precise thicknesses of the transport layer and top electrode were obtained during the deposition processes. The data acquired from these instruments were processed using licensed OriginLab software, with uncertainties recorded to the nearest two or three decimal places.

References

[1] Bailey, R. & Nie, S. Alloyed semiconductor quantum dots: Tuning the optical properties without changing the particle size. Journal of The American Chemical Society. **125**, 7100-7106 (2003)

[2] Vaxenburg, R. & Lifshitz, E. Alloy and heterostructure architectures as promising tools for controlling electronic properties of semiconductor quantum dots. Physical Review B. Condensed Matter and Materials Physics. **85**, 075304 (2012)

[3] Yang, H., Li, R., Zhang, Y., Yu, M., Wang, Z., Liu, X., You, W., Tu, D., Sun, Z. & Zhang, R. Colloidal alloyed quantum dots with enhanced photoluminescence quantum yield in the nir-ii window. Journal of the American Chemical Society. **143**, 2601-2607 (2021)

[4] Kim, J., Hwang, D., Jung, H., Kim, K., Pham, X., Lee, S., Byun, J., Kim, W., Kim, H. & Hahm, E. High-quantum yield alloy-typed core/shell cdsezns/zns quantum dots for bio-applications. Journal of Nanobiotechnology. **20**, 22 (2022)

[5] Li, P. & Lu, Z. Interface engineering in organic electronics: Energy-level alignment and charge transport. Small Science. **1**, 2000015 (2021)

[6] Yan, Y., Zhang, Y., Liu, Y., Shi, Y., Qiu, D., Deng, D., Zhang, J., Wang, B., Adil, M. & Amin, K. Simultaneously decreasing the bandgap and voc loss in efficient ternary organic solar cells. Advanced Energy Materials. **12**, 2200129 (2022)

[7] Ma, R., Liu, T., Luo, Z., Guo, Q., Xiao, Y., Chen, Y., Li, X., Luo, S., Lu, X. & Zhang, M. Improving open-circuit voltage by a chlorinated polymer donor endows binary organic solar cells efficiencies over 17%. Science China Chemistry. **63** pp. 325-330 (2020)

[8] Selopal, G., Zhao, H., Wang, Z. & Rosei, F. Core/shell quantum dots solar cells. Advanced Functional Materials. **30**, 1908762 (2020)

[9] Huang, X., Tong, X. & Wang, Z. Rational design of colloidal core/shell quantum dots for optoelectronic applications. Journal of Electronic Science and Technology. **18**, 100018 (2020)

[10] Khanna, P., Kaur, A. & Goyal, D. Algae-based metallic nanoparticles: Synthesis, characterisation and applications. Journal of Microbiological Methods. **163** pp. 105656 (2019)

[11] Baig, N., Kammakakam, I. & Falath, W. Nanomaterials: A review of synthesis methods, properties, recent progress, and challenges. Materials Advances. **2**, 1821-1871 (2021)

[12] Abid, N., Khan, A., Shujait, S., Chaudhary, K., Ikram, M., Imran, M., Haider, J., Khan, M., Khan, Q. & Maqbool, M. Synthesis of nanomaterials using various top-down and bottom-up approaches, influencing factors, advantages, and disadvantages: A review. Advances in Colloid and Interface Science. **300** pp. 102597 (2022)

[13] Kumar, N., Salehiyan, R., Chauke, V., Botlhoko, O., Setshedi, K., Scriba, M., Masukume, M. & Ray, S. Top-down synthesis of graphene: A comprehensive review. FlatChem. **27** pp. 100224 (2021)

[14] Jia, X., Khan, W., Wu, Z., Choi, J. & Yip, A. Modern synthesis strategies for hierarchical zeolites: Bottom-up versus top-down strategies. Advanced Powder Technology. **30**, 467-484 (2019)

[15] Gan, Y., Jayatissa, A., Yu, Z., Chen, X. & Li, M. Hydrothermal synthesis of nanomaterials. Journal of Nanomaterials. (2020)

[16] Facure, M., Schneider, R., Mercante, L. & Correa, D. Rational hydrothermal synthesis of graphene quantum dots with optimized luminescent properties for sensing applications. Materials Today Chemistry. **23** pp. 100755 (2022)

[17] Ghosh, T., Sahoo, R., Ghosh, S., Banerji, P. & Das, N. Simplistic hydrothermal synthesis approach for fabricating photoluminescent carbon dots and its potential application as an efficient sensor probe for toxic lead (ii) ion detection. Frontiers of Chemical Science And Engineering. **17**, 536-547 (2023)

[18] Kumar, A., Kuang, Y., Liang, Z. & Sun, X. Microwave chemistry, recent advancements, and eco-friendly microwave-assisted synthesis of nanoarchitectures and their applications: A review. Materials Today Nano. **11** pp. 100076 (2020)

[19] Basoglu, A., Ocak, *textU*. & *textGumrukcuoglu*, A. Synthesis of microwave-assisted flu-

orescence carbon quantum dots using roasted–chickpeas and its applications for sensitive and selective detection of fe3+ ions. Journal of Fluorescence. **30**, 515-526 (2020)

[20] Shkir, M., Khan, Z., Chandekar, K., Alshahrani, T., Kumar, A. & AlFaify, S. A facile microwave synthesis of cr-doped cds qds and investigation of their physical properties for optoelectronic applications. Applied Nanoscience. **10** pp. 3973-3985 (2020)

CHAPTER 4

TERNARY ATOMS ALLOY QUANTUM DOT ASSISTED HOLE TRANSPORT IN THIN FILM POLYMER SOLAR CELLS

Journal of Physics and Chemistry of Solids 171 (2022) 110999

Contents lists available at ScienceDirect

Journal of Physics and Chemistry of Solids

journal homepage: www.elsevier.com/locate/jpcs

Ternary atoms alloy quantum dot assisted hole transport in thin film polymer solar cells

Abiodun Kazeem Ogundele [a,b], Genene Tessema Mola [a,*]

[a] School of Chemistry & Physics, University of KwaZulu-Natal, Pietermaritzburg Campus, Private Bag X01, Scottsville, 3209, South Africa
[b] Department of Pure & Applied Physics, Southwestern University, Nigeria, Ogun State, Nigeria

ARTICLE INFO

Keywords:
Quantum confinement effect
Multiple excitons generation
Quantum dots
Ohmic contact

ABSTRACT

Quantum confinement effects and multiple exciton generation (MEG) were explored in this investigation to assist the hole transport and improved trapping of light in thin film solar cells (TFOSCs). The popular organic transport material Poly (3,4-ethylene dioxythiophene): polystyrene sulfonate (PEDOT:PSS) is employed here for effective electron blocking and hole transport processes through doping with quantum dots (QD). Alloyed CdTeSe QD is used, at different concentrations, in PEDOT:PSS layer to fabricate TFOSCs in the convectional device structure consisting of molecules blended as poly (3-hexylthiophene): (6, 6)-phenyl- C61-butyric acid methyl ester (P3HT: PCBM) solar absorber. A remarkable increase in performance of the devices was achieved from TFOSC whose HTL doped with QDs that resulted in an optimal boost in power conversion efficiency (PCE) as high as 111.7% relative to the reference cell. The results suggest that the doping of HTL with the alloy of CdTeSe quantum dots assisted in electron blocking, and improved hole collection as well as improved light trapping at the interface between the solar absorber layer and HTL.

Abstract

Quantum confinement effects and multiple exciton generation (MEG) were explored in this investigation to assist the hole transport and improved trapping of light in thin film solar

cells (TFOSCs). The popular organic transport material Poly (3,4-ethylene dioxythiophene): polystyrene sulfonate (PEDOT:PSS) is employed here for effective electron blocking and hole transport processes through doping with quantum dots (QD). Alloyed CdTeSe QD is used, at different concentrations, in PEDOT:PSS layer to fabricate TFOSCs in the convectional device structure consisting of molecules blended as poly (3-hexylthiophene): (6, 6)-phenyl-C61-butyric acid methyl ester (P3HT: PCBM) solar absorber. A remarkable increase in performance of the devices was achieved from TFOSC whose HTL doped with QDs that resulted in an optimal boost in power conversion efficiency (PCE) as high as 111.7 % relative to the reference cell. The results suggest that the doping of HTL with the alloy of CdTeSe quantum dots assisted in electron blocking, and improved hole collection as well as improved light trapping at the interface between the solar absorber layer and HTL.

4.1 Introduction

Organic solar cells (OSCs) have continued to be among the top research in the Photovoltaic (PV) research field in the past three decades due to their various advantages ranging from the ease of device processing, cost-effective, lightweight, flexibility of the device which give them edge over a more matured technology as copper indium gallium selenide (CIGS) or silicon solar cells whose drawback includes complex manufacturing process, rigidity, high cost of productions and affordability. The main factors slowing mass production of OSC in the energy market are low power conversion efficiency (PCE) and stability [1]. Hence, the need for more fruitful research works in this field is necessary to produce stable OSC. The most effective OSC device architecture to date is bulk heterojunction (BHJ) design which involves the process of photon absorptions, exciton generations, dissociation, charge percolation, and their transportations to the electrodes where they are extracted to external circuits. The continuous quest for improved device performance of organic solar cells has included the exploitation of quantum dots (QDs) in many ways [2, 3, 4, 5, 6]. The invaluable and promising features of QDs have been employed in various applications (photonics and biomedical, electronics, and renewable energy). Quantum dots are special types of semiconducting tiny nanocrystal materials whose lengths range from 2-10 nm. These characteristic features include glowing when stimulated by an external source like ultraviolet (UV) light, the ability to exhibit quantum confinement effects, and multiple excitons generations (MEG) [7]. Quantum confinement occurs when the size of the QD approaches the material's exciton Bohr radius where the electrons' energy level can no longer be treated as a continuous band but as discrete energy levels. Excitons generated

by the absorption of photons in QDs can be re-emitted because of the quantum confinement effect at different wavelengths. This is an advantage in OSC where ultra-violet UV light can be trapped by QDs to generate light in the visible region using gold QDs that can be easily absorbed by the photoactive layer. Figure 4.1 illustrates the quantum dots size dependent on photoluminescence where small QDs that have a large bandgap generate UV light while large QDs produce longer wavelengths. This attribute makes it possible for QD to harvest a wide range of solar spectrum since the sizes between the largest and smallest of QDs account for other colours of light within the spectrum [8]. The characteristic quantum effect confinement of QDs helps to tune its light absorption range owing to its ability to show unique luminescence features and electronic properties like wide and continuous spectra, narrow absorption spectral, and stability while its energy level can also be controlled to improve charge separation of excitons [9].

The impacts of QDs when employed in a hole transport material (HTL), especially poly (3, 4 ethylene dioxythiophene): poly-styrene-sulfonate (PEDOT: PSS) as well as their joint roles in the device performance of conventional OSC architecture have been investigated. Satoh et al. [10] reported PEDOT:PSS to have the highest efficiency among the conductive organic materials with a dimensionless figure of merit (ZT) 0.42 where Z is a reduction factor that is dependent on Seebeck coefficient, electrical resistivity, and thermal conductivity where T is the absolute temperature. PEDOT:PSS is also widely used as a transparent conductive polymer because of its high ductility [10]. An ideal bulk heterojunction BHJ solar cell has five layers, namely the transparent conducting oxide substrate which serves as an anode (e.g. indium tin oxide (ITO), fluorine tin oxide (FTO)), hole transport layer HTL (also called buffer layer), photo-active layer (a blend of donor polymer and fullerene or non- fullerene acceptor), electron transport layer (ETL), a cathode (usually a metal like Aluminium, Silver). A typical HTL is a wide bandgap p-type semiconductor [11]]. PEDOT: PSS has been widely used as HTL because of its wide bandgap and ability to align the work function with donor polymer molecules in the photoactive layer. However, it has some shortcomings which include degradation in devices and chemical stability due to its acidity and hydrophilic nature [12, 13]. These limitations among others as the ineffective ability to block electron diffusion into the hole transport layer (HTL) contribute to its ineffective optimal performance as HTL. An application of nickel sulphide nanoparticles in the PEDOT:PSS of thin film organic solar cells (TFOSCs) has been demonstrated by Mohammed et al. [14], it led to a significant improvement in the power conversion efficiency (PCE) of TFOSC while the incorporation of graphene oxide-germanium

quantum dots in HTL as reported by Amollo et al. [15] also led to a 50% improvement in PCE of the solar cells. The features of quantum dots highlighted above are expected to improve charge transport processes at the interfaces between the anode and photoactive layer. The applications of compound semiconductors consisting of cadmium in both organic and inorganic solar cells have contributed to the successes in photovoltaic solar cells in the past as demonstrated in the use of alloy-structured $CdSe_xTe_{1-x}$ as a ternary third component in the photoactive layer of DPP:PC61BM [16]. Also, both quantum dots of CdTe and CdSe have been used as solar cells in different ways namely metal junction solar cells [17, 18, 19], quantum dot-sensitised solar cells (QDSCs) [20, 21, 22], and thin film polymer solar cells (TFPSCs) [23, 24, 25].

This study investigated and subsequently reported the effects of alloyed CdTeSe quantum dots doped in the PEDOT: PSS as hole transport material in the fabrication of a photo-active layer of poly (3-hexylthiophene): (6, 6)-phenyl- C61-butyric acid methyl ester (P3HT:PCBM) hybrid organic solar cells.

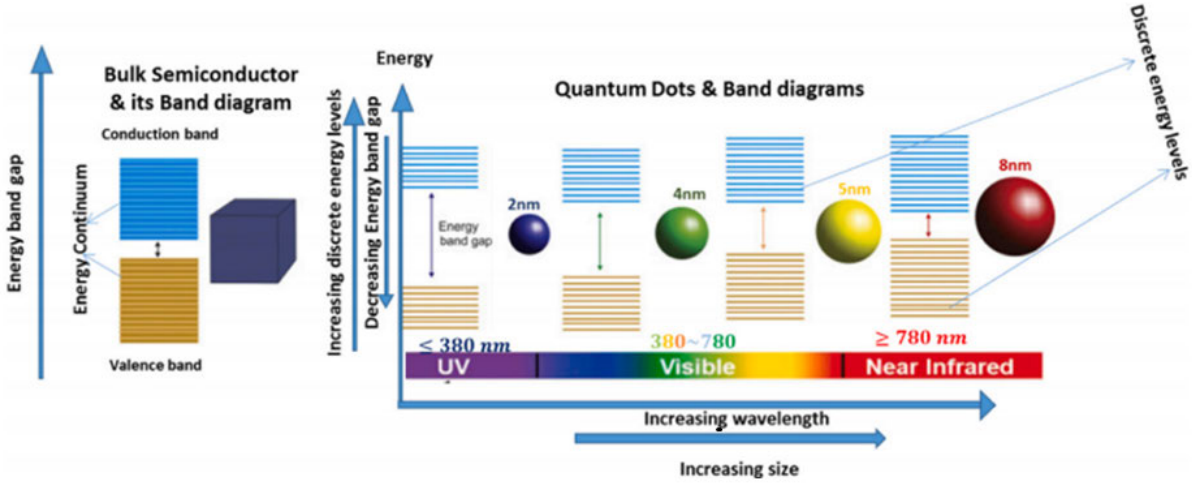

Figure 4.1: Bulk semiconductors with a constant bandgap and intrinsic characteristics, along with quantum dots (QDs) that exhibit changes in bandgap energy in response to size-dependent photoluminescence emission, contribute to the effective light harvesting of PSCs.

4.2 Experimental approach

4.2.1 Material resources

The chemicals and the device substrates used in this study were obtained from Sigma-Aldrich Limited and Ossila limited and were used as received. The chemicals include poly (3, 4 ethy-

lene dioxythiophene): poly-styrene-sulfonate (PEDOT: PSS), poly 3-hexylthiophene (P3HT), (6,6)-phenyl-C61-butyric acid methyl ester (PCBM) with 95% purity was bought from Ossila Company Ltd UK, while indium tin oxide (ITO) coated glass substrates and ethylene glycol with 99.8% purity from Sigma-Aldrich Co. USA.

4.2.2 Synthesis of CdTeSe quantum dots

The procedure reported in [26, 27] was adopted in the synthesis of CdTeSe quantum dots. It involved the synthesis of CdTeSe QD in aqueous media obtained from two precursors and the application of thioglycolic acid as a thiol stabilizer. This was achieved by dissolving a mixture of 1.28 g (6.66 mmol) of sodium hydrogen telluride (NaHTe) granules and 0.78 gram (14.01 mmol) of sodium borohydride (NaBH4) with 20 mL of millipore water in 50 mL round bottom flask situated in an ice bath under a supply of argon gas for 12 hours. This led to the formation of a precursor (NaHTe) evident with pink coloration. This step was followed using the same mole ratio for the preparation of NaHSe precursor using selenium powder with the appearance of purple coloration which indicated the second precursor. Eventually, a 1 gram, 5.46 mmol of cadmium chloride was then added into a 250ml capacity 3- neck round bottom flask, followed by the addition of 0.92 mL (0.0125M) of thioglycolic acid and 200 mL of millipore water, the mixture was stirred to a pH 11 with 1M sodium hydroxide and allowed to de-aerate for 30 minutes under a supply of argon. Both NaHSe precursor and inert NaHTe precursor were simultaneously injected into the mixture after which a reflux at 100°C for 1 h. The setup was left under argon gas for 4 hours. The monitoring of absorption and fluorescence was done at predetermined intervals of time employing aliquots of the emerging quantum dot solution. The reaction was stopped at the desired emission maxima and allowed to cool under ambient temperature. Lastly, the precipitation of fine crystals was done using acetone under centrifugation, while purification was done with methanol and ethanol. Further purification was done to remove excess NaHTe or NaHSe by re-dissolving in ultrapure water and later precipitating out with ethanol. The clean QDs were stored in the dark for more characterisation.

4.2.3 Device fabrication

The un-patterned indium doped tin oxide (ITO) coated glass substrates with the resistance of about 15 Ω/sq were carefully etched by partially covering with a photoresist and partially immersing the part to be etched in a warm yet bubble-free acidic solution composed of hydrochloric acid (HCl), water (H_2O), and nitric acid (HNO_3) in the ratio 12:1:12, respectively.

The substrates were subsequently cleaned with the aid of an ultrasonic bath using deionized water, acetone, and isopropanol for about ten minutes each sequentially. This was followed by drying the substrates in a nitrogen environment before eventually being baked in an oven at 120°C for twenty minutes under ambient conditions. The QD sample was dispersed in ethylene glycol solvent. The choice of ethylene glycol as solvent was determined due to its ability to aid the conductivity of PEDOT:PSS as well as reduce phase separation of inorganic QDs. Eventually, the QDs were used as a dopant in the PEDOT:PSS hole transport layer (HTL) at different concentrations by volume of QDs solution. The doped PEDOT:PSS was spin-coated on the substrate at about 3500 rpm for 60 seconds and annealed in an oven at 120°C for 20 minutes under ambient conditions. The photoactive layers of P3HT:PCBM were prepared at a 1:1 ratio by weight and dissolved in a chloroform solvent. The photoactive solutions were stirred on a hot plate for three hours at a temperature of 40°C to ensure a thorough blend. The active layers were then spin-coated on the dried PEDOT:PSS/CdTeSe QD at 1200 rpm for 40 seconds. The samples were then transferred to the furnace at 90°C for 5 minutes in a nitrogen atmosphere. Finally, thin layers of lithium fluoride (LiF) 0.4 nm and an aluminum (Al) top electrode of 90

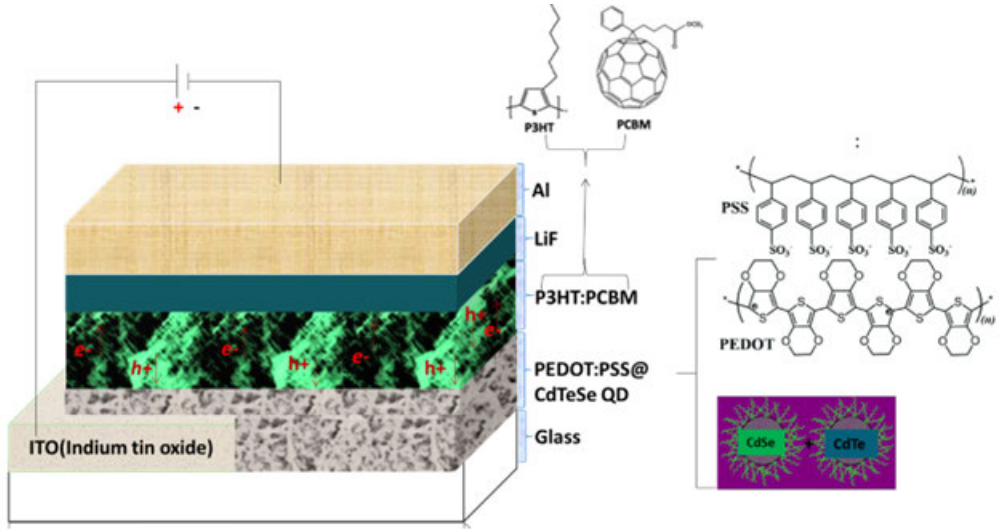

Figure 4.2: Solar cell device architecture consisting of various layers of materials including modified HTL.

nm in thickness were deposited using an Edward Auto 306 vacuum deposition unit at a pressure of 10^{-6} mbar. Upon completion of deposition with different concentrations (1%, 3%, 5%, and 7%) of QD-doped hole transport layers (PEDOT:PSS/CdTeSe), the devices composed of different layers of materials as Glass/ITO/PEDOT:PSS/QD/P3HT:PCBM/LiF/Al are compared with a reference cell fabricated without QDs in the HTL (see Figure 4.2). The electrical properties were measured using a computer-interfaced Keithley (HP2420) source meter under

1.5 AM solar simulator illumination (model SS50AAA) at a light intensity of 100 mWcm^{-2}.

4.3 Results and discussion

4.3.1 SEM and TEM observations

The physical, morphological and structural properties of the ternary molecules alloy (CdTeSe) quantum dot were characterized with the aid of a scanning electron microscope (SEM) and transmission electron microscope (TEM) as shown in Figure 4.3. The SEM and TEM images as analysed revealed (as shown in Figures 4.3a, c & d respectively) that the diameter of QD ranges from 2.35 nm to 5.39 nm while crystal fringes shown in Figure 4.3d underscored a coordinated crystalline structure. The energy dispersive X-ray (EDX) (see Figure 4.3b) clearly showed the presence of constituent elements cadmium, selenium, and telluride in the powder form of the QDs. However, the appearance of elements like gold was due to its use as a target in scanning electron microscopy. A fairly uneven morphology could be attributed to the formation of different-sized nanoparticles in the medium.

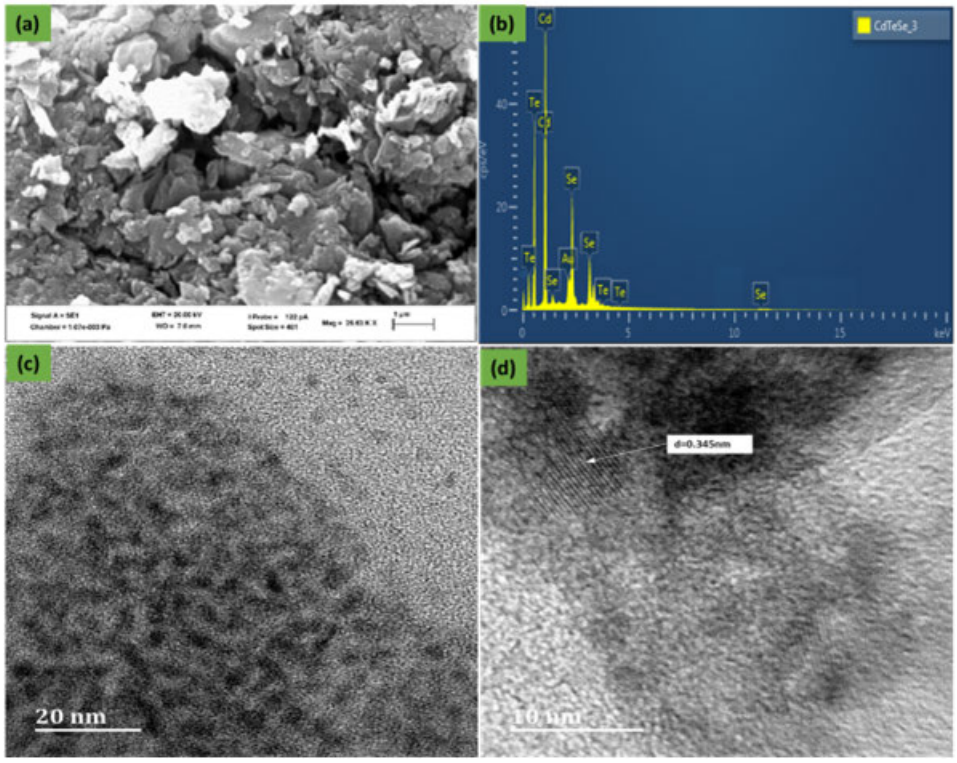

Figure 4.3: (a) Scanning electron microscopy (SEM) image of CdTeSe QDs, (b) Energy dispersive X-ray (EDX) analysis revealing elemental compositions of CdTeSe QDs, (c) & (d) Transmission electron microscopy (TEM) images of CdTeSe QDs at resolution of 20 nm and 10 nm, respectively.

4.3.2 Optical characterisation of HTL films

The optical absorption of the hole transport layers was investigated using a UV-Vis spectrometer. The optical transmission spectra of PEDOT:PSS with and without QD coated on ITO are provided in Figure 4.4c. The pristine and the modified HTL showed similar transmittance of about 70% at 403 nm. Consequently, it can be concluded that the inclusion of a small quantity of QDs in the PEDOT:PSS layer did not impair the optical transmission through the HTL layer [15]. The optical absorption of the doped PEDOT:PSS positively influenced the light-harvesting ability of the active layer [28] by way of the quantum confinement effect. This was evident in the broad absorption ranges of the active layer film as well as the formation of new peaks in the short and far infrared regions as provided in Figure 4.4c. The absorption spectra were taken from solar cell devices consisting of several layers of materials and HTL with/without QDs as Glass/ITO/PEDOT:PSS/P3HT:PCBM/LiF/Al. The absorption spectra provided in Figure 4.4c clearly showed a prominent peak at 512 nm representing the absorbance of P3HT:PCBM while the peaks near 400 nm could be the excitation of the metal nanoparticles in HTL. The HTL layers in the devices were doped at various concentrations of QDs 5%, 7%, 3%, and 1% (see Figure 4.4c) resulting in increased absorbance and absorbance width with QDs concentration, which is more evident at 5% and 7% doping levels. Enhanced optical absorptions are attributed to the characteristics of quantum confinement and multiple exciton generation effects of the QDs. The absorbance of the films doped at different concentrations of QDs exhibited a left shift, an indication of the reduced sizes of the QDs leading to a shorter absorption wavelength, short infrared region-shift with the presence of the vibrionic shoulder attributed to P3HT. Multiple exciton generations also manifested with the creation of another intermediate band around 380-420 nm as shown in Figure 4.4c.

The Tauc's relation [29] was used to determine the optical energy band gap, E_g, based on the relation given by $(\alpha h\nu)^\gamma = B\,(h\nu - E_g)$. Where α is the absorption coefficient; $h\nu$ is the photon energy in eV; h is Planck's constant; ν is the frequency of photon energy $(\nu = \frac{c}{\lambda})$, where c and λ are the speed and wavelength of light respectively. B is a constant that depends on the material (amorphous or crystalline), and γ is a constant dependent on whether the material has a direct allowed transition $(\gamma = 2)$ or an indirect allowed transition $(\gamma = \frac{1}{2})$. The plot of $(\alpha h\nu)^\gamma$ against $h\nu$ was used to determine E_g when the vertical axis i.e. $(\alpha h\nu)^\gamma$ is equal to zero. The transition involved in alloyed CdTeSe QD is a direct allowed transition hence γ was set at 2 as shown in the inset of Figure 4.4b.

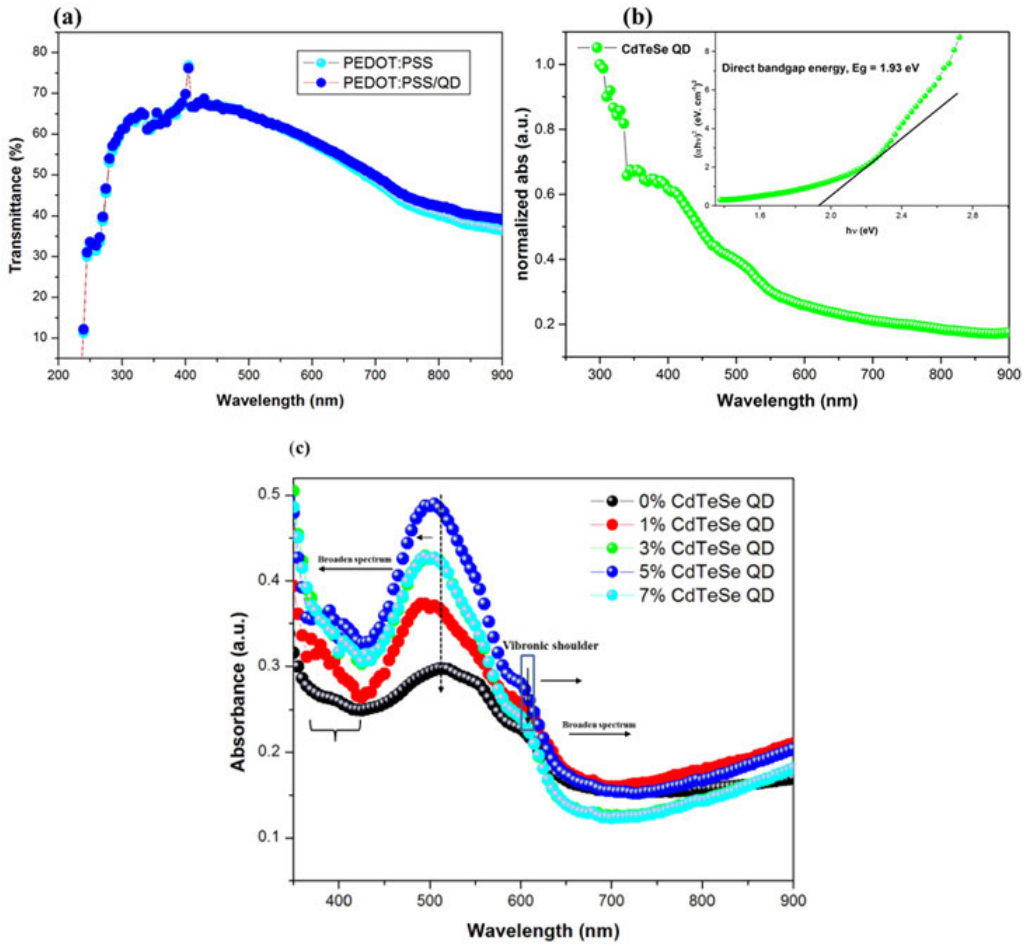

Figure 4.4: (a) UV–Vis transmittance spectra of PEDOT:PSS films with/without QD as HTL (b) the UV–Vis absorption spectra of CdTeSe QDs dispersed in Ethylene glycol and inset of the optical bandgap of the CdTeSe. (c) Optical absorption spectra of thin film solar cell based on P3HT:PCBM active layer using HTL PEDOT:PSS doped with QDs and reference cell.

4.3.3 J-V characteristics

The effects of CdTeSe quantum dots on the performance of thin film polymer organic solar cells were studied using a P3HT:PCBM photoactive layer. The measured current-voltage (J-V) characteristics of the devices whose hole transport layers were doped with various concentrations of QDs are provided in Figure 4.5. Photocurrent has increased substantially with the doping level of QDs, which is reflected by the significant improvements in PV performance compared to the reference cell. This can be attributed to a relative swell in the current density of these devices, signifying that the incorporation of QDs in the HTL led to enhanced photon absorption by way of a quantum confinement effect that reradiates the absorbed UV range radiation to longer wavelengths. This may be coupled with improved transportation and collection of photo-generated charge carriers [15]. The surge in current density can also be

attributed to enhanced optical absorption and a wider range of absorption (see Table 4.1). The devices showed varied ranges in their performance parameters. The reference device showed a good open circuit voltage (V_{oc}) of 0.550 V but suffered from a low current density (J_{sc}) of 9.37 mAcm^{-2} which ultimately impacted its fill factor (FF) and power conversion efficiency (PCE), standing at 49.7% and 2.30%, respectively. The series and shunt resistances (R_S and R_{SH}) were derived using the J-V characteristics curve, where R_S represents the bulk and contact resistances while R_{SH} is related to charge recombination due to energy level mismatches and leakage current [30]. An organic solar cell (OSC) with ideal performance (minimal loss of output current and power) is required to have minimal series resistance (R_s) while the shunt resistance (R_{SH}) should be maximized [31, 32]. The R_S and R_{sh} values are obtained from the J-V curves. The devices with quantum dot-modified PEDOT:PSS showed a remarkable upswing in device performance across all facets. The J_{sc} increased up to 14.65 mAcm^{-2} while the series resistance and shunt resistance showed a minimum value of 412 Ω and a maximum value of 34 kΩ, respectively. The device with a 1% concentration in comparison with the

Table 4.1: The TFPSC devices' parameters with different concentrations of QDs in the hole transport layer.

Device	V_{oc} (V)	J_{sc} (mAcm^{-2})	FF (%)	PCE (%)	R_s (Ω)	R_{sh} (KΩ)
Pristine	0.550	9.37	49.72	2.30	524	10.9
1% CdTeSe	0.543	10.24	57.84	3.20	449	24.3
3% CdTeSe	0.549	11.82	54.17	3.51	417	27.8
5% CdTeSe	0.550	14.65	61.21	4.87	412	34.0
7% CdTeSe	0.549	13.24	57.10	3.97	413	20.6

reference device had a lower V_{oc} of 0.543 V, but an increase in its photo-generated current density of 10.24 mAcm^{-2} assisted in achieving a better fill factor (FF) and power conversion efficiency (PCE) of 57.84% and 3.20%, respectively. Although there was a reduced fill factor in the device with 3% QD concentration compared to the device with 1% QD concentration, the device with 3% concentration recorded higher V_{oc} and J_{sc}, which ultimately outweighed this defect and led to a better PCE. The best device performance was found at a 5% concentration of QDs in the HTL, which resulted in the best parameters (V_{oc} : 0.550 V; J_{sc} : 14.65 mAcm^{-2}; FF: 61.21%; PCE: 4.87%). Further increment in the concentration of QDs was found to be counterproductive since a noticeable decline in the performance of the device was recorded at a 7% doping level. This is attributed to large phase separation due to a high concentration of

QDs, which can produce large charge traps in the medium [33, 34, 35].

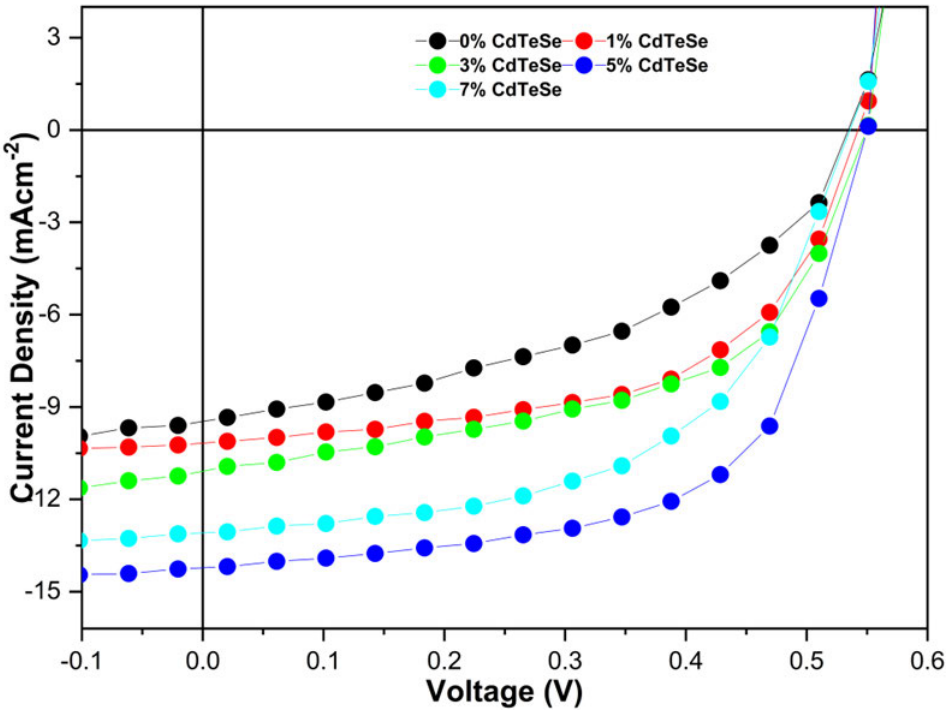

Figure 4.5: J-V Characteristics of TFPSCs with PEDOT:PSS doped with CdTeSe & PEDOT:PSS as HTL.

4.3.4 Charge carrier transport properties

Charge mobility is one of the important parameters that are used to study the charge transport properties of polymer-based solar cells. Different methods can be used to determine mobility, some of them are the time-of-flight method, carrier extraction by linearly increasing voltage (CELIV) method, photo carrier extraction by linearly increasing voltage method (PCELIV), and space charge limited current (SCLC). The charge carrier transport properties of the various devices doped with PEDOT: PSS hole transport layer was studied using SCLC. It involves the plotting of the natural logarithm of current density against voltage as shown in Figure 4.6 and revealed different charge transport mechanisms in the devices. There is an existence of a potential barrier between the electrodes under dark conditions that inhibit the free charge carriers across the junction leading to the rectification of injected carriers from the electrodes leading to current-voltage characteristics becoming quadratic ($J \propto V^2$) while the rectification can be due to Schottky effect. When a system has a large electric field without charge traps assuming there is ohmic contact between the semiconductor and electrode, the current can be

described by the Mutt-Gurney law given by equation (4.1) [36, 37, 38, 39].

$$J = \frac{\mu\varepsilon\varepsilon_0 V^2}{L^3} \tag{4.1}$$

where ϵ_0 is vacuum permittivity, ϵ is relative permittivity, L is the thickness of the active layer, and V is the applied voltage.

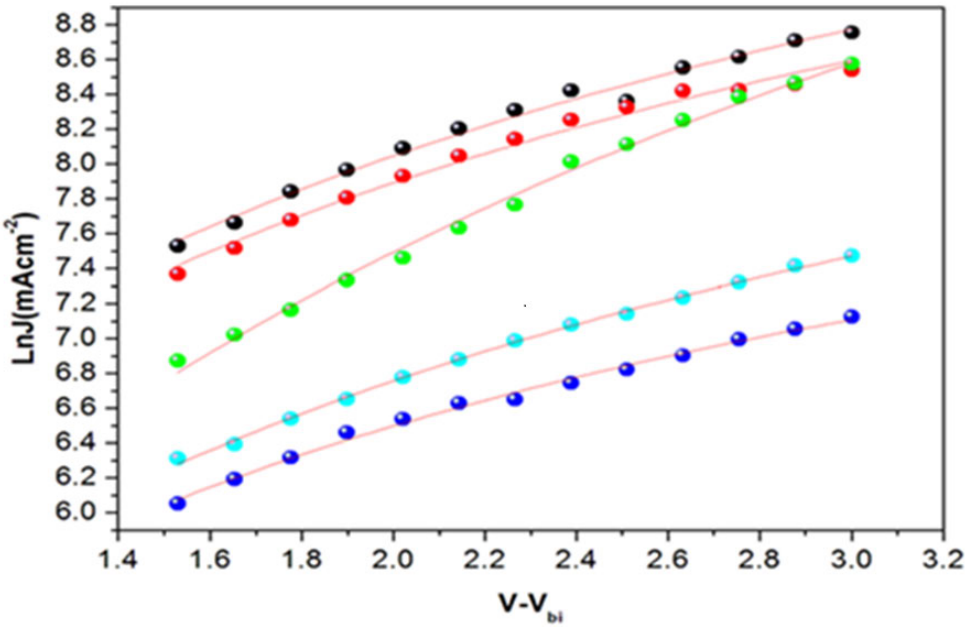

Figure 4.6: Space charge limited current of the devices with solid lines representing computer fitted lines.

Table 4.2: Thin film polymer solar cell (TFPSC) parameters for charge carriers transport.

HTL Material	μ_o (cm^2 V^{-1} S^{-1})	γ (cm V^{-1})
PEDOT:PSS 0% CdTeSe	2.0751×10^{-5}	-2.1812×10^{-4}
PEDOT:PSS : 1% CdTeSe	2.0638×10^{-3}	-2.1693×10^{-4}
PEDOT:PSS : 3% CdTeSe	1.6608×10^{-3}	-1.7457×10^{-4}
PEDOT:PSS : 5% CdTeSe	7.3524×10^{-3}	-7.7281×10^{-4}
PEDOT:PSS : 7% CdTeSe	5.4391×10^{-3}	-5.7171×10^{-4}

The J-V curve taken under dark conditions showed a typical diode characteristic at a low voltage regime in which Ohm's law holds, this is followed by a sharp current surge which indicates a quadratic relationship between voltage and current, that is, a regime that signified the fillings of all traps known as trap free regime is seen (SCLC) [36]. The incorporation of CdTeSe QD in the PEDOT:PSS could have replaced the insulating polystyrene sulphonate in PSS and

assisted in the creation of trajectory within the PEDOT chains for transportation of charges and eventual collection of holes at the anode [39] (see Table 4.2). Moreover, the difference in the work function of the buffer layer and active layer could have resulted in the observed rectification of this device since quantum sheets modified PEPOT:PSS hole extraction layer has been reported to inhibit charge recombination as well as assist hole extraction which led to an increase in PCE [40]. Also, it has been reported that engineering of HTL via incorporation of CdSe@ZnS QD into HTL with non-fullerene active blend showed better durability to 1000 minutes of UV exposure with modified HEL having a work function reduced from 4.73 eV to 4.55 eV compared to a reduction of 4.86 eV to 4.25 eV of the pristine [41]. It is inferred that interfacial engineering of HTL reduced the adverse effects on efficiency and stability of TFOSCS resulting from a gradual drop of built-in voltage during the reaction between BHJ active blend traceable to hygroscopic and acidity properties of PEDOT:PSS [42, 43]. The field activation factor and field-dependent carrier mobilities for the TFPSCs were obtained by plotting SCLC according to equation (4.2) to the obtained experimental data. The fitted data in Figure 4.6 was comparable with the experimental data obeying Mutt-Gurney law predictions of J.

$$J = \frac{9}{8}\epsilon\epsilon_0\mu_0\frac{V^2}{L^3}e^{\left(0.89\gamma\sqrt{\frac{V}{L}}\right)} \tag{4.2}$$

where μ_o is low field mobility, ϵ_0 is vacuum permittivity, ϵ is relative permittivity, L is the thickness of the active layer, V is the applied voltage, γ is the field activation factor. The zero field mobilities of QD doped in PEDOT: PSS devices were observed to be one order of magnitude higher than that of PEDOT: PSS devices. This further showed that the modification of PEDOT: PSS with QD employed in this work assisted in blocking electrons and eventually augmented the harvesting of solar energy by the devices.

4.4 Conclusions

Ternary atoms alloy quantum doped into PEDOT:PSS was used as a hole transport layer using P3HT: PCBM based solar absorber layer in the conventional device structure. The introduction of CdTeSe QD significantly contributed to the electron blocking, and charge transportation ability of HTL which eventually led to the conspicuous improvement of the PV performance of the devices. The quantum dot is believed to have replaced the chains of poly-styrene-sulfonate PSS in the polymer thereby preventing inefficient random hopping among discrete particles but creating a pathway for charge carrier transport. The presence of QD in the HTL also enabled a good ohmic contact at the anode-photoactive layer interface inhibiting charge carrier recombination. These attributes are believed to have outweighed the ability of inorganic QD to

adequately phase separate with organic polymer to form bicontinuous morphology. The device with 5% concentration by vol. of QD produced the highest efficiency which is an increase of 111.7% in comparison to the reference cell.

Acknowledgements

The listed authors are grateful to the National Research Foundation (NRF), South Africa (Grant Numbers: 113835, 85589, and 93562), and the University of KwaZulu-Natal for supporting this research work.

References

[1] Vohra, V., Matsunaga, Y., Takada, T., Kiyokawa, A., Barba, L. & Porzio, W. Impact of the electron acceptor nature on the durability and nanomorphological stability of bulk heterojunction active layers for organic solar cells. Small. **17**, 2004168 (2021)

[2] Huynh, W., Dittmer, J. & Alivisatos, A. Hybrid nanorod-polymer solar cells, science 295. (2002)

[3] Gur, I., Fromer, N., Geier, M. & Alivisatos, A. Air-stable all-inorganic nanocrystal solar cells processed from solution. Science. **310**, 462-465 (2005)

[4] Ghosekar, I. & Patil, G. Review on performance analysis of p3ht: Pcbm-based bulk heterojunction organic solar cells. Semiconductor Science And Technology. **36**, 045005 (2021)

[5] Ram, K., Mehdizadeh-Rad, H., Ompong, D., Setsoafia, D. & Singh, J. Characterising exciton generation in bulk-heterojunction organic solar cells. S Note: MDPI Stays Neutral With Regard To Jurisdictional Clai-ms In. **11** pp. 209, (2021)

[6] Xu, X., Yu, L., Meng, H., Dai, L., Yan, H., Li, R. & Peng, Q. Polymer solar cells with 18.74% efficiency: From bulk heterojunction to interdigitated bulk heterojunction. Advanced Functional Materials. **32**, 2108797 (2022)

[7] Yang, X., Qiao, J., Chen, Z., Wen, Z., Yin, H. & Hao, X. Cdse quantum dot organic solar cells with improved photovoltaic performance. Journal Of Physics D: Applied Physics. **54**, 115504 (2021)

[8] Duan, L., Hu, L., Guan, X., Lin, C., Chu, D., Huang, S., Liu, X., Yuan, J. & Wu, T. Quantum dots for photovoltaics: A tale of two materials. Advanced Energy Materials. **11**, 2100354 (2021)

[9] Zhao, N., Osedach, T., Chang, L., Geyer, S., Wanger, D., Binda, M., Arango, A., Bawendi, M. & Bulovic, V. Colloidal pbs quantum dot solar cells with high fill factor. ACS Nano. **4**, 3743-3752 (2010)

[10] Satoh, N., Otsuka, M., Ohki, T., Ohi, A., Sakurai, Y., Yamashita, Y. & Mori, T. Organic Π-type thermoelectric module supported by photolithographic mold: A working hypothesis of sticky thermoelectric materials. Science and Technology Of Advanced Materials. **19**, 517-525 (2018)

[11] Li, S., Tu, K., Lin, C., Chen, C. & Chhowalla, M. Solution-processable graphene oxide as an efficient hole transport layer in polymer solar cells. ACS Nano. **4** pp. 3169-3174, (2010)

[12] Ye, S., Sun, W., Li, Y., Yan, W., Peng, H., Bian, Z., Liu, Z. & Huang, C. Cuscn-based inverted planar perovskite solar cell with an average pce of 15.6%. Nano Letters. **15**, 3723-3728 (2015)

[13] Labban, A., Chen, H., Kirkus, M., Barbe, J., Gobbo, S., Neophytou, M., McCulloch, I. & Eid, J. Improved efficiency in inverted perovskite solar cells employing a novel diarylamino-substituted molecule as PEDOT: PSS replacement. Advanced Energy Materials. **6**, 1502101 (2016)

[14] Hamed, M., Oseni, S., Kumar, A., Sharma, G. & Mola, G. Nickel sulphide nano-composite assisted hole transport in thin film polymer solar cells. Solar Energy. **195** pp. 310-317 (2020)

[15] Amollo, T., Mola, G. & Nyamori, V. Polymer solar cells with reduced graphene oxide–germanium quantum dots nanocomposite in the hole transport layer. Journal of Materials Science: Materials In Electronics. **29** pp. 7820-7831 (2018)

[16] Soltani, R., Katbab, A., Schaumberger, K., Gasparini, N., Brabec, C., Rechberger, S., Spiecker, E., Alabau, A., Ruland, A. & Saha, A. Light harvesting enhancement upon incorporating alloy structured $CdSe_xTe_{1-x}$ quantum dots in dpp: Pc 61 bm bulk heterojunction solar cells. Journal of Materials Chemistry C. **5**, 654-662 (2017)

[17] Luther, J., Law, M., Beard, M., Song, Q., Reese, M., Ellingson, R. & Nozik, A. Schottky solar cells based on colloidal nanocrystal films. Nano Letters. **8**, 3488-3492 (2008)

[18] Law, M., Beard, M., Choi, S., Luther, J., Hanna, M. & Nozik, A. Determining the internal quantum efficiency of pbse nanocrystal solar cells with the aid of an optical model. Nano

Letters. **8**, 3904-3910 (2008)

[19] Koleilat, G., Levina, L., Shukla, H., Myrskog, S., Hinds, S., Pattantyus-Abraham, A. & Sargent, E. Efficient, stable infrared photovoltaics based on solution-cast colloidal quantum dots. ACS Nano. **2**, 833-840 (2008)

[20] Kongkanand, A., Tvrdy, K., Takechi, K., Kuno, M. & Kamat, P. Quantum dot solar cells. Tuning photoresponse through size and shape control of CdSe–TiO_2 architecture. Journal of The American Chemical Society. **130**, 4007-4015 (2008)

[21] Lee, H., Yum, J., Leventis, H., Zakeeruddin, S., Haque, S., Chen, P., Seok, S., Grätzel, M. & Nazeeruddin, M. Cdse quantum dot-sensitised solar cells exceeding efficiency 1% at full-sun intensity. The Journal of Physical Chemistry. **112**, 11600-11608 (2008)

[22] Shen, Q., Kobayashi, J., Diguna, L. & Toyoda, T. Effect of zns coating on the photovoltaic properties of cdse quantum dot-sensitised solar cells. Journal of Applied Physics. **103**, 084304 (2008)

[23] Ginger, D. & Greenham, N. Photoinduced electron transfer from conjugated polymers to cdse nanocrystals. Physical Review B. **59**, 10622 (1999)

[24] Zhang, J., Coombs, N., Kumacheva, E., Lin, Y. & Sargent, E. A new approach to hybrid polymer–metal and polymer–semiconductor particles. Advanced Materials. **14**, 1756-1759 (2002)

[25] Bartholomew, G. & Heeger, A. Infiltration of regioregular poly [2, 2-(3-hexylthiopene)] into random nanocrystalline tio2 networks. Advanced Functional Materials. **15**, 677-682 (2005)

[26] Liu, X., Ma, Z., Xing, J. & Liu, H. Preparation and characterisation of amino–silane modified superparamagnetic silica nanospheres. Journal Of Magnetism And Magnetic Materials. **270**, 1-6 (2004)

[27] Zhiya, M., Xianqiao, L. & Yueping, G. Synthesis of magnetic silica nanospheres with metal ligands and application in affinity separation of proteins. Colloids And Surfaces A. pp. 1-3 (2006)

[28] Wang, F., Tan, Z. & Li, Y. Solution-processable metal oxides/chelates as electrode buffer layers for efficient and stable polymer solar cells. Energy & Environmental Science. **8**, 1059-1091 (2015)

[29] Tauc, J. Amorphous and liquid semiconductors. (Springer Science & Business Media,2012)

[30] Lee, J., Kwon, B., Park, H., Kim, H., Kim, M., Park, J., Kim, E., Yoo, S., Jeon, D. & Kim, S. Exciton dissociation and charge-transport enhancement in organic solar cells with quantum-dot/n-doped cnt hybrid nanomaterials. Advanced Materials. **25**, 2011-2017 (2013)

[31] Pagliaro, M., Ciriminna, R. & Palmisano, G. Flexible solar cells. ChemSusChem:Chemistry & Sustainability Energy & Materials. **1**, 880-891 (2008)

[32] Yoo, S., Domercq, B. & Kippelen, B. Intensity-dependent equivalent circuit parameters of organic solar cells based on pentacene and c 60. Journal Of Applied Physics. **97**, 103706 (2005)

[33] Xia, Y., Nguyen, T., Yang, M., Lee, B., Santos, A., Podsiadlo, P., Tang, Z., Glotzer, S. & Kotov, N. Self-assembly of self-limiting monodisperse supraparticles from polydisperse nanoparticles. Nature Nanotechnology. **6**, 580-587 (2011)

[34] Coe-Sullivan, S., Steckel, J., Woo, W., Bawendi, M. & Bulović, V. Large-area ordered quantum-dot monolayers via phase separation during spin-casting. Advanced Functional Materials. **15**, 1117-1124 (2005)

[35] Kim, L., Anikeeva, P., Coe-Sullivan, S., Steckel, J., Bawendi, M. & Bulovic, V. Contact printing of quantum dot light-emitting devices. Nano Letters. **8**, 4513-4517 (2008)

[36] Taylor, D. Space charges and traps in polymer electronics. IEEE Transactions on Dielectrics and Electrical Insulation. **13**, 1063-1073 (2006)

[37] Lei, H., Fang, G., Cheng, F., Ke, W., Qin, P., Song, Z., Zheng, Q., Fan, X., Huang, H. & Zhao, X. Enhanced efficiency in organic solar cells via in situ fabricated p-type copper sulfide as the hole transporting layer. Solar Energy Materials And Solar Cells. **128** pp. 77-84 (2014)

[38] Nardes, A., Kemerink, M., Kok, M., Vinken, E., Maturova, K. & Janssen, R. Conductivity, work function, and environmental stability of pedot: Pss thin films treated with sorbitol. Organic Electronics. **9**, 727-734 (2008)

[39] Amollo, T., Mola, G. & Nyamori, V. Reduced graphene oxide-germanium quantum dot nanocomposite: Electronic, optical and magnetic properties. Nanotechnology. **28**, 495703 (2017)

[40] Zhou, P., Lan, W., Gu, J., Zhao, M., Wang, Z., Liao, Y., Liu, Y., Pu, H., Ding, J. & Wei, B. High-efficiency organic photovoltaic cells with an antimony quantum sheet modified hole extraction layer. IEEE Journal Of Photovoltaics. **11**, 111-117 (2020)

[41] Lan, W., Gu, J., Gao, X., Gong, C., Liu, Y., Zhang, W., Sun, Y., Yue, T., Wei, B. & Zhu, F. Efficient and ultraviolet-durable nonfullerene organic solar cells: From interfacial passivation and microstructural modification perspectives. Advanced Materials Interfaces. **9**, 2101894 (2022)

[42] Savva, A., Georgiou, E., Papazoglou, G., Chrusou, A., Kapnisis, K. & Choulis, S. Photovoltaic analysis of the effects of pedot: Pss-additives hole selective contacts on the efficiency and lifetime performance of inverted organic solar cells. Solar Energy Materials And Solar Cells. **132** pp. 507-514 (2015)

[43] Wang, M., Sun, Y., Guo, J., Li, Z., Liu, C. & Guo, W. Alkali metal salts doped zno interfacial layers facilitate charge transport for organic solar cells. Organic Electronics. **74** pp. 258-264 (2019)

CHAPTER 5

SEMICONDUCTOR QUANTUM DOTS AS A MECHANISM TO ENHANCE CHARGE TRANSFER PROCESSES IN POLYMER SOLAR CELLS

Chemosphere 345 (2023) 140453

Contents lists available at ScienceDirect

Chemosphere

journal homepage: www.elsevier.com/locate/chemosphere

Semiconductor quantum dots as a mechanism to enhance charge transfer processes in polymer solar cells

Abiodun Kazeem Ogundele, Genene Tessema Mola *

School of Chemistry & Physics, University of KwaZulu-Natal, Pietermaritzburg Campus, Private Bag X01, Scottsville, 3209, South Africa

HIGHLIGHTS

- Charge multiplication using ZnS quantum dot is a successful mechanism for improved device performance.
- ZnS Quantum dot exhibited a high degree of charge transfer processes and mitigate charge recombination.
- ZnS quantum dots assisted charge transport and enhanced photocurrent in polymer solar.

GRAPHICAL ABSTRACT

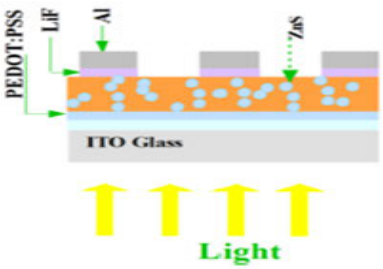

ARTICLE INFO

Handling Editor: Neppolian Bernaurdshaw

Keywords:
Modified active layer
Quantum size effect
Tandem cell
Carrier multiplication

ABSTRACT

The light trapping capability of thin film polymer solar absorber, composed of poly (3-hexylthiophene) and [6,6]–phenyl C61- butyric acid methyl ester (P3HT:PC60BM) blend, is improved using ZnS semiconductor quantum dots (QD) as third donor-acceptor (D:A) component. The inherent characteristics of the microwave-assisted synthesized ZnS QD, such as quantum size effect, and multiple exciton generation were leveraged in harvesting high energy photons, which resulted in a better exciton generation, dissociation, and effective charge transport in the polymer medium. The synthesized QD exhibited good phase purity, effective kinetic enhancement, and control of the aggregation process. Hence, the impact of ZnS QD on the performance of thin film polymer solar cells (TFPSC) is evident by a remarkable improvement in the measured photovoltaic parameters. Nonetheless, it is observed that the device performances are generally dependent on the concentration of the QD in the absorber layer. Consequently, the power conversion efficiency has increased by 58% at 3% concentration of QDs by weight. This is an interesting development of TFPSC fabricated under an ambient environment.

Abstract

The inherent characteristics of the microwave-assisted synthesised ZnS QD, such as quantum size effect, and multiple exciton generation were leveraged in harvesting high-energy photons,

which resulted in better exciton generation, dissociation, and effective charge transport in the polymer medium. The synthesised QD exhibited good phase purity, effective kinetic enhancement, and control of the aggregation process. Hence, the impact of ZnS QD on the performance of thin film polymer solar cells (TFPSC) is evident by a remarkable improvement in the measured photovoltaic parameters. Nonetheless, it is observed that the device performances are generally dependent on the concentration of the QD in the absorber layer. Consequently, the power conversion efficiency has increased by 58% at a 3% concentration of QDs by weight. This is an interesting development of TFPSC fabricated under an ambient environment.

5.1 Introduction

Semiconductor quantum dots are nanostructured crystalline materials that have sizes ranging from 2 nm to 10 nm, which is equivalent to 10 to 50 atomic lengths [1]. QDs are often referred to as zero-dimensional systems that can confine charge carriers in three dimensions resulting in the formation of new energy levels. Such inherent discrete states of nanostructured materials and unique characteristics make them different from bulk semiconductors. As a result, QDs have created new opportunities for various applications such as optoelectronics, solar energy conversion, bio-medicals etc. [2, 3, 4, 5]. Their small size gives them a high surface-to-volume ratio with properties intermediate between individual molecules and bulk semiconductors. Therefore, the electronic energy band gaps of the QDs are strongly dependent on their sizes which significantly influence the QDs' optoelectronic properties. Consequently, the electronic and optical properties of semiconductor quantum dots can be fine-tuned in such a way as to be able to produce emissions of a wide range of radiation wavelengths. The small QD produces blue light emission, while the large size gives off red light emission. On the other hand, QDs are known for multiple charge generations through various channels of energy transfer processes. Charge carrier multiplication (CM) is a phenomenon that occurs in QDs, when the energy of an absorbed photon that is greater than that of the bandgap, is used to create more than one pair of excitons (see Figure 5.1). Such novel properties of the QDs are employed for various applications including harvesting photons in solar energy conversions [6, 7, 8, 9]. The application of ZnS QD could initiate a down-conversion or up-conversion mechanism. Down-conversion is a process that involves the capturing of high-energy ultraviolet photons and their conversion into lower-energy near-infrared or medium visible photons [10, 11] while the up-conversion mechanism occurs from materials that exhibit anti-stokes photoluminescence producing emitted photons with higher energy than the incident photons [12]. Both processes have been reported to lead

to multiple exciton generation, and thus, ZnS QD has been reported to exhibit both types of conversion mechanisms [12, 13, 14, 15]. Semiconductor quantum dots can be prepared from the combination of elements of groups II-VI, III-V, IV-VI, or alloys, using various synthesis routes. Recently, our research group reported that the incorporation of a ternary alloy of Cadmium Telluride Selenide (CdTeSe) quantum dots, as a hole transport layer in the fullerene-based solar absorber, has produced a remarkable increase in device performance with a power conversion efficiency growth of up to 110% [16]. Likewise, the introduction of semiconductor quantum dots into the buffer and photoactive layers of non-fullerene-based thin film polymer solar cells has resulted in enhanced device parameters and stability [D17, D18, D19, D20]. Notably, group II-VI semiconductor QDs, such as CdSe and CdSe@ZnS, have been utilized in both active and buffer layers of fullerene and non-fullerene-based TFPSCs, respectively, to achieve improved performance [20, 21]. In this study, zinc sulphide (II-VI) semiconductor QDs are employed in polymers blend solar absorber (P3HT:PCBM) to investigate the photons capture process in the medium. Zinc sulphide quantum dot has unique properties and is commonly used in optical and photoluminescent applications, such as lasers, sensors, photodiodes, light emitting diodes, and thin film solar cells [22, 23, 24, 25]. ZnS exists in two crystallographic structures, H-ZnS and C-ZnS, with coordination numbers of twelve and eight, respectively. The method of synthesis of ZnS QDs can significantly affect their physical and chemical properties [26]. Previous studies have shown that microwave irradiation synthesis produces small inorganic

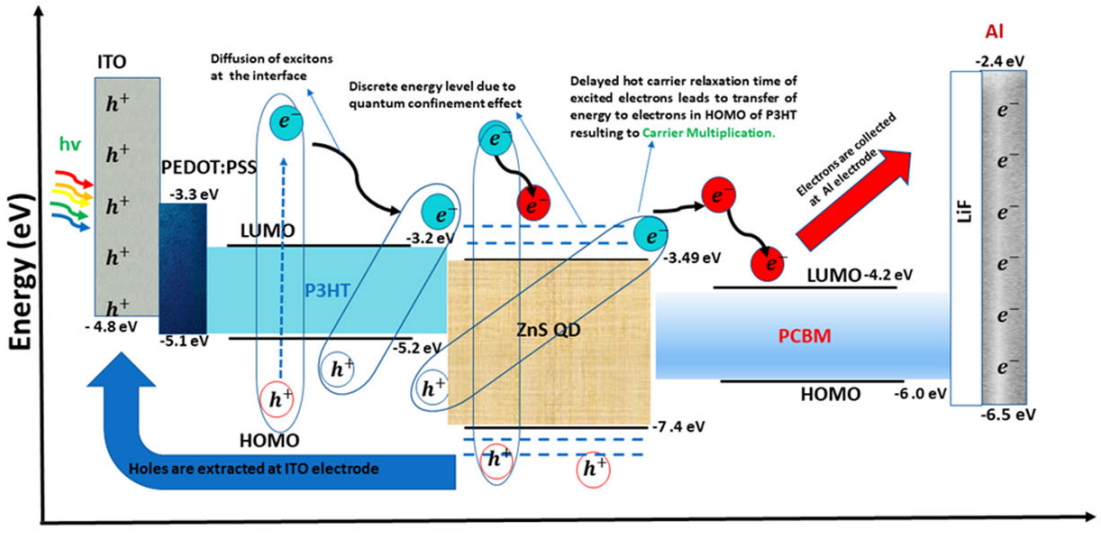

Figure 5.1: Schematic representation of electron transport energy cascade in ZnS QD doped P3HT:PCBM blend solar absorber.

particles with a narrow size distribution and high purity [27]. Microwave irradiation also offers benefits such as rapid reaction time, volumetric heating, and ease of synthesis, making it an

environmentally friendly method [28]. The incorporation of ZnS QD into the photo-active layer of the P3HT:PCBM blend is expected to improve the optical absorption at low wavelengths, enhance charge separation and reduce carriers' recombination, and promote carriers' multiplication. The optical absorption band of the P3HT molecule covers the visible and near-infrared region while PCBM absorbs mainly from UV regions of the solar spectrum. Thus, the ZnS QDs in the polymer blend, however, assist in broadening the absorption spectrum in the blue region making the modified photoactive layer absorbs low wavelength and high-energy photons, which could not have been possible with only P3HT: PCBM blends [29, 30]. Such absorption of low wavelength photons resulted in generating high energetic electrons in ZnS, which cools down through multiple channels (see Figure 5.1). For example, QDs exhibited multiple electron generation (MEG) because of the quantum confinement effect as the result of QDs discrete energy levels. These energy levels are used to delay the hot carriers cooling time, and as such instead of emitting light, it generates phonons into the valence band of the donor molecule (P3HT) to excite other excitons in the medium [31, 32]. Owing to the confinement effect of ZnS QD, this process creates more lattice vibrations of the excited electrons in the excited state because of the delayed relaxation time. Thus, the excited electrons inducing further excitons cumulated into generations of multiple excitons (see Figure 5.1). Alternately, the hot electrons get relaxed into one of the lower energy levels of the ZnS QDS conduction band by emitting light that can be captured by low energy band molecules like P3HT in the solar absorber and generate another exciton [33, 34]. These are inherent features of quantum dots which make them different from bulk semiconductor materials. In fact, they can be carefully tuned to different sizes depending on the wavelength's ranges for different applications.

5.2 Experimental approach

5.2.1 Material resources

The transparent conduction oxide (TCO) used in this study is indium tin oxide substrates (with 99.8% purity) that were procured from Sigma-Aldrich Limited and Ossila Limited. The necessary chemicals, such as zinc acetate, thioacetamide, poly (3, 4 ethylene di-oxy-thiophene): poly-styrene-sulphonate (PEDOT:PSS), poly 3-hexylthiophene (P3HT), and (6,6)-phenyl-C61-butyric acid methyl ester (PCBM), with a purity of 97%, were purchased from Ossila Company Ltd. in the United Kingdom.

5.2.2 Synthesis of ZnS quantum dots

The synthesis of the zinc sulphide QD followed a method described in references [26, 35]. Initially, 1.2 g (0.055 M) of zinc acetate was dissolved in 100 mL of deionized water, followed by the addition of 0.4103 g (0.055 M) of thioacetamide and 4 mL of thioglycolic acid to stabilize and achieve controlled size. The mixture was stirred at 500 rpm for 25 min under ambient conditions. Next, the solution was transferred to a microwave oven (700 W) and irradiated at 540 W for 20 min. During the irradiation process, thioacetamide (TAA) was hydrolysed (stage A in Figure 5.2b) to produce an intermediate and hydrogen sulphide (H_2S) (stage B in Figure 5.2b). As the irradiation continued, the intermediate lost water (stage C in Figure 5.2b) and generated $Zn(CH_3COO)_2$, which reacted with hydrogen sulphide to produce a white precipitate of zinc sulphide QD (stage D in Figure 5.2b). The resulting ZnS QD was allowed to cool to room temperature, followed by centrifugation for 20 min at 5000 rpm and repeated washing with ethanol and deionized water to remove impurities. Finally, the ZnS QD sample was dried in a vacuum for 10 h at 70 °C and stored in the dark for further characterisation.

5.2.3 Device fabrication

The TCO substrate utilized in the device fabrication is an un-patterned indium tin oxide glass substrate with a sheet resistance of 15 $\Omega{\cdot}cm^{-2}$. The ITO glass substrates were etched by partially covering the surface with a photoresist material, followed by vertically immersing the part to be etched in a warm acidic solution that is free of bubbles to maintain a perfectly straight line across the face of the ITO. The acidic solution contains hydrochloric acid (HCl), nitric acid (HNO_3), and water (H_2O) in a ratio of 48%:4%:48% by volume. The etched substrates were first thoroughly cleaned with running water and then ultrasonicated with detergent and distilled water for 20 min. The cleaning process continued by using a cotton ball to wipe with acetone. The substrates were then transferred into a plastic substrate holder and immersed fully in a container of deionized water, acetone, and isopropanol sequentially for 10 min each in an ultrasonic bath. The substrates were then allowed to dry in a nitrogen environment and later baked in an oven at 120 °C for 20 min under ambient conditions. The active blend of poly(3-hexylthiophene):(6,6)-phenyl-C_{61}-butyric acid methyl ester (P3HT:PCBM) was prepared by dissolving 5 mg each of P3HT donor polymer and PCBM acceptor polymer in 0.5 mL of chloroform (CF) co-solvent to obtain a reference pristine at 20 mg/mL concentration. Another three different concentrations were prepared by adding 1%, 3%, and 5% by weight of ZnS QD into the donor:acceptor blend of P3HT:PCBM. All four concentrations were stirred for a period

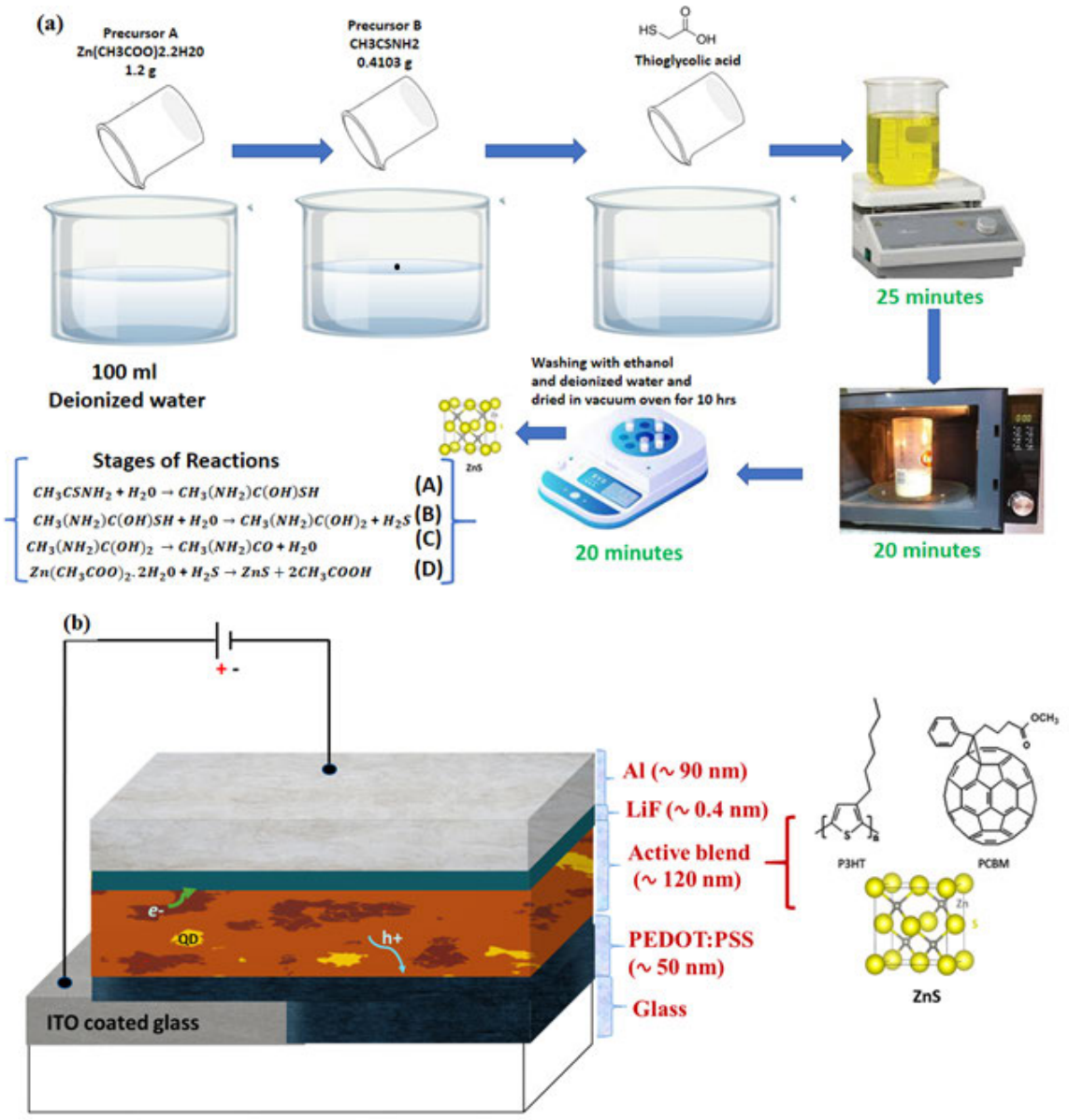

Figure 5.2: (a) Microwave assisted synthesis of zinc sulphide QD (b) Conventional device architecture of different layers including modified active layer.

of three hours at 40 °C to ensure adequate miscibility. Then, poly(3,4-ethylenedioxythiophene) polystyrene sulfonate (PEDOT:PSS) was spin-coated on the substrate at a rate of 3500 rpm for 60 s to achieve a thickness of about 40–50 nm, and annealed in the oven for 30 min at 120 °C. The reference active blend of P3HT:PCBM and modified active blends containing various concentrations of P3HT:PCBM/ZnS were spin-coated on the dried PEDOT:PSS at 1200 rpm for 40 s to obtain a thickness of 100–120 nm. The substrates were subsequently dried in the furnace for 5 minutes at 90 °C in a nitrogen atmosphere. The devices, which followed the conventional architecture as shown in Figure 5.2a, were then carefully mounted on the

mask and transferred to an Edwards Auto 306 vacuum deposition unit where a 0.4 nm thin layer of lithium fluoride (LiF) and 90 nm of aluminium (Al) top electrode were deposited on the substrates at a pressure of 10^{-6} mBar. The samples were briefly annealed for 5 min at 110 °C in a nitrogen-filled furnace, followed by electrical measurements of parameters using a computer-interfaced Keithley (HP2420) source meter under 1.5 solar simulator illuminations (model SS50AAAA) at a light intensity of 100 mW/cm^2.

5.3 Results and discussion:

5.3.1 Optical characterisation of the device

The optical absorptions of ZnS quantum dots in solvent suspension, and polymer blend solar absorber films with/without ZnS QD were studied using the UV-Vis spectrometer (see Figure 5.3). Figure 5.3c displays the UV-Vis absorption spectrum of ZnS QDs in ethanol suspension, indicating that the quantum dot absorbs at lower wavelengths until 350 nm. However, when QDs are incorporated in polymer blend films, new absorption patterns emerged compared to the reference sample (in Figure 5.3a). The absorption spectra taken from ZnS-doped films exhibited new peaks centered around 400 nm, which is likely attributed to electron band-to-band transition in ZnS. The central absorption peak near 515 nm is a typical absorption maximum of the P3HT molecule. The same peak (i.e., in devices doped with 1%, 3%, and 5% ZnS QD) appeared to have slightly blue-shifted compared to the reference cell. Generally, the absorbance measured from QD-doped samples showed broadening of the central peak, which is beneficial for increasing photon capture by the polymer solar absorber, ultimately indicating the capturing of high-energy photons which must have induced extra excitons, thereby leading to reduced energy loss. Possible changes in the energy band gap of the films due to the concentration of QDs are measured from the onset of optical absorptions as provided in Figure 5.3b. On the other hand, QD-doped solar absorber films showed enhanced optical absorptions at the central peak near 515 nm, indicating more exciton dissociations due to reduced charge recombination in the polymer medium, which complements the quenching of the photoluminescence (PL) intensity with QDs in the P3HT:PCBM blend solution (see Figure 5.3d). The PL data presented in Figure 5.3d clearly showed reduced PL intensity with increasing concentrations of QDs in the polymer blend solution, suggesting the occurrence of effective charge separation due to the presence of QDs. Similar observations have been reported in the literature; for instance, [36, 37] reported the existence of interparticle transfer between the ZnS QDs and the photoactive blends. For instance, the P3HT:PCBM blend showed an emission peak around 595

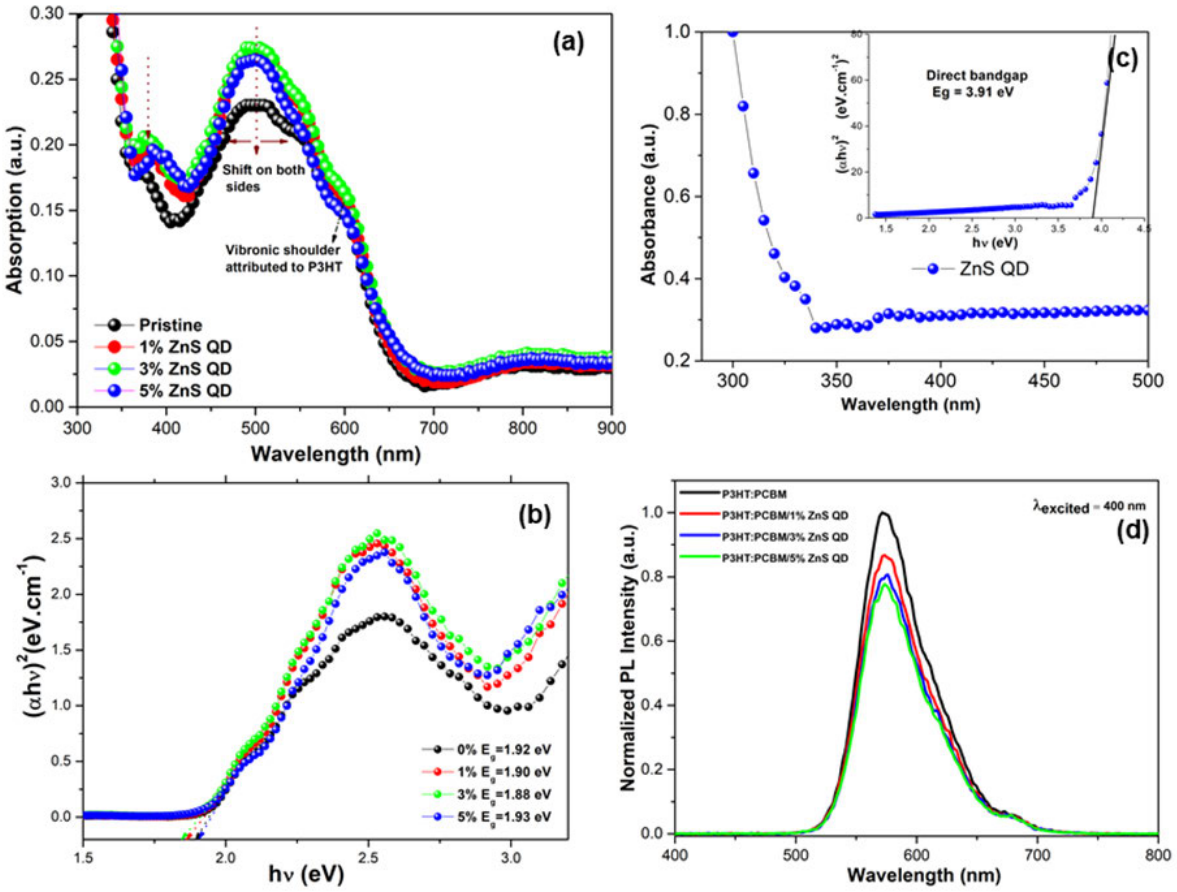

Figure 5.3: (a) Optical absorption of devices with and without QD doped into photoactive layer of P3HT:PCBM (b) Energy loss of reference device and modified active layer (c) UV-Vis absorption spectra of ZnS QD dispersed in ethanol and inset of the bandgap of ZnS QD (d) PL intensity of P3HT:PCBM/ZnS QD solution in chloroform.

nm, which noticeably decreases with increased concentration of QDs. This decrease further explained the efficient photo-induced charge transfer from the QDs to the photoactive blends, suggesting that the excited electrons decayed through non-radiative transition, indicating PL quenching in hybrid polymer solar cells as a characteristic transfer of photogenerated charges [37]. Notably, the electronic properties of the quantum dot vary significantly when its dimensions are closer to or smaller than the Bohr radius of the exciton due to the quantum confinement effect of the semiconductor. A blue shift denotes a wider energy bandgap, while a red shift indicates a narrower energy bandgap. The Beer-Lambert law expresses the relationship between the incident light on a solution and the light transmitted through it, as shown in equation (5.1) below:

$$I = I_0 e^{-\alpha l}, \tag{5.1}$$

where I_0 is the incident light intensity, I is the transmitted light intensity, α is the absorption coefficient, and l is the length of the cuvette, which is 1 cm. The absorption coefficient, α, of the liquid can be obtained from equation (5.1) above to become equation (5.2):

$$\alpha = \frac{2.303A}{l} = 2.303A, \tag{5.2}$$

where the absorbance A is given by $A = \log\left(\frac{I_0}{I}\right)$. Tauc's equation (equation 5.3) shown below was used to calculate the optical energy bandgap of the quantum dot with the aid of the UV-Vis spectrum (see inset of Figure 5.3b):

$$(\alpha h\nu)^n = B(h\nu - E_g), \tag{5.3}$$

where $h\nu = \frac{hc}{\lambda}$ (where c is the speed of light and λ is the wavelength of light) is the photon energy, α is the absorption coefficient, A is a proportionality constant depending on the material (it is used as 1 for amorphous material), and n is either 0.5 for indirect allowed transition or 2 for direct allowed transition. Here, n is taken as 2 since ZnS is known to be a direct bandgap semiconductor, as shown in the inset of Figure 5.3c. The graph of $(\alpha h\nu)^n$ against $h\nu$, where $(\alpha h\nu)^n = 0$, gives the energy gap (E_g). According to the information given in Figure 5.3c, the band gap of ZnS is 3.91 eV. Furthermore, it has been reported that the size effect on energy band gap alteration of the semiconductor quantum dot can be quantified [26], by the Brus effective mass approximation model [38] which relates the effective band gap of a quantum dot to the size of the nanoparticle (NP), using the following equations (5.4) and (5.5):

$$E_{\mathrm{QD}} = E_{\mathrm{BG}} + \frac{h^2}{8R^2}\left(\frac{1}{m_e^*} + \frac{1}{m_h^*}\right) - \frac{1.8e^2}{4\pi\epsilon R}, \tag{5.4}$$

$$a_{\mathrm{exc}} = m_0\epsilon\left(\frac{1}{m_e^*} + \frac{1}{m_h^*}\right)a_0, \tag{5.5}$$

where h is Planck's constant, ϵ is the bulk optical dielectric constant (8.76), E_{BG} is the bulk bandgap, the second term of equation (5.4) represents the confinement energy ($E_{\mathrm{confinement}}$), the third term represents the exciton energy (E_{exciton}), a_0 is the Bohr radius, m_e^* and m_h^* are the effective masses of the electron and hole, respectively, and m_0 is the rest mass of a free electron. For ZnS, $m_e^* = 0.42m_0$ and $m_h^* = 0.61m_0$. The particle size of the quantum dot (QD) is 2.01 nm, calculated using the energy gap obtained from the UV-Vis spectrum for ZnS QD (see equation 5.4), with the confinement energy being 0.39 eV (see Equation 5.4), and the exciton radius is 1.87 nm (equation 5.5). This indicates that the optical bandgap increases with a decreasing ZnS QD size due to the size confinement effect [39]. The size of QDs determined from XRD data is 2.70 nm, which is within the expected range and consistent with TEM images.

This underscores the range of absorption of quantum dots that can be easily tuned due to the size confinement effect [40]. Since the limited optical absorption of P3HT:PCBM is traceable to its small spectral overlap, ultimately leading to incomplete utilisation of high-energy photons and consequently limiting the power conversion efficiency, the incorporation of QDs which have tunable energy bandgaps into the photoactive layer is expected to broaden the absorption spectrum of the solar absorber layer, especially if the QD sizes vary between 2 nm and 9 nm. This is evident from the enhanced intensity of optical absorbencies of the solar absorber films with an optimum concentration of QDs. However, an excess concentration of QDs in a polymer blend matrix could result in the formation of unfavorable defects in the medium, promoting charge recombination and reducing absorption intensities [41, 42, 43]. Owing to the multifaceted roles of QDs from their interaction with electromagnetic radiation, they could impact device performance by creating extra charge carriers that enhance the conductivity of the absorber medium and improve photocurrent collection. Moreover, the interaction of ZnS QDs with polymer blends could lead to alterations in energy level mismatches, consequently reducing energy loss during charge transfer. Overall, there was a notable widening of the absorption range (380–680 nm) of the modified photoactive films, as shown in Figure 5.3a, which is attributed to the tunability of the energy levels of donor and acceptor polymers [44]. The device with 3 wt% ZnS quantum dot concentration recorded the broadest absorption spectrum and highest intensity, resulting in the best device performance.

5.3.2 Characterisation of ZnS QD

Fourier Transform Infrared (FTIR) spectroscopy measurements presented in Figure 5.4a provide pieces of evidence on the constituent's chemical bonds of the molecules in the QD powder. The FTIR spectra given in Figure 5.4a showed some peaks which are characteristics of ZnS as presented in the figure. Particularly, the peaks at 770.46 and 680.79 are attributed to the Zn-S vibration mode which is characteristic of cubic ZnS [45]. The X-ray diffraction crystallography revealed typical XRD patterns of the ZnS QD as shown in Figure 5.4b which carries three diffraction peaks at 28.56°, 48° and 57.8° corresponding to the reflection by crystal planes [111], [220], and [311] cubic crystal planes of ZnS QD (with JCPDS card number 0107), respectively. The conspicuous broadening noticed in the diffraction peaks in Figure 5.4b is related to small crystallite size which further underscores synthesis of the quantum dot. The fewer peak positions and sharp diffraction peaks noted in the XRD pattern are an indication of a good crystallisation of the microwave-assisted synthesised QD [46]. The crystalline size of ZnS QD

grains was determined using Scherrer's equation (5.6) below:

$$D_{hkl} = \frac{k\lambda}{\beta_{hkl} \cdot (2\theta) \cos\theta}, \tag{5.6}$$

β_{hkl} is the full-width at half maximum (FWHM) of the peak (in radians), θ is the Bragg's angle (in degrees), while k is a constant dependent on the shape of the crystal and varies from 0.62 to 2.08. Specifically, $k = 0.94$ for FWHM of a spherical crystal with cubic symmetry, and $k = 0.89$ for the integral breadth of a spherical crystal with no cubic symmetry. Table 5.1 below

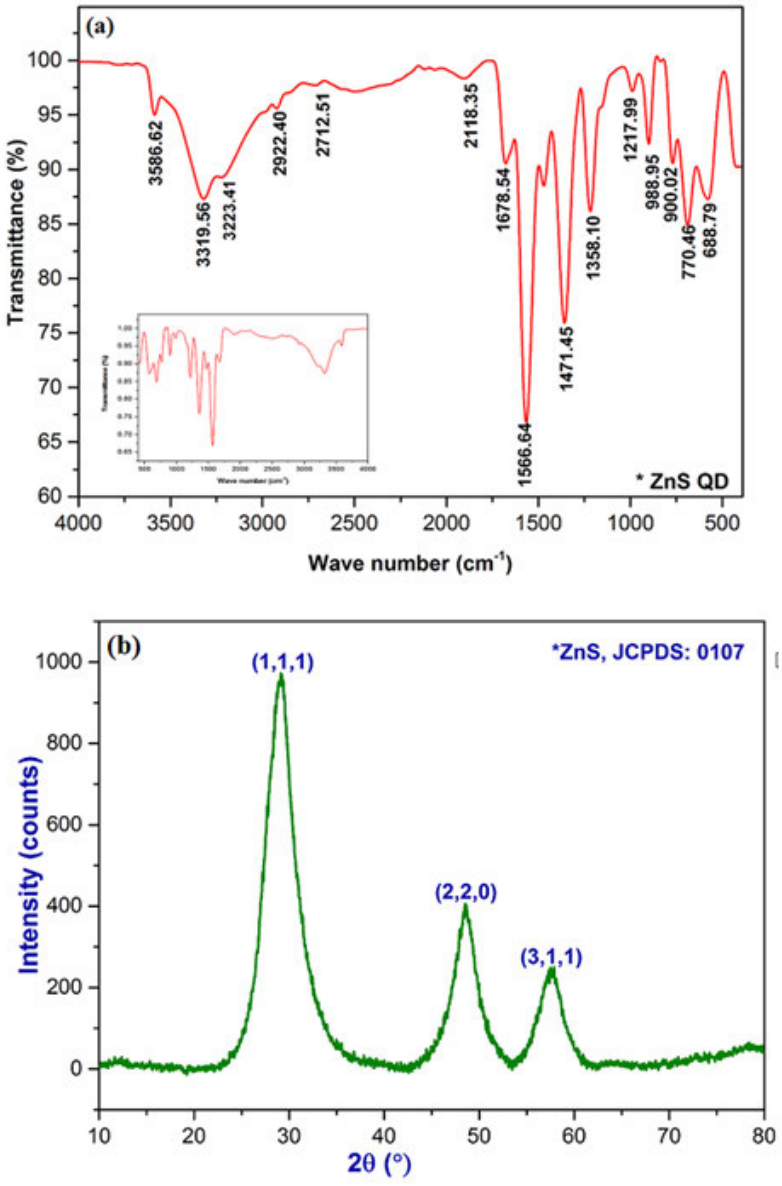

Figure 5.4: (a) FTIR spectrum of ZnS quantum dots (QDs); (b) XRD spectrum of ZnS QDs with insets showing the full width at half maximum (FWHM) values.

shows the results of the XRD data of the quantum dot. The true peak position, as well as the corresponding width of monochromatic Cu Kα radiation, was obtained by fitting the measured

peaks with two Gaussian curves (using Origin software), which led to the determination of the FWHM and peak positions for the QD. The average crystallite size of ZnS QD found from XRD data is 2.70 nm. This size effect can be attributed to the synergistic effect of thioglycolic acid, which acts as a stabilizer, and the microwave-assisted synthesis of the quantum dot.

Table 5.1: The XRD parameters for ZnS QD

Peak no	**2θ (°)**	**hkl**	**FWHM β_{hkl} (°)**	**D_{hkl} (nm)**
1	28.56	111	3.928	2.06
2	47.50	220	3.049	2.81
3	56.36	311	2.770	3.22

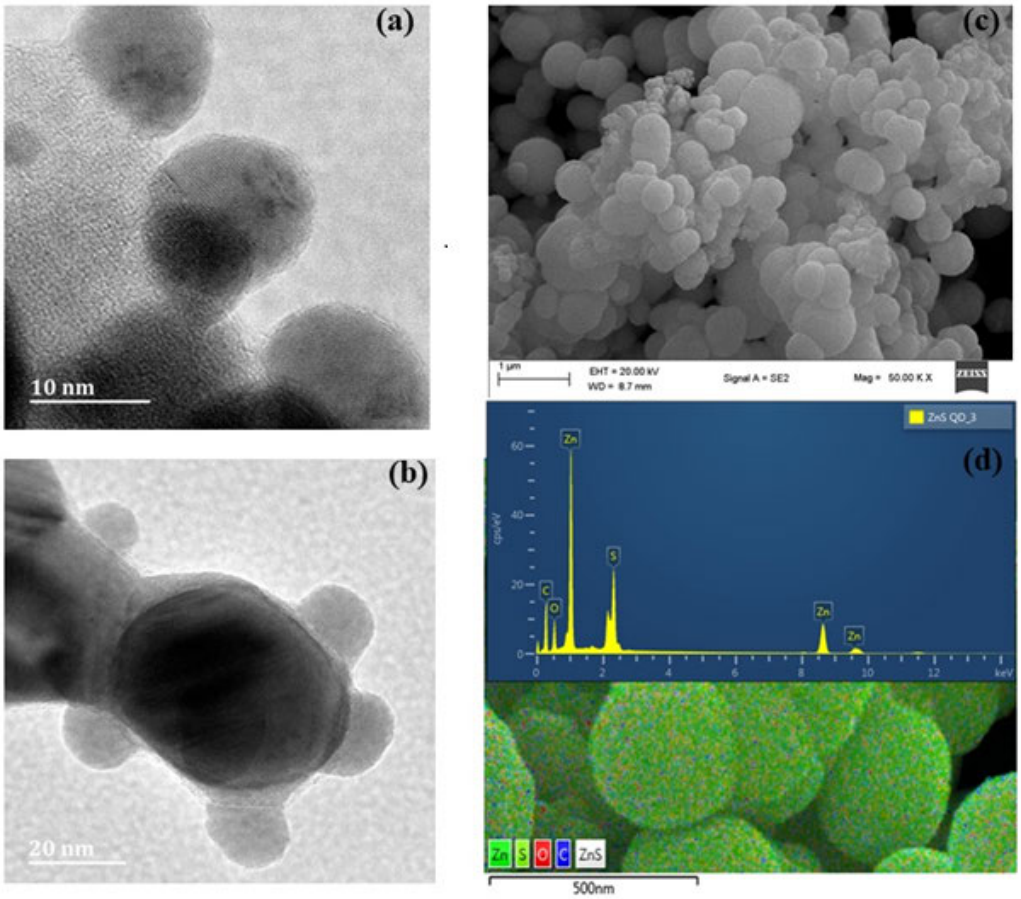

Figure 5.5: (a) & (b) Transmission electron microscopy of ZnS QD at 50 nm and 20 nm magnification sizes, (c) Scanning electron microscopy image of ZnS QD (d) Energy dispersive X-ray of ZnS QD.

Scanning electron microscopy and transmission electron microscopy were employed to study the morphological and structural characteristics of ZnS quantum dots as shown in Figure

5.5. The TEM images provided in Figure 5.5a and Figure 5.5b demonstrate the size of the quantum dots close between 2 nm and 6 nm. Some of the QDs are grown on the surface of large spherical ball-like structures as presented by SEM images in Figure 5.5c and Figure 5.5d. TEM images revealed the presence of crystal fringes with lattice spacing ranging from 0.297 nm to 0.311 nm, this can be an indication of the crystalline structure of different faces. The constituent elements of the ZnS quantum dot were indicated by energy dispersive X-ray (EDX) with an approximately equal ratio of zinc to sulphur. The elemental mapping conducted on the SEM image (Figure 5.5d) clearly shows the even distribution of Zn and S elements in the medium. The noticeably small fraction of nitrogen and oxygen can be attributed to remnants of the impurities and undue exposures during the SEM measurements while the carbon is from the scanning electron microscopy sample holder. However, the quantum dot was noticed to exhibit an uneven morphology which could be traced to different sizes of nanoparticles. The sizes of the nanoparticles as determined by Brus effective mass approximation model and XRD patterns are summarized in Table 5.1 given above. The difference in the sizes obtained from the XRD and Brus model can be attributed to the fact that while the XRD represents the gross measurements of the QD, which includes its surface layers, the Brus model gives the theoretical evaluation of the size based on the optical and electronic properties of the QDs by using idealized conditions [47].

5.3.3 J-V characteristics

The impact of the ZnS quantum dots on the performance of the polymer solar cells was investigated using the measured J-V characteristics of the solar cells as provided in Figure 5.6. The functional layers of the devices were sequentially arranged as (ITO/PEDOT:PSS/P3HT:PCBM/LiF/Al) for reference cells while QD modified photoactive layer follows (ITO/PEDOT:PSS/P3HT:PCBM/ZnS QD/LiF/Al). The ZnS QDs were used at different concentrations (1%, 3%, and 5% by weight) in the (P3HT:PCBM) blend active layer. The graph showed a noticeable surge in photocurrent with various concentrations of doping level of quantum dots into the active layers compared to the reference cell which is evident in photovoltaic (PV) parameters shown in Table 5.2. The increase in Voc with doping of QD into the active blend of P3HT:PCBM could be due to the size quantum effect of the QD, which influences their electronic and optical properties. The energy alignment of QD in active blend led to a suitable alignment of energy level [41, 48] and enhanced charged transfer by modified active layers as shown in Figure 5.6a. This can be traced to the relative surge in the current density of these and ultimately led to efficient dissociation, transportation and collection of

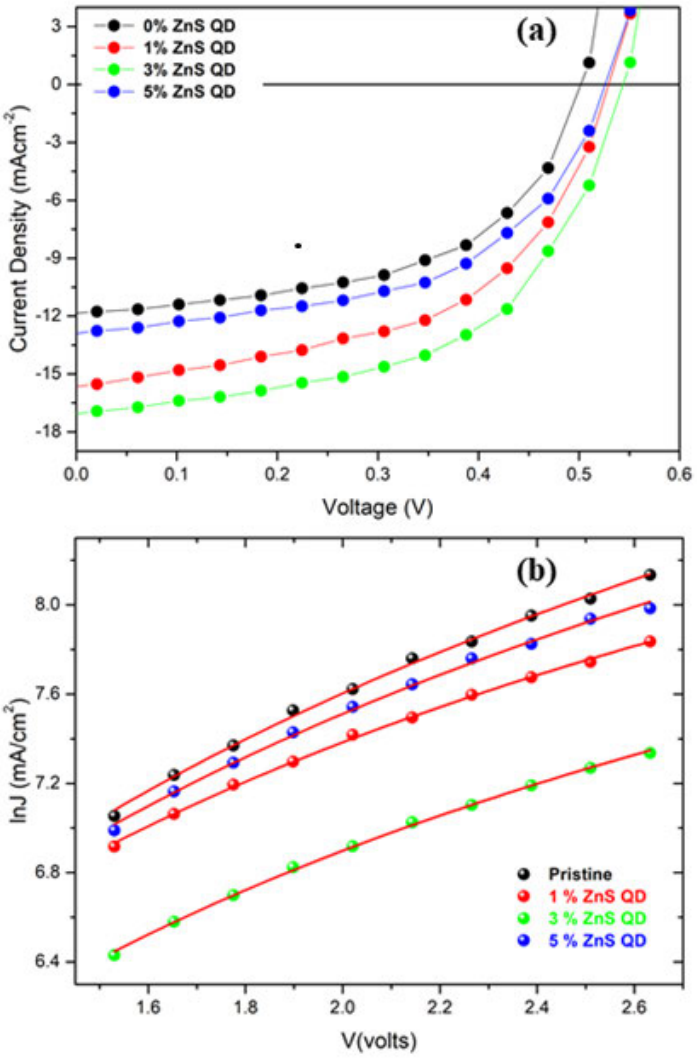

Figure 5.6: (a) J-V Characteristics of TFPSC devices of the reference cell and various concentrations of modified photoactive blend doped with ZnS QD. (b) SCLC of the PSC devices of the reference cell and various concentrations of modified photoactive blend doped with ZnS QD.

photo-generated charge carriers at the electrodes [16, 49]. The PV parameters for devices in Table 5.2 showed that the open voltage V_{oc} values range from 0.50 V to 0.54 V typical of an active blends of P3HT:PCBM with the reference device recording 0.501 V, while the QD modified active blend devices 1%, 3%, and 5% recorded 0.52 V, 0.54 V, and 0.53 V, respectively. The increase in theV_{oc} was due to the size quantum effect of QD which influences its electronic and optical properties as well as favourable energy alignment. Furthermore, Table 5.2 showed improved PV parameters compared to the pristine device, the device with a 3% doped concentration of ZnS QD produced the best device parameters after which a sharp decline was noticed at a higher concentration of 5% which could be traced to the phase separation of inorganic

Table 5.2: Polymer solar cell parameters for pristine and QD-modified photoactive devices.

P3HT:PCBM/ZnS QD	$\mathbf{E}_G$ (eV)	$\mathbf{E_{LOSS}}$ (eV)	$\mathbf{V_{oc}}$ (V)	$\mathbf{J_{sc}}$ (mAcm^{-2})	**FF** (%)	**PCE** (%)	$\mathbf{R}_s$ (Ω)	$\mathbf{R_{SH}}$ ($K\Omega$)
0%	1.92	1.419	0.501	11.84	53.55	3.17	679.1	1.24
1%	1.90	1.385	0.515	15.65	53.72	4.33	444.1	6.18
3%	1.88	1.336	0.544	17.12	53.80	5.01	228.8	6.50
5%	1.93	1.403	0.527	12.91	53.19	3.61	638.1	8.41

QD particles from organic matrix evident with poor bi-continuous morphology [50]. A further increment in the doping concentration of QD into the active blend is believed to be pointless since a conspicuous decline in the performance of the device is recorded at a 5% concentration level.

5.3.4 Charge carrier transport properties

The performance of organic semiconductors in opto-electronic and organic electronic devices relies heavily on their charge carrier transport properties, particularly their charge mobility [51]. This mobility is a direct result of the delocalisation of π-electrons within the organic semiconductor's molecular structure, which contains alternating single and multiple bonds that give rise to π-bonds [52]. Therefore, the charge carrier mobility of the transport or active layer is a critical factor in the overall performance of organic solar cells. Various techniques are available to characterize the charge transport properties of organic semiconductors, including the double injection method (DoI), impedance spectroscopy (IS), carrier extraction by linearly increasing voltage (CELIV) method, photo carrier extraction by linearly increasing voltage (PCELIV) method, time of flight (TOF) method, and space charge limited current (SCLC) method, among others. The method employed in this study is SCLC which is suitable for characterisation of charge transport by dark injection method and involves all the three layers - hole transport layer (HTL), electron transport layer (ETL), active layer (AL) of TFOSCs (thickness of (thickness of $\sim$ 200 nm–2 μm) being sandwich between two electrodes. SCLC involves one injection blocking contact and one charge injection contact. This was achieved in this study by coating indium doped tin oxide (ITO) substrate with a layer of PEDOT:PSS with a thickness of about 50 nm to improve the hole injection before subsequent application of the active layer and modified active layer [53]. According to theoretical calculation and experimental evidence the injection barrier should not exceed 0.3 eV for SCLC experiments [54, 55, 56]. Eventually, the natural logarithm of dark current density was plotted against voltage

as shown in 5.6b. The potential barrier between the electrodes under the dark conditions prevents the free charge carriers across the junction leading to rectification of injected carriers from the electrodes, resulting in the current-voltage relationship becoming quadratic ($J \propto V^2$). It has been reported that a trap-free system exists under a high electric field with an ohmic contact between the semiconductor and electrodes, the J-V relation is given by the Mott-Gurney equation 5.7 [57, 58, 59]:

$$J = \frac{\mu \epsilon \epsilon_0 V^2}{d^3}, \tag{5.7}$$

where ϵ is the relative permittivity, ϵ_o is the vacuum permittivity, d is the thickness of the active layer, and V is the voltage applied across the electrodes. At a low voltage regime, there is a linear relationship between current density and applied voltage which shows that Ohm's law holds, after which the curve is dominated by a quadratic relationship between current and voltage, evident by the filling of all traps, known as the trap-free regime [58]. Equation (5.7) can be modified to equation (5.8) [60, 61] for a material that shows field dependency on mobility.

Table 5.3: Parameters for charge carrier transport of thin film polymer solar cell devices fabricated with a modified photo-active layer.

P3HT:PCBM/ZnS QD	**Zero Field Mobility μ_0**	**Field Activation Factor**
	($\mathrm{cm^2\ V^{-1}\ s^{-1}}$)	γ ($\mathrm{cm\ V^{-1}}$)
0% (Pristine)	1.0098×10^{-4}	-4.4763×10^{-4}
1%	1.4733×10^{-4}	-6.5310×10^{-4}
3%	8.8352×10^{-4}	-3.9166×10^{-4}
5%	1.1595×10^{-4}	-5.9629×10^{-4}

$$J = \frac{9}{8}\mu \epsilon \epsilon_0 \frac{V^2}{d^3} e^{0.89\gamma\sqrt{\frac{V}{d}}}, \tag{5.8}$$

Gill proposed temperature dependency of the field activation factor using the following equation (5.9):

$$\gamma = B\left(\frac{1}{K_B T} - \frac{1}{K_B T_0}\right), \tag{5.9}$$

where K_B is the Boltzmann constant, B is $2.9\times10^{-5}\,\mathrm{eV\,m^{1/2}\,V^{-1/2}}$, and $T_o = 600\,\mathrm{K}$ [61]. It has been reported that large disordered organic semiconductors have similar values of B and T_o, with variations in other parameters showing an order of two in the description of this behavior [62].

The introduction of ZnS QD into the active layer has proven favorable since the mobility

decreases at high electric fields, evident from the negative value of the activation factor as shown in Table 5.3. It should be noted that dark current is the resultant effect of the random generation of holes and electrons within the depletion region of the device in the absence of incident photons; it could also be referred to as leakage current [63]. It has been reported that the presence of dark current in a device is traceable to the appearance of noise in the device [64, 65]. As inferred from Figure 5.6b, the device with a concentration of 3% QD by weight in the photoactive blend of P3HT:PCBM recorded the lowest dark current and thus experienced the least amount of noise, leading to its optimal device parameters as shown in Table 5.3.

5.4 Conclusions

A simple and easy microwave irradiation technique was employed in the synthesis of ZnS QD and subsequently used to dope in P3HT:PCBM blends a photoactive layer of TFPSC, fabricated in a conventional architecture. The doping of ZnS QD into the active layer proved to have a significant positive contribution in the optoelectronic properties of the polymer films and the performance of polymer solar cells by leveraging on its ability to capture high energy photons, and generation of multiple charges. These effects are evident in the broad optical absorption width of the absorber films, and consequently, resulted in enhanced growth in PCE. The ZnS QD is expected to play the role of a third donor-acceptor component in the active layer in analogous to tandem solar cells since the QDs have dual charge carriers (holes and electrons) like donor/acceptor polymers. These attributes of ZnS QD resulted in the collection of high photo-current and better device performances. The optimum concentration of ZnS QDs, for best PCE = 5.01%, was at 3% by weight, which showed PCE growth of 58% from the reference cell. However, a higher concentration of QD in the polymer matrix is found to be unfavourable to device performances due to the formation of undesirable defects in the medium. Finally, ZnS QDs are highly stable in ambient environments and suitable for roll-to-roll device fabrication.

Acknowledgements

The authors expressed profound gratitude to the National Research Foundation (NRF), South Africa (Grant Numbers: 113835, 132786), and the University of KwaZulu-Natal for supporting this research work.

References

[1] Brus, L. Growing gold nanoprisms with light. Nature Materials. **15** pp. 824-825 (2016)

[2] Wu, H., Xu, H., Shi, Y., Yuan, T., Meng, T., Zhang, Y., Xie, W., Li, X., Li, Y. & Fan, L. Recent advance in carbon dots: from properties to applications. Chinese Journal Of Chemistry. **39** pp. 1364-1388 (2021)

[3] Zhang, T., Liu, J., Zhou, F., Zhou, S., Wu, J., Chen, D., Xu, Q. & Lu, J. Polymer-coated Fe2O3 nanoparticles for photocatalytic degradation of organic materials and antibiotics in water. ACS Applied Nano Materials. **3** pp. 9200-9208 (2020)

[4] Reshmy, R., Philip, E., Paul, S., Madhavan, A., Sindhu, R., Binod, P., Pandey, A. & Sirohi, R. Nanocellulose-based products for sustainable applications-recent trends and possibilities. Reviews In Environmental Science And Bio/Technology. **19** pp. 779-806 (2020)

[5] Mansur, A., Mansur, H., Tabare, C., Paiva, A. & Capanema, N. Eco-friendly AgInS 2/ZnS quantum dot nanohybrids with tunable luminescent properties modulated by pH-sensitive biopolymer for potential solar energy harvesting applications. Journal Of Materials Science: Materials In Electronics. **30** pp. 16702-16717 (2019)

[6] Dlamini, M. & Mola, G. Near-field enhanced performance of organic photovoltaic cells. Physica B: Condensed Matter. **552** pp. 78-83 (2019)

[7] Hamed, M., Oseni, S., Kumar, A., Sharma, G. & Mola, G. Nickel sulphide nano-composite assisted hole transport in thin film polymer solar cells. Solar Energy. **195** pp. 310-317 (2020)

[8] Mola, G., Arbab, E., Taleatu, B., Kaviyarasu, K., Ahmad, I. & Maaza, M. Growth and characterisation of V2O5 thin film on conductive electrode. Journal Of Microscopy. **265** pp. 214-221 (2017)

[9] Mola, G., Mthethwa, M., Hamed, M., Adedeji, M., Mbuyise, X., Kumar, A., Sharma, G. & Zang, Y. Local surface plasmon resonance assisted energy harvesting in thin film organic solar cells. Journal Of Alloys And Compounds. **856** pp. 158172 (2021)

[10] Mallick, S., Pal, A., Kumar, A. & Sk, M. Quantum dots as photon down-conversion materials. Advances In Electronic Materials For Clean Energy Conversion And Storage Applications. **Elsevier2023** pp. 247-264

[11] Cai, Q., Sheng, W., Yang, J., Zhong, Y., Xiao, S., He, J., Tan, L. & Chen, Y. Synergistic Passivation and Down-Conversion by Imidazole-Modified Graphene Quantum Dots for High Performance and UV-Resistant Perovskite Solar Cells. Advanced Functional Materials. pp. 2304503 (2023)

[12] Zhou, J., Liu, Q., Feng, W., Sun, Y. & Li, F. Upconversion luminescent materials: advances and applications. Chemical Reviews. **115** pp. 395-465 (2015)

[13] Motmaen, A. & Rostami, A. High-efficiency integrated MIR band to visible band upconversion optoelectronic system. Journal Of Nonlinear Optical Physics & Materials. pp. 2350047 (2023)

[14] Liu, W., Zhang, Y., Ruan, C., Wang, D., Zhang, T., Feng, Y., Gao, W., Yin, J., Wang, Y. & Riley, A. ZnCuInS/ZnSe/ZnS quantum dot-based downconversion light-emitting diodes and their thermal effect. Journal Of Nanomaterials. **16** pp. 354-354 (2016)

[15] Fontenot, R., Mathur, V., Barkyoumb, J., Mungan, C. & Tran, T. Measuring the anti-Stokes luminescence of CdSe/ZnS quantum dots for laser cooling applications, Tri-Technology Device Refrigeration (TTDR. SPIE. pp. 982103 (2016)

[16] Ogundele, A. & Mola, G. Ternary atoms alloy quantum dot assisted hole transport in thin film polymer solar cells. Journal Of Physics And Chemistry Of Solids. pp. 110999 (2022)

[17] Lin, X., Wang, Y., Wu, J., Tang, Z., Lin, W., Nian, L. & Yi, G. Black phosphorus quantum dots based heterostucture boosting electron extraction for non-fullerene organic solar cells surpassing 15

[18] Oseni, S., Osifeko, O., Boyo, A. & Mola, G. Tri-metallic quantum dot under the influence of solvent additive for improved performance of polymer solar cells. Journal Of Applied Polymer Science. **140** pp. 53293 (2023)

[19] Li, R., Tang, L., Zhao, Q., Teng, K. & Lau, S. Facile synthesis of ZnS quantum dots at

room temperature for ultra-violet photodetector applications. Chemical Physics Letters. **742** pp. 137127 (2020)

[20] Lan, W., Gu, J., Gao, X., Gong, C., Liu, Y., Zhang, W., Sun, Y., Yue, T., Wei, B. & Zhu, F. Efficient and Ultraviolet-Durable Nonfullerene Organic Solar Cells: From Interfacial Passivation and Microstructural Modification Perspectives. Advanced Materials Interfaces. **9** pp. 2101894 (2022)

[21] Li, Z., Song, D., Xu, Z., Qiao, B., Zhao, S., Wageh, S., Al-Ghamdi, A. & Huo, X. Improved UV sensitivity and charge transport in PTB7-Th: PC 71 BM solar cells doped with cadmium selenide quantum dots. Sustainable Energy & Fuels. **6** pp. 2053-2061 (2022)

[22] Tang, W. & Cameron, D. Electroluminescent zinc sulphide devices produced by sol-gel processing. Thin Solid Films. **280** pp. 221-226 (1996)

[23] Jin, C., Kim, H., Kim, H. & Lee, C. Enhancement in the photoluminescence of ZnS nanowires by TiO2 coating and thermal annealing. Journal Of Luminescence. **130** pp. 516-519 (2010)

[24] Arcoleo, V., Goffredi, M. & Liveri, V. Calorimetric investigation of the formation of ZnS nanoparticles in w/o microemulsions. Journal Of Thermal Analysis And Calorimetry. **51** pp. 125-133 (1998)

[25] Sou, I., Ma, Z., Zhang, Z. & Wong, G. Temperature dependence of the responsivity of II–VI ultraviolet photodiodes. Applied Physics Letters. **76** pp. 1098-1100 (2000)

[26] Goharshadi, E., Mehrkhah, R. & Nancarrow, P. Synthesis, characterisation, and measurement of structural, optical, and phtotoluminescent properties of zinc sulfide quantum dots. Materials Science In Semiconductor Processing. **16** pp. 356-362 (2013)

[27] Liao, X., Wang, H., Zhu, J. & Chen, H. Preparation of Bi2S3 nanorods by microwave irradiation. Materials Research Bulletin. **36** pp. 2339-2346 (2001)

[28] Joicy, S., Saravanan, R., Prabhu, D., Ponpandian, N. & Thangadurai, P. Mn 2+ ion influenced optical and photocatalytic behaviour of Mn–ZnS quantum dots prepared by a microwave assisted technique. Rsc Advances. **4** pp. 44592-44599 (2014)

[29] Aoki, R., Santos Torres, E., Jesus, J., Lourenço, S., Fernandes, R., Laureto, E. & Silva, M. Application of heterostructured CdS/ZnS quantum dots as luminescence down-shifting layer in P3HT: PCBM solar cells. Journal Of Luminescence. **237** pp. 118178 (2021)

[30] Mall, M., Kumar, P., Chand, S. & Kumar, L. Influence of ZnS quantum dots on optical and photovoltaic properties of poly (3-hexylthiophene. Chemical Physics Letters. **495** pp. 236-240 (2010)

[31] Santos Torres, E., Aoki, R., Jesus, J., Duarte, J., Lourenço, S. & Silva, M. Synthesis and characterisation of CdS/ZnS heterostructures to improve the optical properties of CdS quantum dots. Journal Of Luminescence. **257** pp. 119706 (2023)

[32] Menke, S. & Holmes, R. Exciton diffusion in organic photovoltaic cells. Energy & Environmental Science. **7** pp. 499-512 (2014)

[33] Ummartyotin, S. & Infahsaeng, Y. A comprehensive review on ZnS: From synthesis to an approach on solar cell. Renewable And Sustainable Energy Reviews. **55** pp. 17-24 (2016)

[34] Patil, P. Synthesis of Semiconductor Quantum Dots, Study of Their Optical Properties and Their Application in Sensitised Solar Cells. (Dept. of Physics,2015)

[35] Mirahmadi, F., Marandi, M., Karimipour, M. & Molaei, M. Microwave activated synthesis of Ag2S and Ag2S@ ZnS nanocrystals and their application in well-performing quantum dot sensitised solar cells. Solar Energy. **202** pp. 155-163 (2020)

[36] Lee, J., Kwon, B., Park, H., Kim, H., Kim, M., Park, J., Kim, E., Yoo, S., Jeon, D. & Kim, S. Exciton dissociation and charge-transport enhancement in organic solar cells with quantum-dot/N-doped CNT hybrid nanomaterials. Advanced Materials. **25** pp. 2011-2017 (2013)

[37] Jabeen, U., Adhikari, T., Shah, S., Pathak, D., Kumar, V., Nunzi, J., Aamir, M. & Mushtaq, A. Synthesis, characterisation and photovoltaic applications of noble metal—doped ZnS quantum dots. Chinese Journal Of Physics. **58** pp. 348-362 (2019)

[38] Rossetti, R., Ellison, J., Gibson, J. & Brus, L. Size effects in the excited electronic states of small colloidal CdS crystallites. The Journal Of Chemical Physics. **80** pp. 4464-4469

(1984)

[39] Verma, A., Karar, N., Bakhshi, A., Chander, H., Shivaprasad, S. & Agnihotry, S. Structural, morphological and photoluminescence characteristics of sol-gel derived nano phase CeO 2 films deposited using citric acid. Journal Of Nanoparticle Research. **9** pp. 317-322 (2007)

[40] Xie, R., Battaglia, D. & Peng, X. Colloidal InP nanocrystals as efficient emitters covering blue to near-infrared. Journal Of The American Chemical Society. **129** pp. 15432-15433 (2007)

[41] Yang, X., Qiao, J., Chen, Z., Wen, Z., Yin, H. & Hao, X. CdSe quantum dot organic solar cells with improved photovoltaic performance. Journal of Physics D: Applied Physics. **54** pp. 115504 (2021)

[42] Green, M. Thin-film solar cells: review of materials, technologies and commercial status. Journal Of Materials Science: Materials In Electronics. **18** pp. 15-19 (2007)

[43] Liu, Y., Liang, C., Wu, J., Sharifi, T., Xu, H., Nakanishi, Y., Yang, Y., Woellne, C., Aliyan, A. & Marti, A. Atomic layered titanium sulfide quantum dots as electrocatalysts for enhanced hydrogen evolution reaction. Advanced Materials Interfaces. **5** pp. 1700895 (2018)

[44] Tu, W., Guo, W., Hu, J., He, H., Li, H., Li, Z., Luo, W., Zhou, Y. & Zou, Z. State-of-the-art advancements of crystal facet-exposed photocatalysts beyond TiO2: Design and dependent performance for solar energy conversion and environment applications. Materials Today. **33** pp. 75-86 (2020)

[45] Murugadoss, G. & Kumar, M. Synthesis and optical properties of monodispersed Ni 2+-doped ZnS nanoparticles. Applied Nanoscience. **4** pp. 67-75 (2014)

[46] Xuan, T., Liu, J., Li, H., Sun, H., Pan, L., Chen, X. & Sun, Z. Microwave synthesis of high luminescent aqueous CdSe/CdS/ZnS quantum dots for crystalline silicon solar cells with enhanced photovoltaic performance. RSC Advances. **5** pp. 7673-7678 (2015)

[47] Yang, Z., Gao, M., Wu, W., Yang, X., Sun, X., Zhang, J., Wang, H., Liu, R., Han, C. &

Yang, H. Recent advances in quantum dot-based light-emitting devices: Challenges and possible solutions. Materials Today. **24** pp. 69-93 (2019)

[48] Park, K., Jung, S., Kim, J., Ko, B., Shim, W., Hong, S. & Song, S. Boosting photovoltaic performance in organic solar cells by manipulating the size of MoS2 quantum dots as a hole-transport material. Nanomaterials. **11** pp. 1464 (2021)

[49] Amollo, T., Mola, G. & Nyamori, V. Polymer solar cells with reduced graphene oxide–germanium quantum dots nanocomposite in the hole transport layer. Journal Of Materials Science: Materials In Electronics. **29** pp. 7820-7831 (2018)

[50] Xia, Y., Nguyen, T., Yang, M., Lee, B., Santos, A., Podsiadlo, P., Tang, Z., Glotzer, S. & Kotov, N. Self-assembly of virus-like self-limited inorganic supraparticles from nanoparticles. Nature Nanotechnology. **6** pp. 580-587 (2011)

[51] Kokil, A., Yang, K. & Kumar, J. Techniques for characterisation of charge carrier mobility in organic semiconductors. Journal Of Polymer Science Part B: Polymer Physics. **50** pp. 1130-1144 (2012)

[52] Ramírez, M., Cuadro, A., Alvarez-Builla, J., Castaño, O., Andrés, J., Mendicuti, F., Clays, K., Asselberghs, I. & Vaquero, J. Donor-(π-bridge)-azinium as D-π-A+ one-dimensional and D-π-A+-π-D multidimensional V-shaped chromophores. Organic & Biomolecular Chemistry. **10** pp. 1659-1669 (2012)

[53] Tse, S., Tsang, S. & So, S. Polymeric conducting anode for small organic transporting molecules in dark injection experiments. Journal Of Applied Physics. **100** pp. 063708 (2006)

[54] Malliaras, G. & Scott, J. Numerical simulations of the electrical characteristics and the efficiencies of single-layer organic light emitting diodes. Journal Of Applied Physics. **85** pp. 7426-7432 (1999)

[55] Davids, P., Campbell, I. & Smith, D. Device model for single carrier organic diodes. Journal Of Applied Physics. **82** pp. 6319-6325 (1997)

[56] Liu, C. & Chen, S. Charge mobility and charge traps in conjugated polymers. Macro-

molecular Rapid Communications. **28** pp. 1743-1760 (2007)

[57] Mott, N. & Gurney, R. Electronic processes in ionic crystals, Clarendon Press1948.

[58] Taylor, D. Space charges and traps in polymer electronics. IEEE Transactions On Dielectrics And Electrical Insulation. **13** pp. 1063-1073 (2006)

[59] Tessema, G. Charge transport across bulk heterojunction organic thin film. Applied Physics A. **106** pp. 53-57 (2012)

[60] Matsushima, T. & Murata, H. Observation of space-charge-limited current due to charge generation at interface of molybdenum dioxide and organic layer. Applied Physics Letters. **95** pp. 301 (2009)

[61] Tanase, C., Blom, P. & Leeuw, D. Origin of the enhanced space-charge-limited current in poly (p-phenylene vinylene. Physical Review B. **70** pp. 193202 (2004)

[62] Borsenberger, P. & Weiss, D. Organic photoreceptors for imaging systems, M. (Dekker New York1993)

[63] Zhu, Y., He, Y., Jiang, S., Zhu, L., Chen, C. & Wan, Q. Indium–gallium–zinc–oxide thin-film transistors: Materials, devices, and applications. Journal Of Semiconductors. **42** pp. 031101 (2021)

[64] Liu, H. & Zhang, J. Dark current and noise analyses of quantum dot infrared photodetectors. Applied Optics. **51** pp. 2767-2771 (2012)

[65] Kublitski, J., Hofacker, A., Boroujeni, B., Benduhn, J., Nikolis, V., Kaiser, C., Spoltore, D., Kleemann, H., Fischer, A. & Ellinger, F. Reverse dark current in organic photodetectors and the major role of traps as source of noise. Nature Communications. **12** pp. 551 (2021)

CHAPTER 6

ENHANCED COLLECTION OF PHOTOCURRENTS USING CORE-SHELL QUANTUM DOTS DECORATED POLYMER COMPOSITE FILMS

energy&fuels

pubs.acs.org/EF Article

Enhanced Collection of Photocurrents Using Core–Shell Quantum Dots Decorated Polymer Composite Films

Abiodun Kazeem Ogundele and Genene Tessema Mola*

Cite This: https://doi.org/10.1021/acs.energyfuels.4c02652 Read Online

ACCESS Metrics & More | Article Recommendations | Supporting Information

ABSTRACT: Core–shell semiconductor quantum dots (SQDs) were synthesized via the microwave irradiation method from cadmium and zinc sulfides ($Cd_xS/Zn_{1-x}S$). The SQDs were incorporated into the electron transport layer of thin film polymer solar cells (TFPSCs) to assist in light trapping and charge collection processes. The up and down conversion of radiation in SQDs is expected to boost absorption between the lower energy bandgap core and wide energy bandgap shell, respectively. The investigation employs a polymer blend consisting of a poly[[4,8-bis[(2-ethylhexyl)oxy]benzo[1,2-*b*′]dithiophene-2,6-diyl][3-fluoro-2-[(2-ehylhexyl)-carbonyl]thieno[3,4-*b*]thiophenediyl]]:[6,6]-phenyl C_{71} butyric acid methyl ester (PTB7:PC71BM) as a photoactive medium of the solar cells. Consequently, the experimental evidence suggested that the inclusion of SQDs significantly improved the power conversion efficiency (PCE) of the solar cell as a result of increased energy transfer, exciton generation, and charge collection processes in TFPSCs. Furthermore, the performances of the solar cells are found to be dependent on the concentration of the SQD in the transport layer, where the highest PCE of 7.13% was measured at an optimal concentration of 0.375 wt %. This is an important development of the investigation with a recorded increment in PCE by nearly 23% from the reference cell.

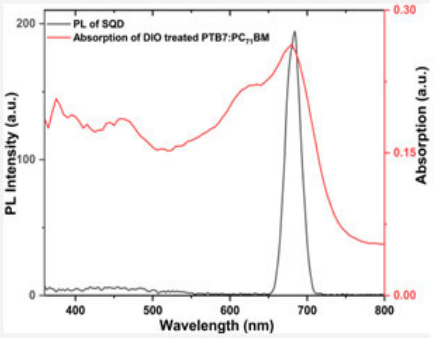

Abstract

Core-shell semiconductor quantum dots (SQDs) were synthesised via the microwave irradiation method from cadmium and zinc sulfide (CdS/ZnS). The SQDs were incorpo-

rated into the electron transport layer of thin film polymer solar cells (TFPSCs) to assist in light trapping and charge collection processes. The up and down-conversion of radiation in SQDs is expected to boost absorption between the lower energy bandgap core and wide energy bandgap shell, respectively. The investigation employs a polymer blend consisting of poly[[4,8-bis[(2-ethylhexyl)oxy]benzo[1,2-b]dithiophene-2,6-diyl][3-fluoro-2-[(2-ethylhexyl)-carbonyl]-thieno[3,4-b]thiophenediyl]]:[6,6]-phenyl C_{71} butyric acid methyl ester (PTB7:$PC_{71}BM$) as a photoactive medium of the solar cells. Consequently, the experimental evidence suggested that the inclusion of SQDs significantly improved the power conversion efficiency (PCE) of the solar cell as a result of increased energy transfer, exciton generation, and charge collection processes in TFPSCs. Furthermore, the performances of the solar cells are found to be dependent on the concentration of the SQD in the transport layer, where the highest PCE of 7.13% was measured at an optimal concentration of 0.375 wt%. This is an important development of the investigation with a recorded increment in PCE by nearly 23% from the reference cell.

6.1 Introduction

Solar energy remains one of the safest, cleanest, and most desirable alternative sources of energy to replace those traditional environmentally unfriendly yet depleted fossil fuels to reduce global greenhouse gase [1]. Interestingly, about 430 quintillion joules of energy are radiated from the sun per hour, while about 580 quintillion joules of energy are consumed globally per year [2]. This enormous solar energy can be tapped to reduce fossil fuel consumption to mitigate environmental pollution. However, a vast amount of radiated solar energy in hours could be enough to fulfil the energy demand for the world population for a year, but it is sadly underutilized as its use only accounts for about 4.5% of global electricity today, according to the International Energy Agency (IEA). This is due to various reasons ranging from the lack of effective solar energy conversion technologies, cumbersome device manufacturing processes coupled with the high cost of production, and knowledge gaps. Impressively, organic solar cells (OSC) are cost-effective, lightweight, solution-process-able, and suitable for roll-to-roll production making them more attractive from an economic perspective with the power conversion efficiencies (PCEs) currently crossing 19%, which is comparable to several inorganic solar cell technologies [3, 4, 5, 6, 7, 8]. However, OSCs still suffer from a shortfall in photons to energy conversion efficiencies [9, 10] because of some inherent inadequacies and challenges such as limited durability, materials variability, low efficiency, environmental

sensitivity, non-robust temperature tolerance, narrow absorption range, competitive market, facelift costs, etc. [11, 12, 13]. Researchers have continued work in the quest to solve these inadequacies by bridging the knowledge gaps. For instance, the emergence of bulk heterojunction (BHJ) with fullerene or non-fullerene acceptors over the last few decades has reduced some of the shortcomings (such as poor charge transport processes, instability, and large energy losses) exhibited by the single layer and bilayers solar absorbers [14] Numerous strategies have been used to continually improve the performance of BHJ thin film organic solar cells. Some of these strategies include the synthesis of eficient new donor and acceptor polymer molecules, [15, 16, 17, 18, 19, 20, 21] fine-tuning of morphology and mesoscopic aggregation of molecules in the photoactive layers, [13, 22] the stacking of multiple active blends-tandem solar cells, [23] optimisation of the donor-acceptor concentration in the absorber layer [24], the use of solvent additives and choice of host solvents [25, 26, 27] and the incorporation of a third component to influence the properties of charge transport layers positively [28, 29, 30, 31, 32, 33, 34, 35]. The third components often employed in the various layers of standard and inverted device architectures of organic solar cells including metallic nanoparticles, plasmonic nanocomposites, and semiconductor quantum dot (SQDs) are found to have a significant influence on carriers dissociation, charge transfer, photon harvesting processes, and reducing energy loss for enhanced power conversion efficiencies [36, 37, 38, 39, 40, 41]. This study demonstrated the application of core - shell SQD ($Cd_xS/Zn_{1-x}S$) in the electron transport layer of an inverted thin film polymer solar cell (TFPSC) containing photoactive layer blends of poly[[4,8-bis[(2-ethylhexyl)oxy]benzo[1,2-b]dithiophene-2,6-diyl][3-fluoro-2-[(2-ethylhexyl)-carbonyl]-thieno[3,4-b]thiophenediyl]]:[6,6]-phenyl C_{71} butyric acid methyl ester (PTB7:PC_{71}BM). SQDs are a unique type of semiconductor material whose sizes range between 2 and 10 nm, exhibiting unique photophysical, electronic, and optical properties evident in the form of quantum size effects, size-controlled fluorescence, high fluorescence quantum yields, multiple exciton generation, stability against bleaching, up-and down-conversion photoluminescence, e.t.c. The SQDs have been notably used in various applications due to the aforementioned features [42, 43, 44]. SQDs can also be classified into core, alloy, and core-shell SQDs. In this study, SQD materials ($Cd_xS/Zn_{1-x}S$) with a medium energy bandgap core and a wide bandgap shell were used in the electron transport layer of TFPSC to assist in improving light trapping in the medium. The SQDs employed in this study are group II-VI cadmium sulfide (Cd_xS) - core and zinc sulfide ($Zn_{1-x}S$) - shell with different ratios of group II metals. The energy bandgap of CdS and ZnS bulk semiconductors are 2.4 and 3.6 eV, respectively [45, 46]. SQDs of these materials, however, change properties due to the quantum size effect

(QSE) as it is a well-known fact that SQD produces a broad optical spectrum with the lowest size of about 2 nm emitting blue light, while a size in the order of 10 nm gives off a red colour [47]. These combined effects of core-shell SQDs can be used to broaden optical absorption spectra and capture high photon energy, resulting in an improved solar cell performance. The microwave-synthesised SQD has been widely reported to yield small inorganic particles with a uniform distribution of particle sizes, high purity, fast reaction time, better control of aggregation, as well as cost-effectiveness [48, 49, 50, 51].

6.2 Experimental section

6.2.1 Materials resources

Thin film transparent conducting oxides (TCO) are commonly used as electrodes in the fabrication of thin film organic solar cells. In this study, unpatterned indium tin oxide (ITO) coated glass substrates were employed with sizes 30 × 30 mm in the preparation of the solar cells. The chemicals used for the synthesis of SQD include cadmium acetate purchased from May & Baker Ltd., Dagenham, England with 98% purity, zinc acetate procured from NT Laboratory Supplies Ltd., Johannesburg, SA with 99% purity, thioacetamide, chlorobenzene (CB), molybdenum(VI) oxide 99.7% trace metals basis, 1,8-diiodooctane (DIO), and zinc oxide nanoparticle ink, supplied by Aldrich Chemical Company USA, Milwaukee, USA with 99% purity. The polymers, namely poly[[4,8-bis[(2-ethylhexyl)oxy]benzo[1,2-b]dithiophene-2,6-diyl][3-fluoro-2-[(2-ethylhexyl)-carbonyl]thieno[3,4-b]thiophenediyl]] (PTB7) with a purity of 97%, and [6,6]-phenyl C_{71} butyric acid methyl ester ($PC_{71}BM$) were purchased from the Ossila Company Ltd., United Kingdom and Luminescence Technology Corp., respectively.

6.2.2 Synthesis of semiconductor quantum dots

The bottom-up method involving two precursors was employed by modifying the processes developed by Soltani *et al* [51], Shi *et al* [52], and Rafea *et al* [53]. The core-shell SQDs were synthesised via a two-step path: the synthesis of the core (Cd_xS) followed by the growth of the shell ($Zn_{1-x}S$) around the core. A 1.33 g of cadmium acetate was dissolved in a beaker containing 100 mL of ethylene glycol to obtain a 0.05 M solution. This was thiol-stabilized with 4 mL of thioglycolic acid, followed by the addition of 0.563 43 g (75 mmol) of thioacetamide. The reaction mixture was stirred for about 10 minutes at approximately 5000 rpm. The reaction was then transferred to a Russell Hobbs (Model no. RHEM21L) domestic microwave with an output power of 700 W, following a working cycle of 30% for 25 minutes. The appearance

of a yellow precipitate signified the formation of cadmium sulfide. For the synthesis of the second precursor, ethanol was used as the solvent due to its lower boiling point compared to ethylene glycol, ensuring adequate ripening of the core SQD and preventing the nucleation of the shell. The second precursor was synthesised using the same process with lower concentrations: 0.548 73 g (25 mmol) of zinc acetate was dissolved in a beaker containing ethanol, stirred for 10 minutes at 5000 rpm, and later transferred to a microwave oven following a similar working cycle used for the core precursor. The appearance of a white precipitate indicated the formation of zinc sulfide SQD. The precursors were added dropwise and allowed to disperse uniformly using a sonication bath for 60 minutes at 40 °C. The resulting solution was placed at the center of the oven for 30 minutes with a power of 30%, during which the monolayers of the shell were deposited on the cores to form ($Cd_xS/Zn_{1-x}S$). The final precipitates were allowed to cool to room temperature and centrifuged for about 10 minutes at a speed of 4000 rpm. The precipitates were then re-dispersed in deionized water and ethanol several times to remove excess ionic remnants. Finally, the SQDs were dried in a vacuum oven at 60 °C for 24 hours, and their morphology was examined via high-resolution scanning electron microscopy (HRSEM), high-resolution transmission electron microscopy (HRTEM), and X-ray diffraction crystallography.

6.2.3 Devices fabrication

The un-patterned ITO-coated glass substrates were carefully etched by partially covering the ITO with photoresist black tape. The uncovered parts of the substrates were then partially immersed in a warm, bubble-free acidic solution composed of hydrochloric acid, nitric acid, and water in a ratio of 48%:4%:48%, respectively. The etched substrates were thoroughly and sequentially cleaned in a sonication bath using detergent, deionized water, ethanol, acetone, and isopropanol for 10 minutes each. The substrates were then blow-dried using a nitrogen gas gun and baked in an oven for 5 minutes at 100 °C. Meanwhile, the polymer blend consisting of PTB7:$PC_{71}BM$ in a 1:1.5 ratio was dissolved in a chlorobenzene co-solvent at a concentration of 25 mg/mL and stirred overnight for approximately 12 hours at 30 °C to ensure the miscibility of the polymers. Furthermore, the as-synthesised SQDs were dispersed in 0.800 g/mL of zinc oxide nanoparticle ink, which was used as an electron-selective interface layer, at different concentrations of 0.125, 0.375, and 0.625 wt.%, respectively. These solutions were stirred for 12 h on a hot plate and pre-ultrasonicated for 1 hour, along with the undoped reference solution containing zinc oxide nanoparticle ink as indicated in the supplier manual, to ensure well-dispersed nanoparticles in the solution. The modified electron-selective interface layer solutions

were coated on the substrates at 4000 rpm for 40 s and annealed at 120 °C for 20 minutes. Then, the photoactive layer was spin-coated from the polymer blend solution onto all substrates (with pre-coated modified electron transport layers and the reference electron transport layer without SQDs) at 1200 rpm for 40 seconds in an ambient environment. The samples were then dried inside a furnace for 1 hour in a nitrogen-filled atmosphere at a temperature of 50 °C. All samples were later properly mounted on a mask and transferred into the vacuum chamber of the Edward 306 deposition unit, where a 10 nm thin layer of molybdenum trioxide (MoO_3) as the hole transport layer and 80 nm of aluminum (Al) as the top electrode were sequentially deposited at a pressure of 1.7×10^{-6} mbar. The active area of the cells was 2.80 mm^2. The schematic diagram of the device structure and the energy level alignment of the materials used are given in Figure 6.1. The current density vs. voltage (J-V) characteristics data under

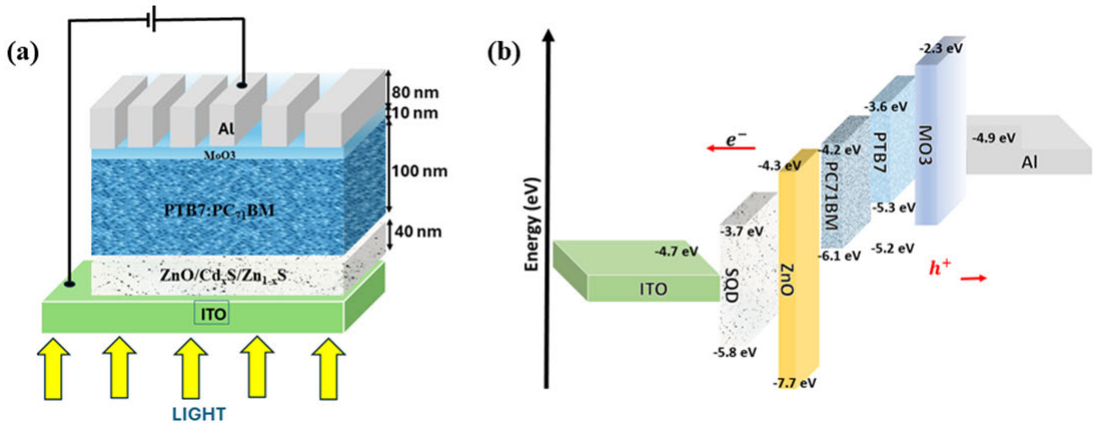

Figure 6.1: (a) Schematic diagram of device structure (b) Energy level alignments of the materials used.

illumination and dark conditions were measured using a computer-interfaced Keithley model SS50AAA at a light intensity of 100 $mWcm^{-2}$.

6.3 Results and discussion

6.3.1 Morphology of as-synthesised SQDs

The surface morphology of the as-synthesised SQD was studied with a high-resolution scanning electron microscope (SEM), while the transmission electron microscope (TEM) assisted in providing detailed structural information at the atomic scale (in the nanometre range) (see Figure 6.2a& b). The elemental analysis of the SQD revealed by energy dispersive X-ray (EDX) indicates the presence of elements, namely cadmium (Cd), zinc (Zn), and sulphur

(S), as shown in Figure 6.2d. The appearance of oxygen is traceable to the exposure of the sample to the ambient environment during the process of characterisation. Furthermore, both

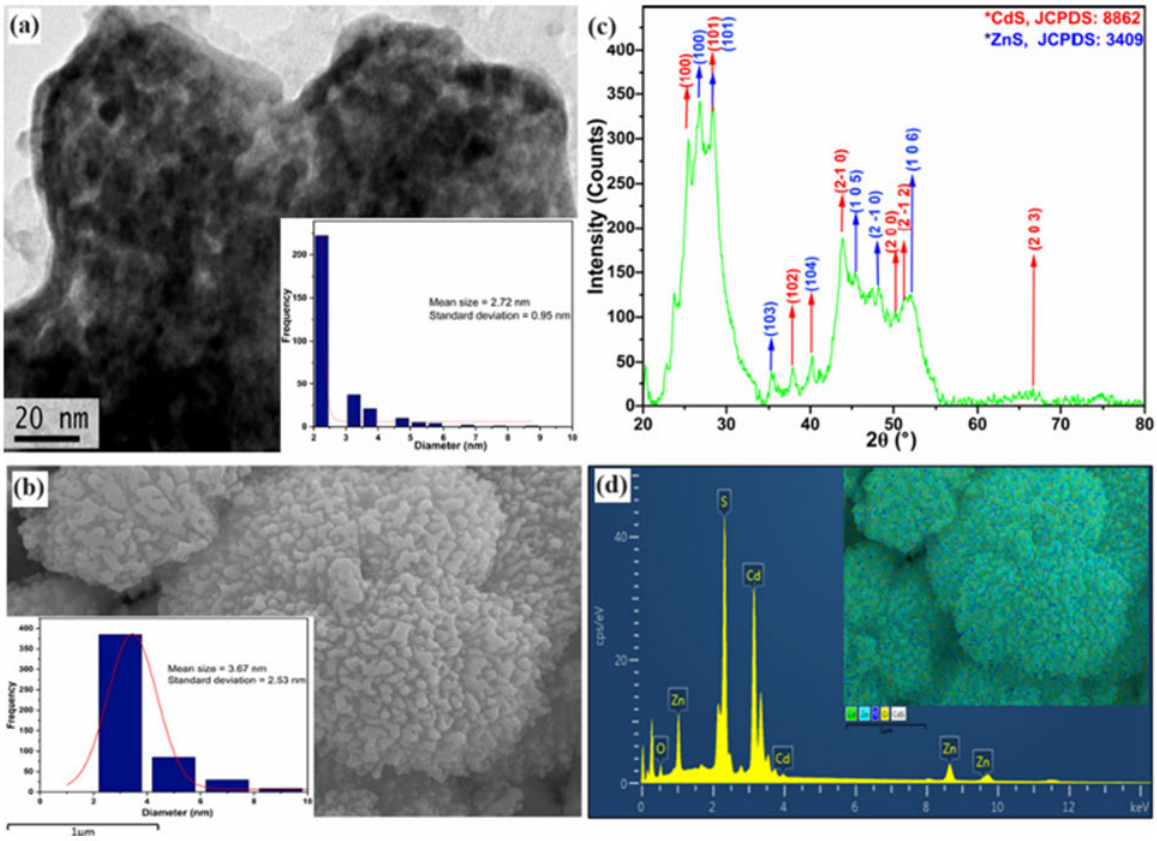

Figure 6.2: (a) HRTEM of ($Cd_xS/Zn_{1-x}S$) SQD with its size distribution (b) HRSEM of ($Cd_xS/Zn_{1-x}S$) SQD with its size distribution (c) XRD of the ($Cd_xS/Zn_{1-x}S$) SQD, and (d) EDX of the ($Cd_xS/Zn_{1-x}S$) SQD.

TEM and SEM suggested that the as-synthesised SQD is a core-shell structure. The size distribution observed through the TEM and SEM images showed an average of 2.72 nm and 3.67 nm, respectively. The difference in calculated sizes from SEM and TEM images is due to the precision of both techniques. More detailed information about the size, shape, and internal structure is obtained from TEM, while SEM provides evidence about the topography and surface morphology of the sample. For instance, SEM images are often taken by coating samples with appropriate conducting species, which tends to give overestimated sample sizes [54]. The histogram showed that sizes between 2 nm and 4 nm accounted for about 70% of the samples taken, while the rest ranged from 4 nm to 10 nm. The size confinement effects of the SQDs have been widely reported for the energy of the particle localized in quantum dots and the wave function of the confined particles [55], resulting in discrete and tunable optical spectra with the smallest size absorbing in the UV range and the largest size (of about 10 nm)

absorbing in the infrared region.

The morphology of the SQD was further characterized by X-ray diffraction (XRD) crystallography (Rigaku Miniflex) to investigate the material structure and the crystal phases of the CdS, ZnS, and CdS/ZnS SQD (see Figure 6.2c). This involves irradiating the core-shell SQD samples with X-rays recording the diffraction patterns using an XRD machine and comparing them with standard reference patterns from the international database. The crystal structural data available in the JCPDS cards (CdS: JCPDS: 8862, ZnS, JCPDS: 3409) show that both the core and shell SQDs are hexagonal with a cell volume of 99.93 Å^3 (4.1348 Å × 3.5810 Å × 6.7490 Å) and 156.97 Å^3 (3.8140 Å × 3.3031 Å × 12.4600 Å), respectively. The phase analysis of the XRD patterns of the ($Cd_xS/Zn_{1-x}S$) SQD is shown in Figure 6.2c. The peaks observed at 2θ values of (1 0 0), (1 0 1), (1 0 2), (2-1 0), (2 0 0), (2-1 2), and (2 0 3) are attributed to the CdS core, while the peaks at (1 0 0), (1 0 1), (1 0 3), (1 0 4), (1 0 5), and (2-1 0) are attributed to the ZnS shell. At 28.2°, the XRD patterns of ($Cd_xS/Zn_{1-x}S$) SQD revealed a peak overlap at (1 0 1) between the hexagonal structure of the CdS core and the hexagonal structure of the ZnS shell. Generally, the well-pronounced sharp peak's narrow width and the evaluated small size distribution indicate a high crystallinity of the SQD, as shown in Figure 6.1c and Table 6.1 [56]. This indicates a favourable electronic state interaction between the core and shell SQD, enhancing their performance in photovoltaic (PV) devices [57]. Scherrer's equation (6.1) below was used to obtain crystalline sizes for different peaks.

$$D = \frac{k\lambda_{\text{Cu}}}{\beta_{hkl}\cos\theta}, \tag{6.1}$$

where D is the crystalline size of the SQD, λ_{Cu} is 1.540 56 Å (wavelength of copper radiation), k is a constant dependent on the shape of the crystalline material ($k = 0.89$), β_{hkl} represents the Full Width Half Maximum (FWHM) which is a measure of the difference between two values of the independent variable for which the dependent variable is half of the maximum value, measured in radians, and θ is the Bragg's angle of diffraction in radians. The average size of the crystallites was calculated from the data in Table 6.1 to be approximately 3.13 nm, which is consistent with the values obtained from both SEM and TEM image analysis.

6.3.2 Optical characterisation of as-synthesised SQDs

The optical properties of the electron transport layer with and without SQD were investigated by measuring the transmittance of the buffer layer using a Rayleigh UV 1601 spectrophotometer. The transmittance of the films of zinc oxide nano ink with and without SQD (see the inset

Table 6.1: XRD analysis of $Cd_xZn_{1-x}S$ SQD.

Peak No	**2θ (º)**	**hkl (CdS)**	**hkl (ZnS)**	**FWHM (º)**	**D (nm)**
1	25.02	1 0 0	-	3.438	2.34
2	26.95	-	1 0 0	2.865	2.82
3	28.12	1 0 1	1 0 1	6.875	1.18
4	35.10	-	1 0 3	4.584	1.80
5	36.54	1 0 2	-	1.146	7.22
6	40.10	-	1 0 4	2.865	2.92
7	43.72	2 -1 0	-	5.157	1.64
8	45.56	-	1 0 5	2.865	2.97
9	47.70	-	2 -1 0	2.292	3.75
10	50.96	2 0 0	-	4.011	2.17
11	51.81	2 -1 2	-	4.011	2.18
12	51.97	-	1 0 6	1.146	7.63
13	66.70	2 0 3	-	4.584	2.05

of Figure (6.3a) showed that the zinc oxide nano ink layer allows a significant amount of light (ß3% transmittance in the visible spectrum) to pass through which underscored its use as a transparent material with a low scattering of incident light which is desirable for efficient light emission. highlighting its use as a transparent material with minimal scattering of incident light, which is desirable for efficient light emission. It could be seen that the optimum transmittance of the zinc oxide was observed in the visible and near-infrared regions (780-900 nm) of the spectrum. The as-synthesised SQD dispersed in ZnO nano-ink suspension also indicated which showed that the doping of SQD did not negatively interfere with features of transparent zinc oxide nano-ink suspension in harnessing solar energy. The Rayleigh UV 1601 spectrophotometer was used to measure the optical absorption of the SQD (see Figure 6.3a) as well as the absorption of the polymers PTB7, $PC_{71}BM$, and the PTB7:$PC_{71}BM$ blend (see Figure 6.3b. The PTB7 shows strong absorption from 500 to 750 nm and recorded peak absorbance at 625 and 680 nm, while the absorption spectrum range for the PC71BM was between 315 to 750 nm with bumps at 404, and 466 nm, which are primarily due to $\pi-\pi^*$ electronic transitions. The absorption ranges noticed for the donor and acceptor complement each other producing a broader spectrum in the blends of PTB7:$PC_{71}BM$ with/without DIO. The absorbance peaks centred at 485 nm, 625 nm and 690 nm (see Figure 6.3b) are attributed to the vibrionic band's

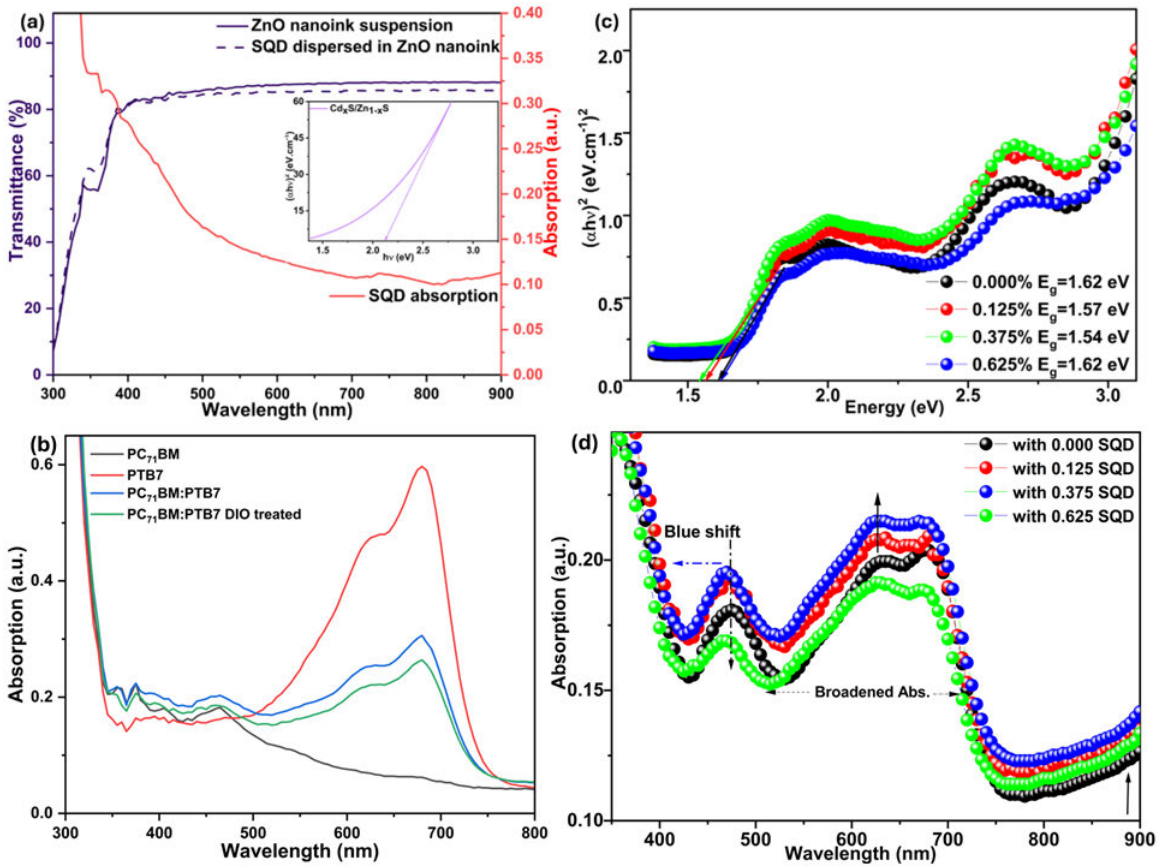

Figure 6.3: (a) Transmittance image of zinc oxide nano-ink suspension, & SQD dispersed in Isopropanol and absorption of SQD (inset bandgap of SQD) (b) UV-vis absorption of polymers solutions (c) Energy bandgap and (d) Optical absorption of PSCs films of pristine and modified electron transport layer devices.

transition from the ground state to the first excited state [58, 59]. Figure 6.3d demonstrates that the films of the modified devices incorporating SQD exhibit a stronger absorption peak at 625 nm compared to the pristine device suggesting the influence of SQD in the optical absorbance of the films. The improved electronic transitions from the highest occupied molecular orbital (HOMO) to the lowest unoccupied molecular orbital (LUMO) of PTB7 boost the number of exciton generation that ultimately increases the probability of dissociated free charge carriers available for collection at the electrodes. Generally, the films with SQD at concentrations of 0.125, and 0.375 wt.% showed a broader spectrum than the pristine device film. The synergy between the moderate energy gap CdS core quantum and relatively larger ZnS shell-QD leads to the energy offset which assists in confining charge carriers within the core thereby preventing them from escaping into the shell. This leads to the quantum confinement effect that influences both the electronic and optical properties of the SQD in the TFPSCs [60]. The wider bandgap shell of SQD enhances stability by acting as a protective layer and mitigating

the Auger recombination, a non-radiative recombination process that could reduce or limit the efficiency of SQD. Summarily, the synergy arising from the difference in energy bandgap of core-shell SQD assisted in engineering the optical and electronic properties of SQD for solar cell applications among others [61, 62]. This feature of SQD was carefully harnessed in the electron transport functional layer of the device in reducing the energy loss (see Figure 6.3c). The Tauc's equation given by equation (6.2) was used to obtain the energy bandgap (2.11 eV) of the SQD dispersed in water, the reference pristine device, and the modified electron transport layer films of the devices with or without SQD.

$$(\alpha h\nu)^{\gamma} = \beta(h\nu - E_g), \tag{6.2}$$

where h is the Planck's constant, ν is the frequency of the photon, $h\nu$ is the photon energy in eV, α is the absorption coefficient, β is a constant dependent on the nature of the material (amorphous or crystalline), and γ is a constant dependent on the type of transition (direct allowed transition, $\gamma = 2$ or indirect allowed transition, $\gamma = \frac{1}{2}$) between the valence band and conduction band. The graph of $(\alpha h\nu)^{\gamma}$ vs. $h\nu$ was used to obtain the bandgap at $(\alpha h\nu)^{\gamma} = 0$. The influence of the SQD on the optical absorption of the devices' films led to an increase in the absorption peaks of the modified devices with 0.125% and 0.375% (see Figure 6.3d) SQD concentrations at 470 nm and 625 nm, which is consistent with the absorption spectrum of SQD. Moreover, a blue shift was also noted for all the modified devices' films at 470 nm, which could be attributed to the impact of the SQD shell (ZnS), while a strong visible absorption was traceable to the (core - CdS) SQD, leading to a broadened spectrum linked to the synergy between core-shell SQD. The device with 0.375% SQD in the modified electron transport layer recorded the highest absorbance coefficient and the broadest optical spectrum. Interestingly, the modified devices recorded favourably lower energy loss than the pristine device. This further proved that the addition of SQD in the electron transport layer (see Table 6.2) is favourable to the device fabrication by reducing the geminate recombination in TFPSCs.

The photoluminescence (PL) intensities of the SQD, polymers, and films of devices were investigated using a PerkinElmer LS-45 Fluorescence Spectrometer. For instance, the overlapping of the PL of SQD with the absorption spectrum range of the photoactive blends and vice-versa, as noted in Figures 6.4a & b, could easily contribute to the enhanced Förster resonance energy transfer (FRET) from $Cd_xS/Zn_{1-x}S$ to donor PTB7, generating additional excitons that dissociate into free charge carriers, leading to a surge in photocurrent densities (J_{sc}) for the modified TFPSC devices. The effect of modified electron transport layers is evident from the summary in Table 6.2 [63]. The emission photoluminescence showed that the SQD exhib-

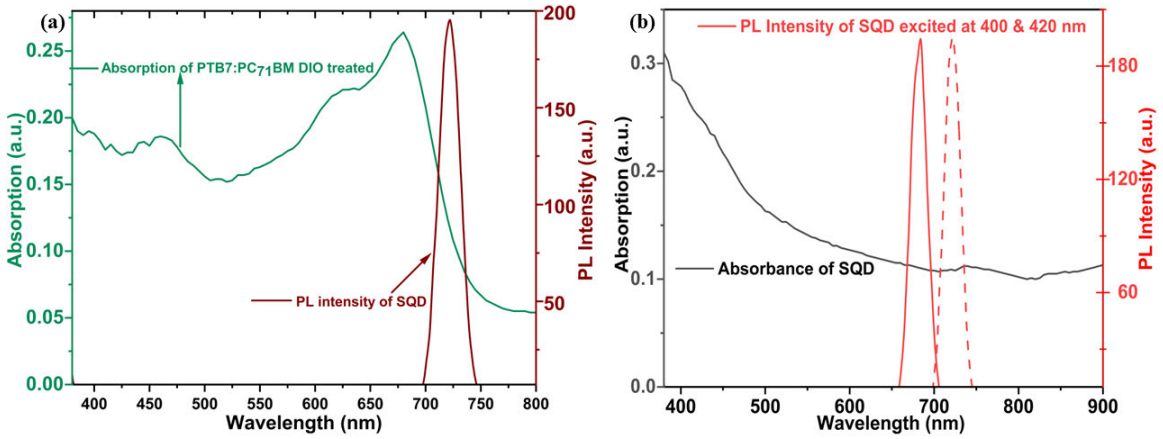

Figure 6.4: (a) PL intensity of SQD and UV and optical absorption of PTB7:$PC_{71}BM$ treated with DIO (b) PL intensity and UV absorption of SQD.

ited downward conversion photoluminescence (DCPL), which is a process in which absorbed high-energy photons are converted to photons (usually multiple photons) with lower energies (longer wavelengths). This is evident with the emission PL intensity in Figure 6.4b, where the excited wavelength at 400 and 420 nm led to pronounced emission peaks at higher wavelengths (or lower energies) around 683 and 720 nm, indicating conversion of absorbed higher energy photons into lower energy photons, which fall within the absorption spectrum (approximately 500 to 800 nm) of the PTB7:$PC_{71}BM$/DIO blend (see Figure 6.4b).

6.3.3 J-V characteristics of the devices

The inverted device architecture is composed of different layers of materials (Glass/ITO/ZnO:$Cd_xS/Zn_{1-x}S$/PTB7:$PC_{71}BM$/MoO_3/Al) as shown in Figure 6.5a. The J-V characteristics were measured under illumination and dark conditions. The current density-voltage (J-V) characteristics graph of the fabricated solar cells is provided in Figure 6.5b. The devices were fabricated with/without modified electron selective interface layers containing SQD at various concentrations as 0.0%, 0.125%, 0.375%, and 0.625%. The reference device parameters averaged over six diodes without SQD in the electron transport layer are: V_{oc}: 0.70 (0.69±0.01) V, J_{sc}: 15.67 (15.49±0.18) mA/cm^2, FF: 53.63 (52.59±1.04%), and PCE: 5.78 (5.70±0.08%). The modified electron selective interface layer devices improved significantly compared to the reference cell. For example, the solar cell fabricated at 0.125% doping level of $Cd_xS/Zn_{1-x}S$ recorded a PCE of 6.70% (6.62±0.08%) with a fill factor as high as 54.34% (53.30±1.04%). The maximum device performance was achieved from the device whose electron interface layer was doped with SQD at 0.375% concentration, this solar

cell recorded a power conversion efficiency of 7.13% (7.01±0.12%) (see Table 6.2), which is an increase of 23% compared to the reference cell. However, a sharp decline in the device parameter is observed as the concentration of SQD increases to 0.625 wt.% SQD, which showed a decrease in PCE to 4.89% (see Table 6.2). The drop in the cell parameters can be linked to the reduced values of current density and increase in the series resistance, which suggests that the high concentration of SQD in the electron selective layer impedes the good morphology of the device and promotes charge recombination at the interfaces [32, 64]. Table 6.2 shows the summary of the devices' parameters with ranges of values for the different diodes. The notable surge in the measured current densities for devices (0.125% and 0.375% wt.) with modified ETL can be linked to the alteration of energy levels, consequently reducing the energy losses as provided in Figure 6.3c and Table 6.2. This is aided by the characteristic features of SQD, which include inherent discrete energy levels, quantum confinement effects, and multiple exciton generations. The surge in current densities in these devices can also be attributed to the occurrence of light trapping in the solar cells due to the presence of SQD in the transport layer, which is evident in the improved light absorption, effective collection of additional carriers, deducible from the calculated carriers' mobilities, dissociation efficiency, and charge collection efficiency (see Table 6.3). The down-conversion of ultraviolet light to visible light is another mechanism exhibited by SQD to boost optical absorption in longer wavelength ranges. This is supported by the PL measurements, where the PL emission of SQD overlaps with the optical absorbency of the polymer blend $PC_{71}BM$:PTB7 (Figure 6.4 a&b). The down-conversion of SQD also involves energy transfer to the active layer blend via Förster resonance energy transfer. This is validated by earlier reported works suggesting that the incorporation of semiconductor quantum dots in the interlayer/buffer layer improved the generation of bound hole-electron pairs, which are eventually separated into free charge carriers. Moreover, it can also slow down the rate at which the modified work function reduces, thereby enhancing device stability [65, 30]. However, the inefficient hopping

Table 6.2: Thin film polymer solar cell parameters for devices with/without SQD in ETL.

ZnO:Cd$_x$S/Zn$_{1-x}$S	**E$_G$** (eV)	**E$_{LOSS}$** (eV)	**V$_{oc}$** (V)	**J$_{sc}$** (mAcm^{-2})	**FF** (%)	**PCE** (%)	**R$_s$** (Ω)	**R$_{SH}$** ($K\Omega$)
Pristine	1.62	0.91	0.69±0.01	15.49±0.18	52.59±1.04	5.70±0.08	291.5	8.78
0.125 wt.%	1.57	0.90	0.63±0.01	17.90±0.93	53.30±1.04	6.62±0.08	234.2	8.68
0.375 wt.%	1.54	0.87	0.65±0.02	18.95±0.55	54.62±1.62	7.01±0.12	229.2	8.82
0.625 wt.%	1.62	0.97	0.64±0.04	14.33±0.04	52.00±1.43	4.81±0.08	514.1	10.1

associated with carriers in polymers and the imperfect discontinuous morphology between quantum dots and the polymer matrix occurs at higher doping concentrations of SQD. This creates recombination sites that trap free charges, leading to non-radiative recombination and energy loss. The J-V measurements under dark conditions were also evaluated for all the devices to determine the effects of core-shell $Cd_xS/Zn_{1-x}S$ SQD on the TFPSCs by investigating the charge transport properties of the devices. We employed the Mott-Gurney charge transport theory using the space charge limited current (SCLC) regions of the J-V data. The low field mobility (μ_l), which is a measure of charge carriers' movement in the TFPSCs under low electric field conditions, and the activation factor (γ) can be determined by an equation (6.3) of the form:

$$J = \frac{9}{8}\epsilon_0\epsilon_r\mu_l\frac{V^2}{L^3}\exp\left(0.89\gamma\sqrt{\frac{V}{L}}\right), \tag{6.3}$$

where $\epsilon_r = 3.5$ is the relative permittivity of PTB7:$PC_{71}BM$ [66], ϵ_0 is the permittivity of free space ($= 8.85\times10^{-12}\,m^{-3}\,kg^{-1}\,s^4\,A^2$), $L \approx 150$ nm is the distance between the aluminum and ITO electrodes (see Figure 6.5a), J is the current density, and V is the applied voltage. The equation (6.3) above was simplified further to yield equation (6.4):

$$\ln J = 23.06 + \ln(\mu_l)V^2 + 2297.97\gamma V. \tag{6.4}$$

The quadratic and linear relationship (see the inset of Figure 6.5c) between the current density and voltage is used to estimate the field activation factor by employing space charge limited current (SCLC) data. Field activation factor describes the impact of electric field on carrier mobility in semiconductor materials, the increase in field activation factor shows that charge carriers move more efficiently through the device under the influence of increased electric field, which is well noted in Table 6.3 as the devices with 0.375, 0.125, pristine and 0.625%wt. showed better mobility and field activation factors in that order.

Table 6.3: Charge transport parameters of TFPSCs with/without SQD in the electron transport layer.

ZnO/$Cd_xS/Zn_{1-x}S$	μ_l **($cm^2V^{-1}s^{-1}$)**	γ **(cm V^{-1})**	G_{max} **($m^{-3}s^{-1}$)**	η_{diss} **(%)**	η_{coll} **(%)**
Pristine	3.02×10^{-6}	-6.58×10^{-5}	1.08×10^{27}	85.9	66.1
0.125 wt.%	4.12×10^{-6}	-1.76×10^{-4}	1.32×10^{27}	89.3	66.9
0.375 wt.%	4.36×10^{-6}	-1.29×10^{-4}	1.35×10^{27}	94.7	70.0
0.625 wt.%	1.44×10^{-6}	-7.67×10^{-6}	1.02×10^{27}	87.8	62.1

Furthermore, the low field mobility without trapping required the exponential function to

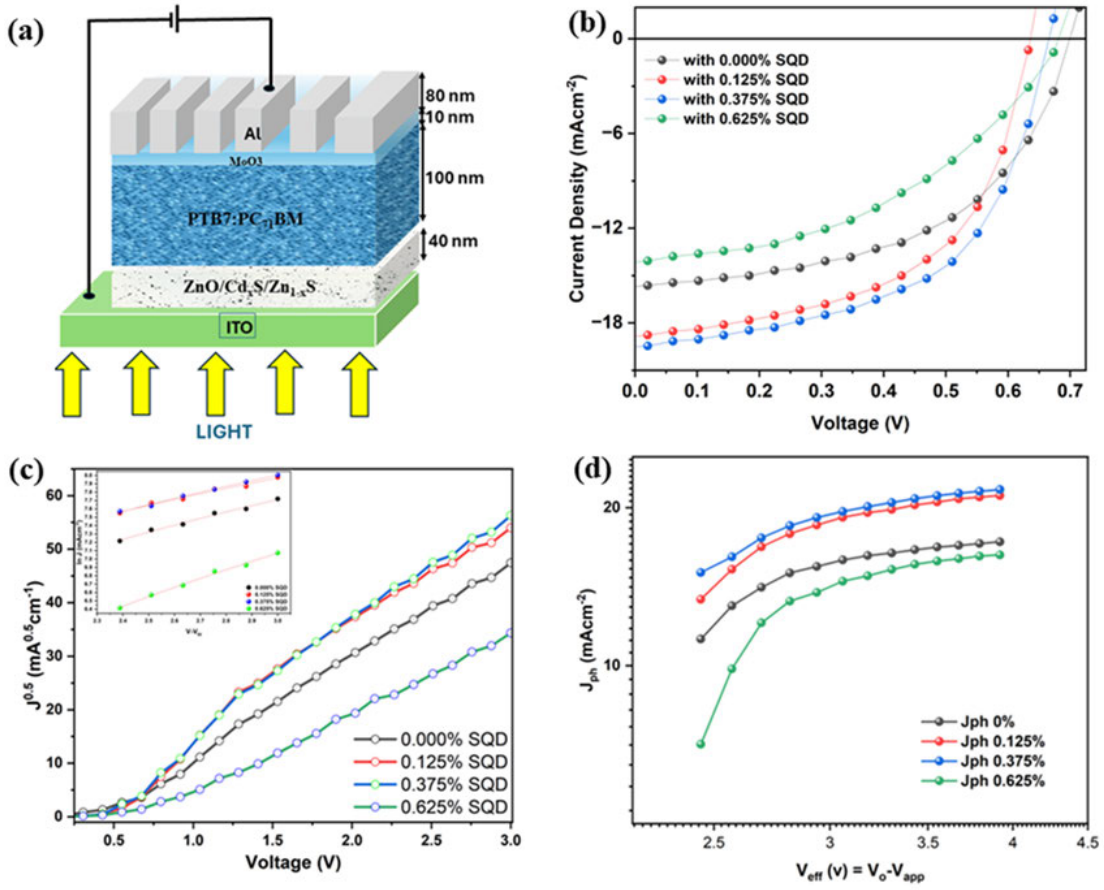

Figure 6.5: (a) Inverted device architecture of PSC with modified ETL (b) $J-V$ graphs under illumination & (c) $J^{0.5}$-V graphs under dark conditions (inset SCLC) (d) J_{ph} vs. V_{eff} for TFPSCs pristine and modified ETL devices.

decay to unity [63]. This yields equation (6.5) below upon substituting the values of ϵ_r, the relative permittivity, ϵ_0, the permittivity of free space, and considering the thicknesses of the active layer (100 nm), and buffer layers (ESL $\sim$ 40 nm and HTL $\sim$ 10 nm),

$$J^{0.5} = 101612\sqrt{\mu_l}V. \tag{6.5}$$

The linear fittings of $J^{0.5}$ against V (obtained under dark conditions) as shown in Figure 6.5c were eventually used to determine the values of the low field mobility for pristine devices and SQD-modified transport layer devices. The low field mobility increases for all the modified electron selective transport layer devices compared with the pristine devices, from $3.02\times10^{-6}\,\mathrm{cm^2V^{-1}s^{-1}}$ to $4.36\times10^{-6}\,\mathrm{cm^2V^{-1}s^{-1}}$ (see Table 6.3). Additionally, the relationship between the photocurrent (J_{ph}) and effective voltage (V_{eff}) was investigated as indicated in Figure 6.5d to deduce exciton dissociation efficiency, charge collection efficiency, and The saturation current (J_{sat}) was used to determine the maximum exciton generation ($G_{\mathrm{max}} = \frac{J_{\mathrm{sat}}}{qL}$), where q is the charge and L is the distance between the electrodes. The photocurrent den-

sity (J_{ph}) is calculated by evaluating the difference in current density under illumination (J_L) and dark conditions (J_D) (i.e., $J_{ph} = J_L - J_D$), and the effective voltage (V_{eff}) is obtained by evaluating the difference between the voltage (V_0) (at which $J_{ph} = 0$) and the applied voltage (V_a). The probabilities of charge dissociation (η_{diss}) and collection (η_{coll}) of the pristine and modified devices were determined by evaluating $\frac{J_{ph}}{J_{sat}}$ under short-circuit and maximum power area of the curve, respectively. The device with 0.375 wt % exhibited the highest probability of dissociation and collection of charges at 94.71% and 69.9%, respectively, as shown in Table 6.3. Importantly, all the modified devices showed enhanced dissociation efficiency, underscoring the positive impacts of the SQD doped into the ESL buffer layer. The reduced values of charge collection efficiency compared to dissociation efficiency indicate energy losses in the devices, which could be due to radiative energy losses, Joule heating, scattering losses, etc. The stability of the devices was investigated by taking J-V measurements under illumination for a period of 72 h in a 24 h interval after the initial measurements. Consequently, the shelf-life of the newly fabricated solar cells appears to be dependent on the concentration of SQD in the transport layer (see Figures S6.1, S6.2, S6.3, and S6.4 and Table S6.1 in the Supporting Information). The best device lifetime recorded in this study was at the optimum concentration of 0.375 wt %, whose PCE gradually decreased from 7.13% to 5.48% in 72 h. However, according to the data provided in the Supporting Information S6.4 and Table S6.2 and S6.3, the pristine cell showed a sharp decline in PCE from 5.78% to 3.762% after 24 h and with no tangible readings after 48 h. On the other hand, a marginal decrease in the shunt resistances was noted for the devices with modified electron layers after the first measurements except for the pristine device, which witnessed a significant reduction from 8.78 kΩ to 4.378 kΩ. Interestingly, there were indications of a series resistance reduction for devices with SQD concentrations of 0.125 and 0.375 wt.% after the first 24 h, which is a favourable condition for the devices' performance [67]. Generally, the decay rate of the devices with SQD at (0.125 and 0.375 wt %) showed a slower trend than the reference cell (see Figure S6.4 and Table S6.3 in Supporting Information), which further accentuates the beneficial impacts of SQD on the improved performance of the solar cells.

6.4 Conclusions

Core-shell ternary semiconductor quantum dots ($Cd_xS/Zn_{1-x}S$) were employed as a mechanism for light trapping in an inverted thin-film polymer solar cell (TFPSC) whose photoactive layer is composed of a PTB7:$PC_{71}BM$ blend. The devices with the modified electron transport

layer showed significant improvement in power conversion efficiency (PCE) and device stability compared to the reference cell. The investigation results suggest that the improved device performances depend on the SQD concentration in the ETL. The optimum SQD concentration for the best device performance recorded was 0.375 wt%, with a PCE of 7.13%, which is an increment of 23.4% compared to the reference cell. Such enhanced solar cell performance was attributed to the improved exciton generation, effective light trapping in the absorber medium, efficient dissociation of excitons, and improved charge transport processes due to the incorporation of SQDs. The down-conversion in SQDs played an important role in new absorption peaks and red-shifts. The improved collection of photocurrent is supported by evidence from the transport theory, such as better probabilities of charge dissociation and collection that cumulated into enhanced performances. Furthermore, the incorporation of SQDs has triggered molecular interactions between the active layer and electrodes, which resulted in energy level misalignment and reduced open-circuit voltage of all doped ETLs. Therefore, the improved device performances are mainly the consequence of better collections of the photogenerated current. This study showed the characteristic synergy inherent in semiconductor quantum dots in improving the various metrics of thin-film organic solar cells, ultimately leading to better device parameters and environmental stability of TFPSCs.

Acknowledgements

The authors express their profound gratitude for the support from the National Research Foundation (NRF), South Africa, and the University of KwaZulu-Natal (UKZN).

SUPPORTING INFORMATION

Enhanced collection of photo-current using core-shell quantum dots decorated polymer composite films

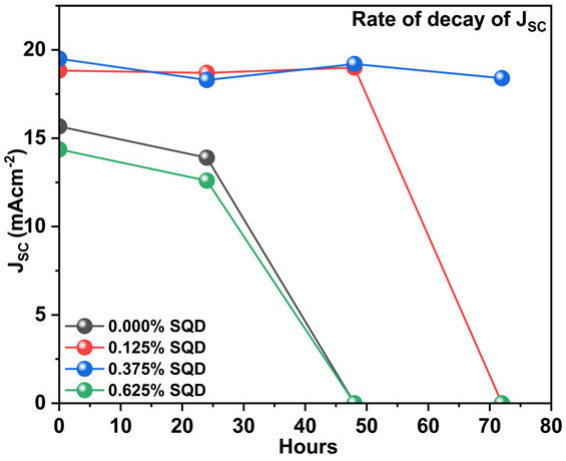

Figure S6.1: Change in the J_{sc} with the lifetime of the solar cell.

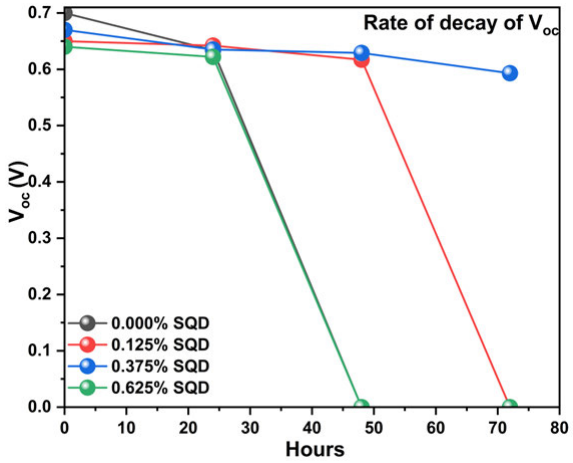

Figure S6.2: Change in the V_{oc} with the lifetime of the solar cell.

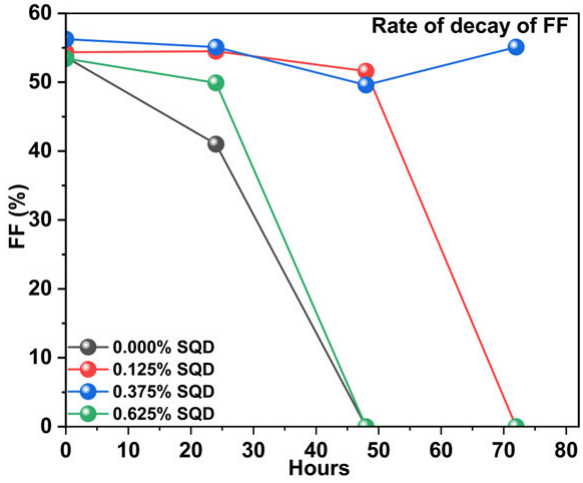

Figure S6.3: Change in the FF with the lifetime of the solar cell.

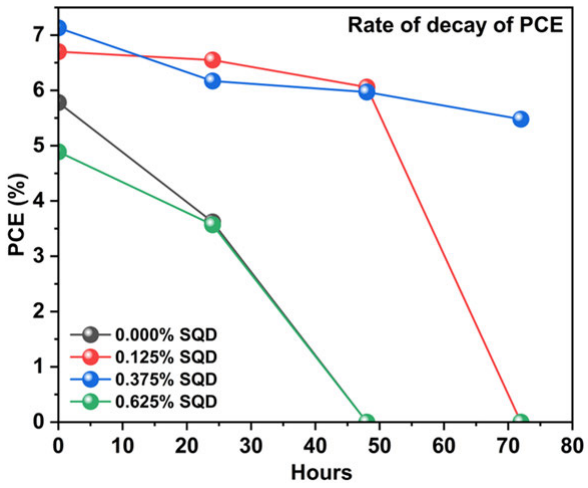

Figure S6.4: Change in the PCE with the lifetime of the solar cell.

Table S6.1: The thin-film Polymer solar cells' (TFPSCs) parameters for devices with/without SQD in ETL after 24 hours.

ZnO:$Cd_xS/Zn_{1-x}S$	V_{oc} (V)	J_{sc} (mA cm^{-2})	FF (%)	PCE (%)	R_s (Ω)	R_{SH} (kΩ)
Pristine	0.634	13.90	41.0	3.62	571.6	4.80
0.125 wt.%	0.642	18.70	54.50	6.55	220.2	8.50
0.375 wt.%	0.635	18.30	55.10	6.17	150.8	7.87
0.625 wt.%	0.622	12.60	49.90	3.57	851.6	8.65

Table S6.2: The Thin-film Polymer solar cells' (TFPSCs) parameters for devices with/without SQD in ETL after 48 hours.

ZnO:$Cd_xS/Zn_{1-x}S$	V_{oc} (V)	J_{sc} (mA cm^{-2})	FF (%)	PCE (%)	R_s (Ω)	R_{SH} (kΩ)
Pristine	-	-	-	-	-	-
0.125 wt.%	0.617	19.0	51.6	6.06	366.5	7.07
0.375 wt.%	0.629	19.20	49.6	5.97	305.2	6.32
0.625 wt.%	-	-	-	-	-	-

Table S6.3: The Thin-film Polymer solar cells' (TFPSCs) parameters for devices with/without SQD in ETL after 72 hours.

ZnO:$Cd_xS/Zn_{1-x}S$	V_{oc} (V)	J_{sc} (mA cm^{-2})	FF (%)	PCE (%)	R_s (Ω)	R_{SH} (kΩ)
Pristine	-	-	-	-	-	-
0.125 wt.%	-	-	-	-	-	-
0.375 wt.%	0.593	18.40	55.1	5.48	166.0	6.33
0.625 wt.%	-	-	-	-	-	-

References

[1] Qazi, A., Hussain, F., Rahim, N., Hardaker, G., Alghazzawi, D., Shaban, K. & Haruna, K. Towards sustainable energy: A systematic review of renewable energy sources, technologies, and public opinions. IEEE Access. **7** pp. 63837-63851 (2019)

[2] Nushra, O., Shafkat, T. & Ali, M. Efficiency improvement analysis for recent high-efficient solar cells. AIUB Journal Of Science And Engineering (AJSE. **19**, 1-6 (2020)

[3] Liu, Q., Jiang, Y., Jin, K., Qin, J., Xu, J., Li, W., Xiong, J., Liu, J., Xiao, Z. & Sun, K. 18% efficiency organic solar cells. *Science Bulletin.* **65**, 272-275 (2020)

[4] Cui, Y., Yao, H., Zhang, J., Xian, K., Zhang, T., Hong, L., Wang, Y., Xu, Y., Ma, K. & An, C. Single-junction organic photovoltaic cells with approaching 18% efficiency. Advanced Materials. **32**, 1908205 (2020)

[5] Wang, J., Wang, Y., Bi, P., Chen, Z., Qiao, J., Li, J., Wang, W., Zheng, Z., Zhang, S. & Hao, X. Binary organic solar cells with 19.2% efficiency enabled by solid additive.Advanced Materials. pp. 2301583 (2023)

[6] Chen, Z., Zhu, J., Yang, D., Song, W., Shi, J., Ge, J., Guo, Y., Tong, X., Chen, F. & Ge, Z. Isomerisation strategy on a non-fullerene guest acceptor for stable organic solar cells with over 19% efficiency. Energy & Environmental Science. **16**, 3119-3127 (2023)

[7] Fan, Q., Ma, R., Bi, Z., Liao, X., Wu, B., Zhang, S., Su, W., Fang, J., Zhao, C. & Yan, C. 19.28% efficiency and stable polymer solar cells enabled by introducing an nir-absorbing guest acceptor. Advanced Functional Materials. **33**, 2211385 (2023)

[8] Guo, C., Fu, Y., Li, D., Wang, L., Zhou, B., Chen, C., Zhou, J., Sun, Y., Gan, Z. & Liu, D. Polycrystalline polymer donor as pre-aggregate toward ordered molecular aggregation for 19.3% efficiency binary organic solar cells. Advanced Materials. pp. 2304921 (2023)

[9] Jiang, Q., Tong, J., Xian, Y., Kerner, R., Dunfield, S., Xiao, C., Scheidt, R., Kuciauskas, D., Wang, X. & Hautzinger, M. Surface reaction for efficient and stable inverted perovskite solar cells. Nature. **611**, 278-283 (2022)

[10] Dréon, J., Jeangros, Q., Cattin, J., Haschke, J., Antognini, L., Ballif, C. & Boccard, M. 23.5%-efficient silicon heterojunction silicon solar cell using molybdenum oxide as hole-selective contact. Nano Energy. **70** pp. 104495 (2020)

[11] Günther, M., Kazerouni, N., Blätte, D., Perea, J., Thompson, B. & Ameri, T. Models and mechanisms of ternary organic solar cells. Nature Reviews Materials. pp. 1-16 (2023)

[12] Wang, J., Wang, Y., Xian, K., Qiao, J., Chen, Z., Bi, P., Zhang, T., Zheng, Z., Hao, X. & Ye, L. Regulating phase separation kinetics for high-efficiency and mechanically robust all-polymer solar cells. Advanced Materials. pp. 2305424 (2023)

[13] Bi, P., Wang, J., Cui, Y., Zhang, J., Zhang, T., Chen, Z., Qiao, J., Dai, J., Zhang, S. & Hao, X. Enhancing photon utilisation efficiency for high-performance organic photovoltaic cells via regulating phase-transition kinetics. Advanced Materials. pp. 2210865 (2023)

[14] Cheng, P., Li, G., Zhan, X. & Yang, Y. Next-generation organic photovoltaics based on non-fullerene acceptors. Nature Photonics. **12**, 131-142 (2018)

[15] Hamed, M., Adedeji, M., Zhang, Y. & Mola, G. Silver sulphide nano-particles enhanced photo-current in polymer solar cells. Applied Physics A. **126**, 207 (2020)

[16] Oseni, S. & Mola, G. Bimetallic nanocomposites and the performance of inverted organic solar cell, Composites Part B. Engineering. **172** pp. 660-665 (2019)

[17] Hamed, M. & Mola, G. Copper sulphide as a mechanism to improve energy harvesting in thin film solar cells. Journal Of Alloys And Compounds. **802** pp. 252-258 (2019)

[18] Arbab, E., Taleatu, B. & Mola, G. Environmental stability of ptb7: Pcbm bulk hetero-junction solar cell. Journal of Modern Optics. **61**, 1749-1753 (2014)

[19] Mola, G. & Abera, N. Correlation between lumo offset of donor/acceptor molecules to an open circuit voltage in bulk heterojunction solar cell. Physica B: Condensed Matter. **445** pp. 56-59 (2014)

[20] Mola, G., Mthethwa, M., Hamed, M., Adedeji, M., Mbuyise, X., Kumar, A., Sharma, G. & Zang, Y. Local surface plasmon resonance assisted energy harvesting in thin film

organic solar cells. Journal Of Alloys and Compounds. **856** pp. 158172 (2021)

[21] Wang, E., Wang, L., Lan, L., Luo, C., Zhuang, W., Peng, J. & Cao, Y. High-performance polymer heterojunction solar cells of a polysilafluorene derivative. Applied Physics Letters. **92** (2008)

[22] Zhu, L., Zhang, M., Xu, J., Li, C., Yan, J., Zhou, G., Zhong, W., Hao, T., Song, J. & Xue, X. Single-junction organic solar cells with over 19% efficiency enabled by a refined double-fibril network morphology. Nature Materials. **21**, 656-663 (2022)

[23] Kim, J., Lee, K., Coates, N., Moses, D., Nguyen, T., Dante, M. & Heeger, A. Efficient tandem polymer solar cells fabricated by all-solution processing. Science. **317**, 222-225 (2007)

[24] Wang, J., Zheng, Z., Zu, Y., Wang, Y., Liu, X., Zhang, S., Zhang, M. & Hou, J. A tandem organic photovoltaic cell with 19.6% efficiency enabled by light distribution control. Advanced Materials. **33**, 2102787 (2021)

[25] Franeker, J., Turbiez, M., Li, W., Wienk, M. & Janssen, R. A real-time study of the benefits of co-solvents in polymer solar cell processing. Nature Communications. **6**, 6229 (2015)

[26] Dong, X., Jiang, Y., Sun, L., Qin, F., Zhou, X., Lu, X., Wang, W. & Zhou, Y. Large-area organic solar modules with efficiency over 14%. Advanced Functional Materials. **32**, 2110209 (2022)

[27] Wang, Z., Gao, K., Kan, Y., Zhang, M., Qiu, C., Zhu, L., Zhao, Z., Peng, X., Feng, W. & Qian, Z. The coupling and competition of crystallisation and phase separation, correlating thermodynamics and kinetics in opv morphology and performances. Nature Communications. **12**, 332 (2021)

[28] Zhao, H., Lin, B., Xue, J., Naveed, H., Zhao, C., Zhou, X., Zhou, K., Wu, H., Cai, Y. & Yun, D. Kinetics manipulation enables high-performance thick ternary organic solar cells via r2r-compatible slot-die coating. Advanced Materials. **34**, 2105114 (2022)

[29] Wang, J., Zhang, M., Lin, J., Zheng, Z., Zhu, L., Bi, P., Liang, H., Guo, X., Wu, J. &

Wang, Y. An asymmetric wide-bandgap acceptor simultaneously enabling highly efficient single-junction and tandem organic solar cells. Energy & Environmental Science. **15**, 1585-1593 (2022)

[30] Ogundele, A. & Mola, G. Ternary atoms alloy quantum dot assisted hole transport in thin film polymer solar cells. Journal of Physics and Chemistry Of Solids. **171** pp. 110999 (2022)

[31] Ma, Q., Jia, Z., Meng, L., Zhang, J., Zhang, H., Huang, W., Yuan, J., Gao, F., Wan, Y. & Zhang, Z. Promoting charge separation resulting in ternary organic solar cells efficiency over 17.5%. Nano Energy. **78** pp. 105272 (2020)

[32] Ogundele, A. & Mola, G. Semiconductor quantum dots as a mechanism to enhance charge transfer processes in polymer solar cells. Chemosphere. pp. 140453 (2023)

[33] Ashagre, S., Ogundele, A., Ike, J., Gebremichael, B., Bekele, M., Sharma, G. & Mola, G. Synergistic contribution of potassium sulfide doped with silver nanoparticles on the performance of thin film organic solar cells. Journal of Physics and Chemistry Of Solids. **177** pp. 111290 (2023)

[34] Adedeji, M., Garcia-Rodriguez, R., Davies, M., Zhang, Y. & Mola, G. Plasmon-enhanced charge transport processes for improved collection of photo-current in polymer solar cells. ACS Applied Energy Materials. **5**, 12503-12512 (2022)

[35] Oseni, S., Osifeko, O., Boyo, A. & Mola, G. Simultaneous inclusion of quantum dots in multi-functional layers of thin film organic solar cells. AIP Advances. **13** (2023)

[36] Bi, P., Zheng, F., Yang, X., Niu, M., Feng, L., Qin, W. & Hao, X. Dual förster resonance energy transfer effects in non-fullerene ternary organic solar cells with the third component embedded in the donor and acceptor. Journal of Materials Chemistry A. **5**, 12120-12130 (2017)

[37] Ma, X., Mi, Y., Zhang, F., An, Q., Zhang, M., Hu, Z., Liu, X., Zhang, J. & Tang, W. Efficient ternary polymer solar cells with two well-compatible donors and one ultranarrow bandgap nonfullerene acceptor. Advanced Energy Materials. **8**, 1702854 (2018)

[38] Hu, Z., Yang, L., Gao, W., Gao, J., Xu, C., Zhang, X., Wang, Z., Tang, W., Yang, C. & Zhang, F. Over 15.7% efficiency of ternary organic solar cells by employing two compatible acceptors with similar lumo levels. Small. **16**, 2000441 (2020)

[39] Li, K., Wu, Y., Tang, Y., Pan, M., Ma, W., Fu, H., Zhan, C. & Yao, J. Ternary blended fullerene-free polymer solar cells with 16.5% efficiency enabled with a higher-lumo-level acceptor to improve film morphology. Advanced Energy Materials. **9**, 1901728 (2019)

[40] Xie, L., Yang, C., Zhou, R., Wang, Z., Zhang, J., Lu, K. & Wei, Z. Ternary organic solar cells based on two non-fullerene acceptors with complimentary absorption and balanced crystallinity. Chinese Journal of Chemistry. **38**, 935-940 (2020)

[41] Ma, X., An, Q., Ibraikulov, O., Lévêque, P., Heiser, T., Leclerc, N., Zhang, X. & Zhang, F. Efficient ternary organic photovoltaics with two polymer donors by minimizing energy loss. Journal Of Materials Chemistry A. **8**, 1265-1272 (2020)

[42] Chen, H., Lin, L., Yu, X., Qiu, K., Lü, X., Kuang, D. & Su, C. Dextran based highly conductive hydrogel polysulfide electrolyte for efficient quasi-solid-state quantum dot-sensitised solar cells. Electrochimica Acta. **92** pp. 117-123 (2013)

[43] Baik, S., Kim, K., Lim, K., Jung, S., Park, Y., Han, D., Lim, S., Yoo, S. & Jeong, S. Low-temperature annealing for highly conductive lead chalcogenide quantum dot solids. The Journal of Physical Chemistry C. **115**, 607-612 (2011)

[44] Hernández-Gutiérrez, C., Kudriavtsev, Y., Cardona, D., Guillén-Cervantes, A., Santana-Rodríguez, G., Escobosa, A., Hernández-Hernández, L. & López-López, M. Inxga1-xn nucleation by in+ ion implantation into gan. Nuclear Instruments and Methods In Physics Research Section B: Beam Interactions With Materials and Atoms. **413** pp. 62-67 (2017)

[45] Zajac, W., Rozycka, A. & Trenczek-Zajac, A. Rational design of the electronic structure of cds nanopowders. Inorganic Chemistry. **62**, 10955-10964 (2023)

[46] D'Amico, P., Calzolari, A., Ruini, A. & Catellani, A. New energy with zns: Novel applications for a standard transparent compound. Scientific Reports. **7**, 1-9 (2017)

[47] Li, Z., Song, D., Xu, Z., Qiao, B., Zhao, S., Wageh, S., Al-Ghamdi, A. & Huo, X. Improved

uv sensitivity and charge transport in ptb7-th: Pc 71 bm solar cells doped with cadmium selenide quantum dots. Sustainable Energy & Fuels. **6**, 2053-2061 (2022)

[48] Liao, X., Wang, H., Zhu, J. & Chen, H. Preparation of bi2s3 nanorods by microwave irradiation. Materials Research Bulletin. **36**, 2339-2346 (2001)

[49] Joicy, S., Saravanan, R., Prabhu, D., Ponpandian, N. & Thangadurai, P. Mn 2+ ion influenced optical and photocatalytic behaviour of mn–zns quantum dots prepared by a microwave assisted technique. RSC Advances. **4**, 44592-44599 (2014)

[50] Porta, F., Ferrer, M., Santana, Y., Raubach, C., Longo, V., Sambrano, J., Longo, E., Andrés, J., Li, M. & Varela, J. Synthesis of wurtzite zns nanoparticles using the microwave assisted solvothermal method. Journal of Alloys and Compounds. **556** pp. 153-159 (2013)

[51] Soltani, N., Saion, E., Erfani, M., Bahrami, A., Navaseri, M., Rezaee, K. & Hussein, M. Facile synthesis of zns/cds and cds/zns core-shell nanoparticles using microwave irradiation and their optical properties. Chalcogenide Letters. **9** (2012)

[52] Shi, J., Liang, Z., Lu, X., Tong, Y., Su, C. & Liu, H. The roles of defect states in photoelectric and photocatalytic processes for $Zn_xCd_{1-x}S$. Energy & Environmental Science. **4**, 466-470 (2011)

[53] Rafea, M., Farag, A. & Roushdy, N. Structural and optical characteristics of nano-sized structure of zn0. 5cd0. 5s thin films prepared by dip-coating method. Journal Of Alloys and Compounds. **485**, 660-666 (2009)

[54] Binns, C. Introduction to nanoscience and nanotechnology. (John Wiley & Sons,2021)

[55] Mantashian, G., Mantashyan, P. & Hayrapetyan, D. Modeling of quantum dots with the finite element method. Computation. **11**, 5 (2023)

[56] Liu, X., Jiang, Y., Fu, F., Guo, W., Huang, W. & Li, L. Facile synthesis of high-quality zns, cds, cdzns, and cdzns/zns core/shell quantum dots: Characterisation and diffusion mechanism. Materials Science In Semiconductor Processing. **16**, 1723-1729 (2013)

[57] Bera, D., Qian, L., Tseng, T. & Holloway, P. Quantum dots and their multimodal appli-

cations: A review. Materials. **3**, 2260-2345 (2010)

[58] Su, X., Hu, R., Wen, G., Zou, X., Qing, M., Peng, J., He, X. & Zhang, W. Understanding of photophysical processes in dio additive-treated ptb7: Pc71bm solar cells. Crystals. **11**, 1139 (2021)

[59] Bencheikh, F., Duché, D., Ruiz, C., Simon, J. & Escoubas, L. Study of optical properties and molecular aggregation of conjugated low band gap copolymers: Ptb7 and ptb7-th. The Journal of Physical Chemistry C. **119**, 24643-24648 (2015)

[60] Huang, X., Tong, X. & Wang, Z. Rational design of colloidal core/shell quantum dots for optoelectronic applications. Journal Of Electronic Science and Technology. **18**, 100018 (2020)

[61] Kim, S., Fisher, B., Eisler, H. & Bawendi, M. Type-ii quantum dots: Cdte/cdse (core/shell) and cdse/znte (core/shell) heterostructures. Journal Of The American Chemical Society. **125**, 11466-11467 (2003)

[62] Talapin, D., Rogach, A., Kornowski, A., Haase, M. & Weller, H. Highly luminescent monodisperse cdse and cdse/zns nanocrystals synthesised in a hexadecylamine- trioctylphosphine oxide-trioctylphospine mixture. Nano Letters. **1**, 207-211 (2001)

[63] Yang, X., Qiao, J., Chen, Z., Wen, Z., Yin, H. & Hao, X. Cdse quantum dot organic solar cells with improved photovoltaic performance. Journal Of Physics D: Applied Physics. **54**, 115504 (2021)

[64] Xia, Y., Nguyen, T., Yang, M., Lee, B., Santos, A., Podsiadlo, P., Tang, Z., Glotzer, S. & Kotov, N. Self-assembly of self-limiting monodisperse supraparticles from polydisperse nanoparticles. Nature Nanotechnology. **6**, 580-587 (2011)

[65] Zhou, P., Lan, W., Gu, J., Zhao, M., Wang, Z., Liao, Y., Liu, Y., Pu, H., Ding, J. & Wei, B. High-efficiency organic photovoltaic cells with an antimony quantum sheet modified hole extraction layer. IEEE Journal Of Photovoltaics. **11**, 111-117 (2020)

[66] Foster, S., Deledalle, F., Mitani, A., Kimura, T., Kim, K., Okachi, T., Kirchartz, T., Oguma, J., Miyake, K. & Durrant, J. Electron collection as a limit to polymer: Pcbm solar

cell efficiency: Effect of blend microstructure on carrier mobility and device performance in ptb7: Pcbm. Advanced Energy Materials. **4**, 1400311 (2014)

[67] Danladi, E., Egbugha, A., Obasi, R., Tasie, N., Achem, C., Haruna, I. & Ezeh, L. Defect and doping concentration study with series and shunt resistance influence on graphene modified perovskite solar cell: A numerical investigation in scaps-1d framework. Journal Of The Indian Chemical Society. **100**, 101001 (2023)

CHAPTER 7

CONCLUSION

7.1 Summary

In this thesis, we explored the potential of semiconductor quantum dots (SQDs) as guest components in optimizing the performance of organic solar cells. The photo active media were polymer blends composed of P3HT:PCBM and PTB7:$PC_{71}BM$. This study investigated the use of group II-VI semiconductor quantum dots, including ternary alloy SQDs (CdTeSe), core SQDs (ZnS), and core-shell SQDs ($Cd_xS/Zn_{1-x}S$). These SQDs were incorporated as guest components into various layers of polymer solar cells: ternary alloy SQDs in the hole transport layer, core SQDs in the photoactive layer, and core-shell SQDs in the electron transport layer.

The alloyed (CdTeSe) SQD was doped at different concentrations (1, 3, 5, and 7%) by volume into the hole transport layer (PEDOT:PSS) using a P3HT:PCBM blend as a photoactive absorber in conventional device architecture. The investigation revealed that the incorporation of ternary alloy CdTeSe quantum dots (QDs) did not reduce the transmittance of the hole transport layer (HTL); instead, it enhanced the electron-blocking capability of PEDOT and improved its hole extraction efficiency from the active layer. The absorption spectra and calculated charge carrier mobilities of the modified films also showed a broader spectrum and improved charge transport compared to the pristine devices. There was a surge in photocurrents in the modified devices which reflected with other PV parameters signifying improved photon harvesting. This synergies resulting from the doping of CdTeSe recorded an optimal performance at a 5% concentration by volume, with a power conversion efficiency (PCE) of 4.87%, representing an increase of about 111% in PCE compared to the pristine device, which had a PCE of 2.30%.

Microwave-assisted synthesised ZnS QDs were incorporated into the photoactive layer composed of P3HT:PCBM blends at different concentrations by weight (1, 3, and 5%) using conventional architecture. The synthesis method ensured the production of quantum dots with uniform distribution and small crystallite sizes. X-ray diffraction (XRD) analysis indicated good crystallisation, evidenced by fewer, sharper, and broadened diffraction peaks, which were consistent with transmission electron microscopy (TEM) measurements and evaluated size. The incorporation of relatively large bandgap QDs with small size helped capture high-energy photons, as indicated by a blue shift in the optical absorption of the film. The modified photoactive layer exhibited effective charge transfer from the QDs to the blends, as shown by photoluminescence (PL) measurements. The intermediate energy bandgap of ZnS QDs, which lies between P3HT and PCBM, played an important role in bandgap alignment, leading to enhanced open-circuit voltage (V_{oc}) and reduced energy loss. The down-conversion effect due to the incorporation also yielded a wider spectrum in the infrared region of the modified photoactive films. Ultimately, the synergies created by the incorporation of ZnS QDs in the active blend resulted in optimal performance at a concentration of 3 wt.%, with a PCE of 5.01%, representing a 58% increase compared to the pristine device.

The core-shell SQD, composed of a medium-energy bandgap core and a relatively large bandgap shell ($Cd_xS/Zn_{1-x}S$), was employed at various concentrations of 0.125, 0.375, and 0.625 wt.% in the electron transport layer (ETL) of zinc oxide nano-ink suspension, with PTB7:$PC_{71}BM$ as the solar absorber. The impact of core-shell SQDs on light harvesting was demonstrated through improved light absorption, exciton generation, exciton dissociation, and the transport of free charge carriers to the electrodes. The investigation revealed reduced energy losses in modified devices compared to pristine ones, as well as the harvesting of high-energy photons due to the shell SQD and lower-energy photons due to the core SQD. The study showed that the improved performance resulting from doping guest components into the electron transport layer was beneficial up to a certain threshold concentration. The device exhibited optimal performance at a doping concentration of 0.375 wt.%, achieving a PCE of 7.13%, which represents an improvement over the pristine device's PCE of 5.78%.

7.2 Implication of the study

Features of semiconductor quantum dots, such as photo-absorption, tunable bandgap, photoluminescence, multiple exciton generation, quantum confinement, stability and versatility, played important roles in the optimisation of organic solar cells. The study showed that the ap-

plication of SQD in the functional layers of organic solar cells led to a significant enhancements of PV parameters, resulting from photon harvesting, enhanced exciton generation and dissociation, and efficient carrier transport. However, challenges such as dispersion in solvent, poor phase separation between the organic polymer matrix and inorganic quantum dots inhibit carrier transport due to trapping defects that promote recombination. These shortcomings were reduced with adequate miscibility, surface passivation, and optimal threshold doping of SQD. Therefore, it can be concluded that the advantageous properties of semiconductor quantum dots outweigh the challenges posed by their integration into the functional layers of polymer solar cells, making them a promising approach for optimizing solar cell performance.

7.3 Recommendations

These investigations can be extended to the utilisation of SQDs as the interconnecting layer in tandem polymer solar cells architecture (either fullerene based or non-fullerene based). With this approach, the use of either n-type or p-type SQD can eliminate the challenges typically encountered when two different transport layers are stacked on top of each other as the top of the rear sub-cell and the bottom of the front sub-cell respectively. In doing this, the chosen SQD acts as the interconnecting layer, complementing the absorption spectrum of the sub-cells. Likewise, in a typical BHJ organic solar cells, the SQD can be thermally deposited as an interlayer inside a vacuum depositor chamber. This would require the determination of evaporation data which include density, melting point, and Z-ratio of SQD. With these information, the SQD can be used in lieu of traditional interlayers like lithium fluoride or molybdenum trioxide. The medium to large energy bandgap quantum dots can be used for this purpose because they have similar bandgap with the traditional transport layers. It is expected that the use of semiconductor quantum dots will enhance the charge collection at the electrodes. Moreover, the as-synthesised SQD can be utilised at a known thickness without the need for pre-dispersion in solvent. Moreso, the pinhole defect that is associated with spin-coating technique will be eliminated. Moreover, It is believed that inherent hole and electron-blocking capabilities along with the tunable bandgap characteristics of SQD, will enhance device parameters as well as improve the stability of polymer solar cells. Above all, there is a need to use controlled environments, such as gloveboxes and clean rooms, to minimize contaminants. It is believed that these approaches will help to achieve better cell parameters and provide valuable insights into organic PV technologies.